Ultrasound Methods for Quantitative Edema Monitoring

by

John J. Pitre, Jr.

A dissertation submitted in partial fulfillment
of the requirements for the degree of
Doctor of Philosophy
(Biomedical Engineering)
in the University of Michigan
2017

Doctoral Committee:

Professor Joseph L. Bull, Chair
Professor J. Brian Fowlkes
Professor William Schultz
Dr. William F. Weitzel, Department of Veterans Affairs Hospital, Ann Arbor, MI

2017

For Dad

I have fought the good fight, I have finished the course, I have kept the faith.—2 Timothy 4:7

ACKNOWLEDGMENTS

There are so many people I wish to thank for their help in my doctoral studies, and an exhaustive list would take far too long to write and to read. I will try to keep this as brief as I am able. First, I would like to thank my committee – Professors Joseph Bull, Brian Fowlkes, William Schultz, and Dr. William Weitzel – for their thoughts, ideas, and guidance.

My advisor, Joseph Bull, has been an outstanding source of mentorship, support, and friendship throughout this Ph.D. process. It would be so easy to understate the impact he has had in helping me to become a better researcher, scientist, and teacher. His mentorship has provided me with both wonderful insight and experience into so many aspects of academic science. Above and beyond that, however, I cannot thank him enough for the understanding and flexibility he showed to me through some very difficult times. I will always be grateful for the time he allowed me to work remotely to spend time with my father. It was invaluable to me.

This work could also simply have not been possible without the influence and guidance of Rick Weitzel. His insight into the real practical problems facing clinicians has been a key component directing my research. I have learned so much, through both him and Dr. Bull, about the grant writing process, translational research, and multidisciplinary collaboration.

I also thank my other committee members, Brian Fowlkes and William Schultz, for their ideas and discussions. Their questions, suggestions, and challenges were instrumental in driving this dissertation forward and improving my research and analyses. They forced me to challenge assumptions I took for granted, and I believe this dissertation is far better because of their input.

I owe a great deal of thanks to current and former lab mates who have been wonderful sources of discussion, assistance, mentorship, and friendship. Working

with them has been a great pleasure, and I will always feel grateful to have met them and worked with them, both the members of the Biotransport Lab – David Li, Robinson Seda, Stanley Samuel, Samantha Stephenson, Nelson Smith, Xianglong Wang, Jonah Harmon, and Foad Kabinejadian – and the VA Ultrasound Lab – Leo Koziol, Alan Vollmer, and Karen Belanger. I also am incredibly thankful to Yang Liu and Ashish Sahani who assisted me in planning and setting up ultrasound experiments. The Biomedical Engineering staff have also been a wonderful resource, and I would be remiss if I did not thank Brandon Baier, Chuck Nicholas, Maria Steele, and the rest of the staff for their assistance with hundreds of assorted matters of requirements, paperwork, computers, and general questions.

Finally, and most importantly, I owe an immeasurable debt of gratitude to my friends and family. They cannot begin to fathom how much their love, friendship, support, and encouragement have meant to me. It is truly not an exaggeration to say I could not have finished these doctoral studies without them. They were there in all of the most difficult moments pushing me forward. Mom, Dad, David, Maria, Grandma, Nanny, Pawpaw, Matt, Nidhi, Sydney, Sriram, Janki, David, Robinson, Brandon, Amy, Lee, Sarah, Katie, Jonathan, Stephanie, Krystal, Josh, Elizabeth, Jonathan, Jade, and Megan – Thank you, thank you, thank you.

TABLE OF CONTENTS

LIST OF FIGURES

LIST OF TABLES

ABSTRACT

Ultrasound Methods for Quantitative Edema Monitoring

by

John J. Pitre, Jr.

Chair: Joseph L. Bull

Patients with end stage renal disease typically must undergo regular dialysis treatments to replace the loss of kidney function. A critical part of these dialysis treatments is the careful management of fluid status, as these patients are at an increased risk for developing fluid overload, a condition that poses a number of dangers to their health and quality of life. Current clinical methods are lacking in their ability to accurately provide a quantitative metric for grading edema and fluid overload. In this dissertation, I explore a number of methods based on ultrasound strain imaging, ultrasound viscoelastography, and ultrasound poroelastography to address this clinical need. The practical and theoretical aspects of the measurement process and parameter estimation methods are explored, and new methods are proposed and evaluated to overcome common difficulties. Chiefly, the experiments and simulations described in this work aim to highlight the role of assumptions in visco- and poroelastic imaging, to explore how these assumptions can hinder accurate parameter estimation, and to develop methods that are less

assumption-dependent. First, I evaluate a point-of-care ultrasound viscoelastography system and use it to estimate the viscoelastic properties of a tissue-mimicking material. The strain and material properties are observed to be depth dependent, highlighting possible breaks with the viscoelastic model assumptions and possible poroelastic behavior. Next, I analyze the role of model assumptions on poroelastography measurements using both finite element models and benchtop experiments. Strain magnitudes and loading geometries that differ from the model assumptions used in most poroelastography studies are shown to produce large differences in poroelastic parameter estimates. Furthermore, they can lead to lateral-to-axial strain ratio measurements that do not converge to the true Poisson's ratio of the material, thus highlighting the need for more careful interpretation of standard effective Poisson's ratio (EPR) poroelastograms. Finally, I develop and evaluate a new approach to poroelastography by posing the poroelastic imaging as an inverse problem. This allows for the quantitative imaging of spatial variations. This method is shown to produce more accurate poroelastic images in simulations with ideal, Gaussian corrupted data. In addition, the method shows promise in reconstructions based on simulated ultrasound images, though some difficulties remain. Possible improvements and recommendations for future poroelastography studies are discussed.

CHAPTER 1

Introduction

The following work explores ultrasound-based methods for estimating the material properties of edematous tissue. The problem of quantifying the degree of edema is one for which no one solution exists, and various methods have been proposed to meet this need. Of interest to this work are a class of methods called poroelastography that rely on ultrasound strain measurements to characterize the temporal behavior of tissue under compression. The benchtop experiments and simulation studies reported in this dissertation seek to address both the practical and theoretical aspects of this problem, which sits at the intersection of tissue mechanics, signal processing, image reconstruction, and applied mathematics. The work has therefore been organized into the following chapters:

1. Chapter 2 (Background) discusses the practical clinical aspects of the edema quantification problem. It provides an overview of the basic techniques involved in ultrasound strain estimation and proceeds into a review of the literature in the subfield of ultrasound poroelastography, including preliminary clinical studies.

2. Chapter 3 (Theory) provides derivations of the Biot model of poroelasticity as well as Armstrong's solution to the Kuei-Lai-Mow biphasic model, both of which can be used to provide the theoretical basis for poroelastography. The

implications of these theoretical treatments will become particularly important in chapters 5 and 6.

3. Chapter 4 (Design and testing of a single-element ultrasound viscoelastography system for point-of-care edema quantification) describes benchtop experiments and analysis to evaluate the performance of a simple, low-cost ultrasound system for quantifying viscoelastic properties of a tissue mimicking material under compression at large strain.

4. Chapter 5 (The effects of geometry and strain magnitude on poroelastography curve fitting) discusses the implications of incorrect assumptions on poroelastic parameter estimation. Finite element models are used to provide numerical evidence of the different behavior that might be expected to occur under different poroelastography measurement configurations. These effects are then demonstrated in benchtop experiments.

5. Chapter 6 (Evaluation of a model-based ultrasound poroelastography algorithm) describes a new framework for poroelastic image formation based on an inverse problem formulation. This removes assumptions of spatial uniformity from the parameter estimation process. The performance of the algorithm is investigated in simulation studies using both ideal data and synthetic ultrasound image sequences.

6. Chapter 7 (Conclusions and future directions) summarizes the overall results of this work, their implications for the broader field of poroelastography, and their impact on the clinical problem of edema quantification. Future directions and questions raised are also presented.

CHAPTER 2

Background

2.1 Clinical Motivation

In its 2016 Annual Report, the United States Renal Data System reported 678,383 prevalent cases of end stage renal disease (ESRD) in the United States (United States Renal Data System, 2016). ESRD is the final stage of chronic kidney disease (CKD) and is marked by a decreased glomerular filtration rate (less than 15 mL/min/173m^2) and/or the need for renal replacement therapy (National Kidney Foundation, 2002). Most patients with ESRD (97.2%) undergo regular dialysis treatments to replace the loss of kidney function. A critical part of these dialysis treatments is the careful management of fluid status, as ESRD patients are at an increased risk for developing fluid overload. As many as 30% of dialysis patients may exceed the recommended levels of fluid retention (Lindberg et al., 2009), and the prevalence of fluid overload in dialysis patients is strongly associated with the occurence of clinical care episodes and higher mortality (Leggat et al., 1998; Mallick and Gokal, 1999; Saran et al., 2003; Stegmayr et al., 2006; Movilli et al., 2007; Kalantar-Zadeh et al., 2009; Arneson et al., 2010). As such, it is imperative that patient hydration status be accurately, easily, and reproducibly monitored. Fluid overload is a complex pathological state manifesting itself with excess fluid in various body compartments including the vascular, pulmonary, abdominal, and

peripheral spaces. While simple quantitative methods exist for measuring fluid in the vascular space (blood pressure or CRIT-LINE)(Rodriguez et al., 2005), measurements in the other compartments are either invasive – pulmonary capillary wedge pressure in the case of pulmonary edema – or qualitative – ultrasound or physical examination in the cases of aciteps (abdominal) or peripheral edema (Hogan, 2007).

Currently, the clinical practice of determining a patient's ideal fluid status, known as dry weight, follows a process that is largely reactive or subjective. For example, clinicians often note the weight at which hypotension and cramping are observed as fluid is removed during a dialysis treatment. Additionally, clinicians use a physical examination to monitor the level of peripheral edema, grading it on a semi-quantitative scale of 0-4+ (Table 2.1). In this "pitting test", a clinician uses his or her thumb to compress a small region of the edematous limb (Figure 2.1). The level of edema is then assessed based on the observed depth of the depression, the rebound time, and the condition of the skin. In contrast to other quantitative methods routinely used in the clinic, for example, to measure blood pressure, the edema pitting test can be largely subjective and leaves room for large inter-examiner variation (Brodowicz et al., 2009). Studies have shown that these methods are neither specific nor sensitive enough, and this has stimulated interest in improving quantitative measures of dry weight and fluid overload. To this end, several methods have been proposed including the measurement of biochemical markers, interior vena cava diameter, bioimpedance, mechanical properties, and blood volume. These methods have repeatedly demonstrated that the clinical exam alone is an inadequate measure of dry weight, underestimating fluid overload in 24-37% of patients (Kouw et al., 1993; Oe et al., 2000; Yashiro et al., 2007).

2.2 Ultrasound Elastography

Ultrasound-based approaches to quantifying fluid overload hold a number of advantages. Ultrasound imaging is non-invasive, and it can be performed quickly and easily, facilitating its use at the point-of-care. One approach that has been proposed is the use of ultrasound elastography to quantify edematous tissue mechanical properties (Righetti et al., 2007a; Berry et al., 2008; Adriaenssens et al., 2012; Kruger et al., 2012). Ultrasound elastography is an imaging technique that uses a known compressive stress to elicit a measurable strain in a region of tissue (Ophir et al., 1991). Briefly, an ultrasound transducer is placed so that a region of interest is visible, and an initial image is captured. A known axial compressive stress is then applied to the tissue, inducing a deformation, and a second ultrasound image is acquired. Assuming that compression occurs in the axial direction only, Hooke's law for linear elasticity states that the stress σ in the tissue must be proportional to the strain ε,

$$\sigma = E\varepsilon. \tag{2.1}$$

The proportionality constant E is known as the Young's modulus, and it is a measure of the elasticity of a material. Assuming the applied stress is known and is uniform throughout the tissue, only the internal strain field is needed to estimate the Young's modulus. That is,

$$E = \frac{\sigma_{applied}}{\varepsilon_{measured}}. \tag{2.2}$$

Internal strain can be estimated by measuring the displacement between the first and second ultrasound images at each point in the tissue. By definition, the strain

tensor ε_{ij} is related to the displacement vector u_i by

$$\varepsilon_{ij} = \frac{1}{2}(u_{i,j} + u_{j,i}). \tag{2.3}$$

Since it is assumed that only axial strains are present, equation 2.3 can be simplified by considering only the third component. If z represents the axial direction, this leaves the relationship

$$\varepsilon_{\text{measured}} = \varepsilon_{33} = \frac{\partial u_3}{\partial z}. \tag{2.4}$$

Provided the displacement estimates and differentiation operation are accurate enough, equations 2.2 and 2.4 can be combined to accurately estimate the Young's modulus.

2.3 Ultrasonic Speckle Tracking

2.3.1 Basic Algorithm

Internal tissue displacements can be estimated using a technique called ultrasonic speckle tracking. To form an ultrasound image, a pressure transducer emits a high frequency sound wave. The wave travels through the tissue, interacting with the many microscale features present. Each of these features creates a scattered sound wave that returns to the transducer, which records the pressure waves as an electrical signal. This recorded signal is called the raw radiofrequency (RF) signal. The direct reflection of sound waves is not the only feature recorded in the RF signal. As the sound scatters, the hills and valleys of the waves interfere constructively and destructively, creating small bright and dark spots, respectively. This interference pattern is called ultrasonic speckle. The speckle pattern is intrinsically linked to the unique microscale geometry of the tissue, and motion of the tissue induces a near identical motion of the speckle pattern. Speckle can therefore be used as a

type of identifying "tissue marker" to track how discrete regions move between two ultrasound images.

Speckle tracking algorithms rely on cross correlation to track motion. Small windows, or kernels, are defined in the precompression image, typically along each A-line of the RF data. The normalized cross correlation ρ between the kernel k and a search region s in the postcompression image is then computed:

$$\rho(m) = \frac{\sum_{n=0}^{N-m-1} s_{n+m} k_n^*}{\sqrt{\left(\sum_{n=0}^{N-1} s_n s_n^*\right)\left(\sum_{n=0}^{N-1} k_n k_n^*\right)}}. \tag{2.5}$$

The peak of the normalized cross correlation corresponds to the best match between the pre- and postcompression images, and the associated lag represents the most likely displacement. Figure 2.2 summarizes the speckle tracking process graphically.

As long as the speckle pattern remains correlated between the pre- and postcompression RF signals, the displacement estimates obtained by this simple algorithm will be accurate. However, strains lead to changes in the speckle pattern, and the correlation peak may become ambiguous, resulting in displacement errors. This decorrelation of the signal tends to increase with the strain. To overcome these challenges, a number of improvements to the basic speckle tracking algorithm have been developed. One important development was the strain filter, a theoretical framework used to estimate the internal tissue strain required to obtain the most accurate estimates of the displacement (Varghese and Ophir, 1997a). Strain filter theory states that the optimal strain is 1-2%. At higher strains, the elastographic signal-to-noise ratio drops abruptly. Other approaches have sought to cleverly improve the correlation between pre- and postcompression signals. These methods include fixed and adaptive temporal stretching (Varghese and Ophir,

1996, 1997b; Alam and Ophir, 1997; Alam et al., 1998), short time correlation (Lubinski et al., 1999), and the use of dynamic programming (Petrank et al., 2009). All of these approaches allow for greater accuracy at higher strains.

An alternate approach for large strain measurements relies on acquiring a time series of images. The pre- and postcompression frames for the tracking step are then carefully chosen so as to ensure that the strain between that frame pair falls in the 1-2% range. This produces an incremental displacement (or equivalently strain) estimate that may be summed over the entire sequence of tracked frames, effectively measuring large total strains while only tracking over more optimal small strains (Righetti et al., 2005a).

Once the displacements are obtained, the strain field can be estimated. A naive approach might use simple finite differences to approximate spatial derivatives. In practice, this process amplifies noise in the displacement estimates. To avoid this, a local least-squares fit can be used to estimate the mean slope over small regions of the displacement field. The number of points included in the fit must be chosen carefully so as to balance smoothness and resolution. The resulting strain field may then be used, together with a material model, to estimate tissue properties.

2.3.2 Two-dimensional Speckle Tracking

Speckle tracking in the axial direction (along the ultrasound beam) can produce displacement estimates with a very fine spatial resolution. This is because axial resolution is determined by the pulse length, which is on the order of 0.5-1 mm for a typical ultrasound system (Hoskins et al., 2010). Speckle tracking algorithms can be extended to the lateral direction as well, but displacement estimates in the lateral direction are inherently less accurate. Lateral resolution is a function of the pulse width, which is typically on the order of 1-5 mm (Hoskins et al., 2010). Furthermore, the lack of lateral phase information and the relatively low spatial

sampling in the lateral direction make lateral tracking difficult.

To overcome the difficulties associated with lateral speckle tracking, Konofagou and Ophir (1998) introduced an iterative two-dimensional speckle tracking algorithm capable of producing accurate displacement estimates in both the axial and lateral directions. First, the postcompression ultrasound image is laterally upsampled by creating new linearly interpolated A-lines between the original A-lines. Tracking windows from the A-lines in the precompression frame are tracked axially using the same methods detailed in the previous section. Tracking then proceeds laterally from the location of the best axial displacement estimate. In this step, the interpolated postcompression A-lines are used to provide better lateral sampling. These alternating axial and lateral tracking steps can then be repeated for a set number of iterations or until the correlation coefficient converges to a high value. Since this method produces accurate estimates of lateral displacement, a strain estimator can also be applied in the lateral direction to produce an estimate of the lateral strain.

2.4 The Inverse Elastography Problem

In the previous sections, I described how elastography could be used to obtain strain estimates and how Hooke's law could be used to obtain a Young's modulus estimate. This approach relies on two critical assumptions, both of which are taken as a given in most elastography studies. The first is that the stress is uniform throughout the tissue and that it is equal to the applied stress at the boundary. In general, this is not true. The prescence of lateral strains in the compressed tissue points to a slightly more complex relationship between the mechanical properties, stress, and strain. It becomes important to consider not only the Young's modulus but also the Poisson's ratio of the tissue being imaged. This analysis requires a

more nuanced appraoch. One must consider the general form of the equilibrium equations for linear elastic solids

$$\sigma_{ij,j} = 0, \tag{2.6}$$

$$\sigma_{ij} = \frac{E}{(1+\nu)(1-2\nu)} \left[\nu\delta_{ij}\varepsilon_{kk} + (1-2\nu)\varepsilon_{ij}\right], \tag{2.7}$$

$$\varepsilon_{ij} = \frac{1}{2}(u_{i,j} + u_{j,i}). \tag{2.8}$$

Typically, studies simplify these equations by making the second major assumption – that the tissue is incompressible. Incompressibility implies that the Poisson's ratio equals 0.5. This provides a link between the axial and lateral strains.

Even with the incompressibility assumption, the elastography problem remains difficult:

> Given a set of known displacements $u_i(x, y)$ and known boundary forces, determine the Young's modulus field $E(x, y)$ that satisfies equations 2.6-2.8.

The above is known as an inverse elasticity problem. Posing the elastography problem in this way allows for more complicated physics and even more complex material models to be employed. Furthermore, the inverse problem formulation reduces artifacts and performs better than strain-based formulations in cases of high elasticity contrast (Doyley et al., 2005). Provided the solution to the inverse problem can be computed (Barbone and Bamber, 2002), this approach to generating an elastogram becomes very appealing.

Skovoroda et al. (1994, 1995, 1999) posed the inverse elastography problem using a displacement-pressure formulation, solving it for both small and large deformation using a gradient descent method. In contrast, Kallel and Bertrand (1996) solved the elastography inverse problem using a modified Gauss-Newton method.

This approach has become much more common in model-based elastography. Using both ideal displacement data and simulated RF ultrasound data, they were able to reconstruct Young's modulus images for materials with hard cylindrical inclusions. Doyley et al. (2000) provided experimental validation of this technique using a similar inverse problem solver, the Levenberg-Marquardt method.

Both the Gauss-Newton and Levenberg-Marquardt methods face a computational disadvantage. Namely, they both require a computation of the system Jacobian, or sensitivity, matrix. Computing the Jacobian directly requires that the forward elasticity problem be solved at least once for each pixel in the image. Oberai et al. (2003, 2004) derived and tested an adjoint-based method for computing the Jacobian matrix that greatly reduces computational costs, requiring only one solve of the forward problem when linear elasticity is assumed.

More recent work in model-based elastography has focused on implementing more accurate tissue models into the inverse elastography framework. In particular, numerous studies have sought to measure the properties of tissue assuming it behaves as a more complex hyperelastic material (Samani and Plewes, 2004; Goenezen et al., 2011, 2012).

2.5 Ultrasound Poroelastography

The stress-strain behavior of biological tissue is rather complex. This is due to its complex structure. Biological tissue is not a homogeneous solid, but rather a large network of many constituent components. Most simply, tissue can be divided into three parts: the cells, the extracellular matrix, and the interstitial fluid. The extracellular matrix is a dense network of polysaccharides and proteins that houses the various cells of the body. Its primary structural components are collagen and elastin. These fibrous proteins account for the elastic properties of tissue

as well as anisotropy. The extracellular matrix is saturated with the interstitial fluid, a solution of water and the various dissolved ions necessary for physiological function. The interaction between the extracellular matrix and the interstitial fluid during deformation also contributes to the complex stress-strain response. The movement of fluid through the porous extracellular matrix leads to time dependent responses, for example, creep and stress relaxation. The relative motion of fibrous proteins against each other also contributes to these responses. A number of constitutive relationships are used to model tissue behavior ranging in complexity. The most common are hyperelastic models to account for the nonlinear stress-strain relationship, and viscoelastic or poroelastic models to account for the effects of fluid motion within the tissue.

The poroelastic model of tissue is of special interest when discussing edematous tissue. Since edema is a state of fluid overload in tissue, fluid motion is very important to the stress-strain response. As mentioned earlier, the clinical "pitting test" of edema is based in part on the refilling time of the deformed region – that is, the time required for interstitial fluid to flow back into the compressed region. Both the initial compression and the refilling are time dependent. Suppose a compressive force is applied to a region of tissue. In response, the extracellular matrix deforms elastically and pressurizes the interstitial fluid. The increase in internal fluid pressure drives fluid flow through the porous matrix according to Darcy's law. As more fluid leaves the compressed region, less fluid remains to support the extracellular matrix. This leads to tissue exhibiting a slow additional deformation, the creep response, which approaches a constant value once all the mobilizable fluid is driven from the region.

Poroelastography methods seek to image the mechanical properties that lead to this poroelastic response – the elastic coefficients of the extracellular matrix, the fluid volume contained in it, and the porosity and permeability of the tissue. It

has been hypothesized that these measurements may be useful in a diverse number of clinical settings, including edema monitoring. The first attempt to image the poroelastic properties of tissue came from Konofagou and Ophir (1998). In their study, they introduced the interative axial and lateral speckle tracking algorithm and used the newly acquired lateral strain images to form a lateral-to-axial strain ratio elastogram, giving a measurement of the effective Poisson's ratio of the tissue (EPR). Konofagou et al. (2001) later termed this method poroelastography when they combined their measurement method of the lateral-to-axial strain ratio with a theoretical solution of deformation for a biphasic poroelastic material. Note that the terms lateral-to-axial strain ratio elastogram and EPR elastogram are used interchangably in the literature, and I will follow that convention here.

The initial theoretical basis for poroelastography was an analytical solution to the Kuei-Lai-Mow (KLM) biphasic model of tissue (Kuei et al., 1978; Mow and Kuei, 1980; Armstrong et al., 1984). The KLM model can be derived by considering the conservation of mass, momentum, and energy for a binary mixture of fluid and solid constituents. The model was originally used to describe the stress-strain response of articular cartilage, where it successfully described the creep and stress relaxiation responses of cartilage under sustained compression (Mow and Kuei, 1980). Armstrong et al. (1984) later derived an analytical solution to the KLM equations for a uniform unconfined cylinder with slip boundary conditions subjected to an axial compressive stress. This solution, which will be described in more detail later, dictates that the average lateral-to-axial strain ratio (the average effective Poisson's ratio) in the cylinder should decay in time to that of the drained matrix.

The typical model for poroelastography studies proceeds as follows (Konofagou et al., 2001; Righetti et al., 2004, 2005a,b; Berry et al., 2006a,b). First, displacement data are collected according to a standard elastography protocol. The tissue to be imaged is compressed, and pre- and postcompression images are collected. Typ-

ically, a time series of multiple postcompression images is collected. Ultrasound speckle tracking provides an estimate of the internal displacement field in the imaged region of interest, both in the axial and lateral directions. The EPR elastogram is then computed using a finite difference or least squares strain estimator. Finally, a curve fitting procedure is usually applied to obtain other descriptive parameters. For example, by fitting an exponential function to the each pixel of the time series of EPR elastograms, one can create an EPR time constant elastogram (Righetti et al., 2005b). This image is purely descriptive, and its relationship to the physical mechanical properties is tenuous, but it nevertheless provides a potentially useful measurement of tissue behavior. An alternative curve fitting routine uses Armstrong's solution to the KLM model (2.9) for each pixel to create a permeability elastogram (Righetti et al., 2005b) or aggregate modulus, drained Poisson's ratio, and permeability elastograms (Berry et al., 2006a,b). Armstrong's solution intrinsically assumes material uniformity, however, and so care should be taken in interpreting these elastograms in situations that do not exactly match the model assumptions (unconfined uniaxial compression of a uniform cylinder).

$$\frac{u}{a\varepsilon_0}(a,t) = \nu_s + (1-2\nu_s)(1-\nu_s)\sum_{n=1}^{\infty}\frac{\exp\left(-\frac{\alpha_n^2 H_A k t}{a^2}\right)}{\alpha_n^2(1-\nu_s)^2-(1-2\nu_s)} \tag{2.9}$$

2.5.1 Early Studies

Initial poroelastography studies made heavy use of simulated ultrasound RF data and tissue mimicking materials. One can simulate RF data by convolving the point spread function of a theoretical ultrasound scanner with the positions of uniformly distributed scatterers with Gaussian distributed scattering strengths. In its most simple form, this operation can be written in a few lines of code. Academic and commercial software packages also exist to perform these simulations (for example Field-II and FOCUS). Konofagou et al. (2001) used the solution of a finite element

model to displace the scatterers between simulated ultrasound frames. This finite element model used the Biot model of poroelasticity (Biot, 1941), which I will describe in detail later. Note that the Biot model is equivalent to the KLM model under common simplifying assumptions for soft tissue (Simon, 1992). The measured EPR showed good agreement with the computational true value, but the image was very noisy.

Righetti et al. (2004) followed a similar procedure but also tested the method experimentally using tofu as a tissue mimicking phantom. Their study exhibited similar results – namely, the Poisson's ratio image, though accurate, was highly noisy, especially for the experimental case. They also noted the difficulty in applying corrections to the lateral measured strains in the presence of contrast in both the Poisson's ratio and Young's modulus. Despite these drawbacks, the study produced an important extension to earlier work. Using experimentally measured values of the Young's modulus and permeability, the authors used Armstrong's solution to solve for the Poisson's ratio of the draiend matrix. They observed an expected decay in the mean Poisson's ratio, but the true value was difficult to obtain since the permeability could only be accurately estimated experimentally to an within an order of magnitude (by falling-head test).

In a similar study, Righetti et al. (2005b) generated two new varieties of poroelastogram using two types of tofu phantoms as well as porcine tissue. The first, the Poisson's ratio time constant elastogram, was generated by fitting an exponential curve of the form $\nu = \nu_0(1 - \exp(-t/\tau))$ to the EPR at each pixel in the series of poroelastograms, where the constant ν_0 was estimated from the experimental data directly at time $t = 0$. The time constant τ for each pixel then gives a measure for the degree to which the tissue deviates from a purely elastic behavior (since for a purely elastic material, the time constant should approach zero). The second type of poroelastogram detailed in the study, the permeability poroelastogram, re-

lies on *a priori* estimates of the drained Poisson's ratio and the Young's modulus. With both of these measurements, the EPR at each pixel in the time series of poroelastograms can be fit to Armstrong's biphasic solution to the KLM model. This provides an estimate for the permeability k at each pixel. In practice, such a procedure is difficult since it requires accurate estimates of both the Poisson's ratio and Young's modulus. Furthermore, as mentioned earlier, Armstrong's solution assumes uniform permeability, and so variations in the permeability elastogram should be interpreted carefully as they do not fit the model assumptions.

Berry et al. (2006a) improved upon Konofagou's work and Righetti's work by deriving a local, rather than average, expression for the lateral-to-axial strain ratio. This approach, which focused more heavily on the underlying theory of poroelastic deformation, centered around a curve fitting algorithm for determining the poroelastic constants. They also provided experimental validation for homogeneous tofu cylinders with slip boundary conditions (Berry et al., 2006b). While this work corrected some of the earlier theoretical flaws, it also relied on the assumption of material homogeneity throughout the region of interest. In general, this may not hold in the body, and in some cases such as tumors, it should be expected that inhomogeneity exists.

2.5.2 In vivo Studies

To date, two clinical ultrasound poroelastography studies have been performed (Righetti et al., 2007a; Berry et al., 2008). The first compared Poissons ratio time constant elastograms for patients with and without lymphedema (Righetti et al., 2007a). Ultrasound measurements were obtained from the thigh or forearm subcutis of 7 females and 1 male with clinically diagnosed lymphedema. Similar measurements were obtained from 5 female subjects without lymphedema. All subjects were asked to lie in a supine position while a constant 25% strain was

applied, corresponding to a stress relaxation experiment. Effective Poissons ratio time constant elastograms were then used to differentiate the two patient populations. While the images themselves were difficult to interpret, the mean value of the time constant for each patient provided a useful metric for differentiating the presence of lymphedema. For subjects in the non-edematous group, the mean Poissons ratio time constant was on the order of 225 seconds. In contrast, patients with lymphedema exhibited time constants on the order of 55 seconds with a distribution heavily skewed towards lower values. Although staging the degree of lymphedema was not addressed in this study and indeed remains an open problem, the ability to differentiate edematous and non-edematous subjects represents an important step forward for clinical translation and marks effective Poissons ratio poroelastography as a feasible method for edema measurements.

The second clinical poroelastography study, from Berry et al. (2008), examined the differences in the poroelastic response measured from patients with chronic unilateral lymphedema. The study examined 6 female subjects who exhibited at least a 20% fluid volume difference between the ipsilateral and contralateral arms, as measured using optoelectronic volumetry. A constant strain was applied to the measured arm for 500 seconds (stress relaxation), and ultrasound images were collected during and following a ramp-like compression. Axial strain images were then computed, and strains were compared at various depths along the image centerline. While the researchers did not analyze any poroelastic constants in this study, they were able to observe poroelastic behavior in both the ipsilateral (edematous) and contralateral (non-edematous) arms for each patient. Specifically, they observed that the axial strain in both arms exhibited temporal and spatial dependence, as is typical for poroelastic materials under compression. Moreover, they reported that these effects seemed to be more pronounced in the ipsilateral (edematous) arm. Because of the small sample size and single measurements ob-

tained per patient, more definite conclusions could not be made regarding significant differences or reproducibility. They also noted the need to reduce patient motion and to reduce experimental variance. Nevertheless, the fact that this study observed poroelastic effects in all of their clinical measurements gives ample motivation to continuing research into poroelastic imaging methods.

2.6 Measured Properties of Poroelastic Materials and Tissues

Poroelastography is still a nascent field, and as such, most of the work has taken place within the laboratory as opposed to the clinic. Tofu has frequently been used as a tissue mimicking phantom because of its porous structure and time-dependent response to applied loads. The properties of tofu as a tissue-mimicking ultrasound phantom are well documented (Wu, 2001; Kim et al., 2009), and it has become the de facto choice of phantom in poroelastography studies (Righetti et al., 2004, 2005a; Berry et al., 2006b; Righetti et al., 2007b; Perriñez et al., 2010b,a; Nair et al., 2011; Nair and Righetti, 2015). Most poroelastography studies, whether ultrasound-based or magnetic resonance-based, have sought to compare the imaged properties of tofu to those measured using standard mechanical creep and stress-relaxation tests. The goal has typically been to estimate the time constant of the temporal response (Table 2.2) or the shear modulus (Table 2.3). Studies have reported a wide range of values for these parameters. This may in part be due to the variability inherent in studying a material like tofu whose properties may vary by type (soft, firm, extra-firm), manufacturer, age, and storage conditions. These variables make it difficult to reasonably evaluate comparisons across studies.

Clinical pilot studies have also shown a wide range in variation when measuring the poroelastic properties of tissue. Often, comparisons between imaging

studies and mechanical measurements are difficult because tissue structure and loading vary greatly between the in-vivo case (typically employed for imaging studies) and the case of excised tissue (typically used for mechanical tests). Peripheral edema imaging represents a special case where a more direct comparison can be made. Both imaging tests and mechanical tests in this setting apply a compressive stress to the surface of the skin and measure the resulting deformation. The behavior is then described by fitting an exponential model to the measured axial strain or EPR, yielding a time constant. This allows comparisons of the temporal response between patients with edema and those without it. The literature in this area remains sparse, however, and the conclusions of existing studies vary. Table 2.4 summarizes some key results of one poroelastic imaging study (Righetti et al., 2007b) and three studies utilizing mechanical tests. Two of the mechanical studies suggest that edematous tissues exhibit longer time constants, but their time constant measurements differ from each other by two orders of magnitude (Mridha and Odman, 1986; Bates et al., 1994). In contrast, one mechanical study and the previously mentioned imaging study suggest the opposite – namely, that time constants are lower in edematous tissues (Lindahl, 1995). These studies demonstrated similar time constant measurements and similar differences between edematous and non-edematous tissues. Because of the discrepancies in the literature, more study is clearly required to produce a satisfactory conclusion. A study that combines both ultrasound and mechanical measurements on a large cohort of patients for varying degrees of edema should be able to more accurately answer these questions.

Table 2.1: Physical Examination Edema Grades

Edema Grade	**Description**
Zero to trace	No visible swelling
1+	2 mm depression, barely detectable, immediate rebound
2+	4 mm deep pit, a few seconds to rebound
3+	6 mm deep pit, 10-12 seconds to rebound
4+	8 mm deep pit, more than 20 seconds to rebound, blister or skin break

Table 2.2: Mechanical Properties of Tofu – Time Constants

Type	**Axial Strain TC (s)**	**EPR TC (s)**	**Study**
Unspecified (TT1 in study)	NA	339 (relaxation)	Righetti et al. (2005b)
Unspecified (TT1 in study)	290 (creep)	240 (creep) 340 (relaxation)	Righetti et al. (2007b)
Unspecified (TT1 in study)	270 (relaxation)	NA	*Righetti et al. (2007b)*
Unspecified (TT2 in study)	NA	50 (relaxation)	Righetti et al. (2005b)
Unspecified (TT2 in study)	56 (creep)	32 (creep) 49 (relaxation)	Righetti et al. (2007b)
Unspecified (TT2 in study)	67 (relaxation)	NA	*Righetti et al. (2007b)*
Extra firm	20 (relaxation)	NA	*Belmont et al. (2013)*

(*Italics* denotes a mechanical, rather than imaging, test)

Table 2.3: Mechanical Properties of Tofu – Shear Modulus (kPa)

Type	**Imaged**	**Mechanical Quasistatic**	**Mechanical Harmonic**	**Study**
Silken	6-7 (MR)	NA	NA	Perriñez et al. (2010a)
Soft	4.5-4.8 (MR)	0.89	6.4	Perriñez et al. (2010b)
Firm	5.1-10.6 (MR)	2	16	Perriñez et al. (2010b)
Extra Firm	7.1-14 (MR)	2.3	22	Perriñez et al. (2010b)
Extra Firm	5.4 (MR)	NA	NA	Perriñez et al. (2009)
Unspecified (fully hydrated)	0.64* (USN)	NA	NA	Righetti et al. (2004)
Unspecified (partially dehydrated)	0.69* (USN)	NA	NA	Righetti et al. (2004)
Unspecified (TT1 in study)	NA	0.67*	NA	Righetti et al. (2007b)
Unspecified (TT2 in study)	NA	1.2*	NA	Righetti et al. (2007b)

(* denotes that the shear modulus μ was computed from the Young's modulus E and Poisson's ratio ν determined by the study according to $\mu = E/2(1+\nu)$.)

Table 2.4: Mechanical Properties of Edematous Tissue – Time Constants (s)

	Tissue	Time Constant	Type	Study
Normal	Subcutis, arm and leg, normal patients (USN)	225	EPR	Righetti et al. (2007a)
	Subcutis, lower leg, normal patients	0.39	AS	Mridha and Odman (1986)
	Subcutis, contralateral arm, unilateral edema	71	AS	Bates et al. (1994)
	Subcutis, contralateral arm, unilateral edema	135	AS	Lindahl (1995)
Edematous	Subcutis, arm and leg, lymphedema patients (USN)	25	EPR	Righetti et al. (2007a)
	Subcutis, lower leg, edema patients	1.4-2.8	AS	Mridha and Odman (1986)
	Subcutis, ipsilateral arm, unilateral edema	230	AS	Bates et al. (1994)
	Subcutis, ipsilateral arm, unilateral edema	30	AS	Lindahl (1995)

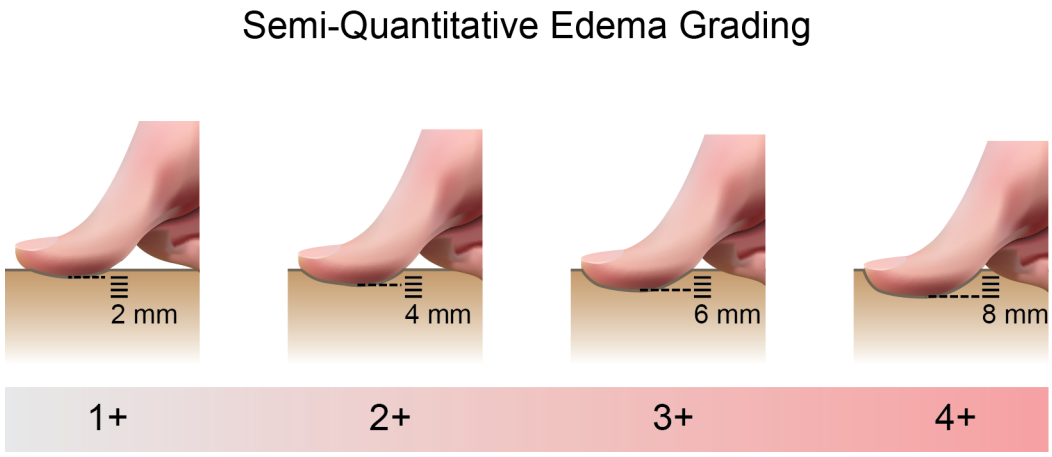

Figure 2.1: Illustration of the physical examination, or "pitting" test, for grading peripheral edema. The edematous region is compressed manually, and the degree of edema is rated on a scale of 0-4+ based on the depth and rebound time of the observed indentation in the skin.

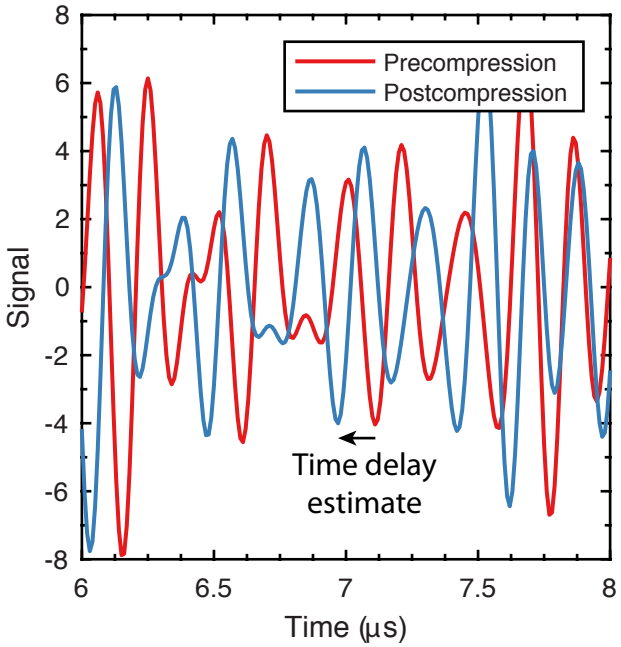

Figure 2.2: Simple graphical illustration of the speckle tracking time delay estimation. The RF ultrasound signals are shifted relative to one another by the applied compression. Normalized cross correlation can then be used to estimate the time delay for which small segments of the pre- and postcompression RF signals are most similar.

BIBLIOGRAPHY

Adriaenssens, N., Belsack, D., Buyl, R., Ruggiero, L., Breucq, C., De Mey, J., Lievens, P., and Lamote, J. (2012). Ultrasound elastography as an objective diagnostic measurement tool for lymphoedema of the treated breast in breast cancer patients following breast conserving surgery and radiotherapy. *Radiol. Oncol.*, 46(4):284–95.

Alam, S. K. and Ophir, J. (1997). On the use of envelope and RF signal decorrelation as tissue strain estimators. *Ultrasound Med. Biol.*, 23(9):1427–33.

Alam, S. K., Ophir, J., and Konofagou, E. E. (1998). An adaptive strain estimator for elastography. *IEEE Trans. Ultrason. Ferroelectr. Freq. Control*, 45(2):461–72.

Armstrong, C. G., Lai, W. M., and Mow, V. C. (1984). An analysis of the unconfined compression of articular cartilage. *J. Biomech. Eng.*, 106(2):165–73.

Arneson, T. J., Liu, J., Qiu, Y., Gilbertson, D. T., Foley, R. N., and Collins, A. J. (2010). Hospital treatment for fluid overload in the Medicare hemodialysis population. *Clin. J. Am. Soc. Nephrol.*, 5(6):1054–63.

Barbone, P. E. and Bamber, J. C. (2002). Quantitative elasticity imaging: what can and cannot be inferred from strain images. *Phys. Med. Biol.*, 47(12):2147–64.

Bates, D., Levick, J., and Mortimer, P. (1994). Quantification of rate and depth of pitting in human edema using an electric tonometer. *Lymphology*, 27(4):159–172.

Belmont, B., Dodde, R. E., and Shih, A. J. (2013). Impedance of tissue-mimicking phantom material under compression. *J. Electr. Bioimpedance*, 4(1):2–12.

Berry, G. P., Bamber, J. C., Armstrong, C. G., Miller, N. R., and Barbone, P. E. (2006a). Towards an acoustic model-based poroelastic imaging method: I. Theoretical foundation. *Ultrasound Med. Biol.*, 32(4):547–67.

Berry, G. P., Bamber, J. C., Miller, N. R., Barbone, P. E., Bush, N. L., and Armstrong, C. G. (2006b). Towards an acoustic model-based poroelastic imaging method: II. experimental investigation. *Ultrasound Med. Biol.*, 32(12):1869–85.

Berry, G. P., Bamber, J. C., Mortimer, P. S., Bush, N. L., Miller, N. R., and Barbone, P. E. (2008). The spatio-temporal strain response of oedematous and nonoedema-

tous tissue to sustained compression in vivo. *Ultrasound Med. Biol.*, 34(4):617–29.

Biot, M. A. (1941). General theory of three-dimensional consolidation. *J. Appl. Phys.*, 12(2):155–164.

Brodowicz, K. G., McNaughton, K., Uemura, N., Meininger, G., Girman, C. J., and Yale, S. H. (2009). Reliability and feasibility of methods to quantitatively assess peripheral edema. *Clin. Med. Res.*, 7(1-2):21–31.

Doyley, M. M., Meaney, P. M., and Bamber, J. C. (2000). Evaluation of an iterative reconstruction method for quantitative elastography. *Phys. Med. Biol.*, 45(6):1521–1540.

Doyley, M. M., Srinivasan, S., Pendergrass, S. a., Wu, Z., and Ophir, J. (2005). Comparative evaluation of strain-based and model-based modulus elastography. *Ultrasound Med. Biol.*, 31(6):787–802.

Goenezen, S., Barbone, P., and Oberai, A. A. (2011). Solution of the nonlinear elasticity imaging inverse problem: The incompressible case. *Comput. Methods Appl. Mech. Eng.*, 200(13-16):1406–1420.

Goenezen, S., Dord, J.-F., Sink, Z., Barbone, P. E., Jiang, J., Hall, T. J., and Oberai, A. a. (2012). Linear and nonlinear elastic modulus imaging: an application to breast cancer diagnosis. *IEEE Trans. Med. Imaging*, 31(8):1628–37.

Hogan, M. (2007). *Medical-Surgical Nursing*. Prentice Hall, Salt Lake City, 2nd edition.

Hoskins, P., Martin, K., and Thrush, A., editors (2010). *Diagnostic Ultrasound: Physics and Equipment*. Cambridge Univ Press, New York, NY, 2nd edition.

Kalantar-Zadeh, K., Regidor, D. L., Kovesdy, C. P., Van Wyck, D., Bunnapradist, S., Horwich, T. B., and Fonarow, G. C. (2009). Fluid retention is associated with cardiovascular mortality in patients undergoing long-term hemodialysis. *Circulation*, 119(5):671–9.

Kallel, F. and Bertrand, M. (1996). Tissue elasticity reconstruction using linear perturbation method. *IEEE Trans. Med. Imaging*, 15(3):299–313.

Kim, Y. T., Kim, H. C., Inada-Kim, M., Jung, S. S., Yun, Y. H., Jho, M. J., and Sandstrom, K. (2009). Evaluation of tissue mimicking quality of tofu for biomedical ultrasound. *Ultrasound Med. Biol.*, 35(3):472–81.

Konofagou, E. and Ophir, J. (1998). A new elastographic method for estimation and imaging of lateral displacements, lateral strains, corrected axial strains, and Poisson's ratios in tissues. *Ultrasound Med. Biol.*, 24(8):1183–1199.

Konofagou, E. E., Harrigan, T. P., Ophir, J., and Krouskop, T. A. (2001). Poroelasticity: Imaging the poroelastic properties of tissues. *Ultrasound Med. Biol.*,

27(10):1387–1397.

Kouw, P. M., Kooman, J. P., Cheriex, E. C., Olthof, C. G., de Vries, P. M., and Leunissen, K. M. (1993). Assessment of postdialysis dry weight: a comparison of techniques. *J. Am. Soc. Nephrol.*, 4(1):98–104.

Kruger, G. H., Dodde, R. E., Koziol, L. B., and Weitzel, W. F. (2012). Novel method and device for viscoelastic tissue characterization of edema. In *IEEE Int. Ultrason. Symp. IUS*, pages 2368–2371.

Kuei, S., Lai, W., and Mow, V. (1978). A biphasic rheological model of articular cartilage. In Eberhardt, R. and Burstein, A., editors, *Adv. Bioeng.*, page 17. American Society of Mechanical Engineers.

Leggat, J. E., Orzol, S. M., Hulbert-Shearon, T. E., Golper, T. A., Jones, C. A., Held, P. J., and Port, F. K. (1998). Noncompliance in hemodialysis: predictors and survival analysis. *Am. J. Kidney Dis.*, 32(1):139–45.

Lindahl, O. (1995). The evaluation of a biexponential model for description of intercompartmental fluid shifts in compressed oedematous tissue. *Physiol. Meas.*, 16:17–28.

Lindberg, M., Prütz, K.-G., Lindberg, P., and Wikström, B. (2009). Interdialytic weight gain and ultrafiltration rate in hemodialysis: lessons about fluid adherence from a national registry of clinical practice. *Hemodial. Int.*, 13(2):181–8.

Lubinski, M. A., Emelianov, S. Y., and O'Donnell, M. (1999). Speckle tracking methods for ultrasonic elasticity imaging using short-time correlation. *IEEE Trans. Ultrason. Ferroelectr. Freq. Control*, 46(1):82–96.

Mallick, N. P. and Gokal, R. (1999). Haemodialysis. *Lancet*, 353(9154):737–42.

Movilli, E., Gaggia, P., Zubani, R., Camerini, C., Vizzardi, V., Parrinello, G., Savoldi, S., Fischer, M. S., Londrino, F., and Cancarini, G. (2007). Association between high ultrafiltration rates and mortality in uraemic patients on regular haemodialysis. A 5-year prospective observational multicentre study. *Nephrol. Dial. Transplant*, 22(12):3547–52.

Mow, V. and Kuei, S. (1980). Biphasic creep and stress relaxation of articular cartilage in compression: theory and experiments. *J. . . .*, 102(February 1980):73–84.

Mridha, M. and Odman, S. (1986). Noninvasive method for the assessment of subcutaneous oedema. *Med. Biol. Eng. Comput.*, 24(4):393–8.

Nair, S. P. and Righetti, R. (2015). Resimulation of noise: a precision estimator for least square error curve-fitting tested for axial strain time constant imaging. *Phys. Med. Biol.*, 60(9):3515–3529.

Nair, S. P., Yang, X., Krouskop, T. a., and Righetti, R. (2011). Performance analy-

sis of a new real-time elastographic time constant estimator. *IEEE Trans. Med. Imaging*, 30(2):497–511.

National Kidney Foundation (2002). *Clinical Practice Guidelines for Chronic Kidney Disease: Evaluation, Clasification and Stratification*, volume 39.

Oberai, A. A., Gokhale, N. H., Doyley, M. M., and Bamber, J. C. (2004). Evaluation of the adjoint equation based algorithm for elasticity imaging. *Phys. Med. Biol.*, 49(13):2955–2974.

Oberai, A. A., Gokhale, N. H., and Feijoo, G. R. (2003). Solution of inverse problems in elasticity imaging using the adjoint method. *Inverse Probl.*, 19(2):297–313.

Oe, B., de Fijter, C. W., Geers, T. B., Vos, P. F., Donker, A. J., and de Vries, P. M. (2000). Diameter of inferior caval vein and impedance analysis for assessment of hydration status in peritoneal dialysis. *Artif. Organs*, 24(7):575–7.

Ophir, J., Cespedes, I., Ponnekanti, H., Yazdi, Y., and Li, X. (1991). Elastography: A quantitative method for imaging the elasticity of biological tissues. *Ultrason. Imaging*, 134:111–134.

Perriñez, P. R., Kennedy, F. E., Van Houten, E. E. W., Weaver, J. B., and Paulsen, K. D. (2009). Modeling of soft poroelastic tissue in time-harmonic MR elastography. *IEEE Trans. Biomed. Eng.*, 56(3):598–608.

Perriñez, P. R., Kennedy, F. E., Van Houten, E. E. W., Weaver, J. B., and Paulsen, K. D. (2010a). Magnetic resonance poroelastography: an algorithm for estimating the mechanical properties of fluid-saturated soft tissues. *IEEE Trans. Med. Imaging*, 29(3):746–55.

Perriñez, P. R., Pattison, A. J., Kennedy, F. E., Weaver, J. B., and Paulsen, K. D. (2010b). Contrast detection in fluid-saturated media with magnetic resonance poroelastography. *Med. Phys.*, 37(7):3518–3526.

Petrank, Y., Huang, L., and O'Donnell, M. (2009). Reduced peak-hopping artifacts in ultrasonic strain estimation using the Viterbi algorithm. *IEEE Trans. Ultrason. Ferroelectr. Freq. Control*, 56(7):1359–67.

Righetti, R., Garra, B. S., Mobbs, L. M., Kraemer-Chant, C. M., Ophir, J., and Krouskop, T. A. (2007a). The feasibility of using poroelastographic techniques for distinguishing between normal and lymphedematous tissues in vivo. *Phys. Med. Biol.*, 52(21):6525–41.

Righetti, R., Ophir, J., Garra, B. S., Chandrasekhar, R. M., and Krouskop, T. A. (2005a). A new method for generating poroelastograms in noisy environments. *Ultrason. Imaging*, 27(4):201–220.

Righetti, R., Ophir, J., and Krouskop, T. A. (2005b). A method for generating per-

meability elastograms and Poisson's ratio time-constant elastograms. *Ultrasound Med. Biol.*, 31(6):803–16.

Righetti, R., Ophir, J., Srinivasan, S., and Krouskop, T. A. (2004). The feasibility of using elastography for imaging the Poisson's ratio in porous media. *Ultrasound Med. Biol.*, 30(2):215–28.

Righetti, R., Righetti, M., Ophir, J., and Krouskop, T. A. (2007b). The feasibility of estimating and imaging the mechanical behavior of poroelastic materials using axial strain elastography. *Phys. Med. Biol.*, 52(11):3241–59.

Rodriguez, H. J., Domenici, R., Diroll, A., and Goykhman, I. (2005). Assessment of dry weight by monitoring changes in blood volume during hemodialysis using Crit-Line. *Kidney Int.*, 68(2):854–861.

Samani, A. and Plewes, D. (2004). A method to measure the hyperelastic parameters of ex vivo breast tissue samples. *Phys. Med. Biol.*, 49(18):4395–4405.

Saran, R., Bragg-Gresham, J. L., Rayner, H. C., Goodkin, D. A., Keen, M. L., Van Dijk, P. C., Kurokawa, K., Piera, L., Saito, A., Fukuhara, S., Young, E. W., Held, P. J., and Port, F. K. (2003). Nonadherence in hemodialysis: associations with mortality, hospitalization, and practice patterns in the DOPPS. *Kidney Int.*, 64(1):254–62.

Simon, B. R. (1992). Multiphase poroelastic finite element models for soft tissue structures. *Appl. Mech. Rev.*, 45(6):191–218.

Skovoroda, A. R., Emelianov, S. Y., Lubinski, M. A., Sarvazyan, A., and O'Donnell, M. (1994). Theoretical analysis and verification of ultrasound displacement and strain imaging. *IEEE Trans. Ultrason. Ferroelectr. Freq. Control*, 41(3):302–313.

Skovoroda, A. R., Emelianov, S. Y., and O'Donnell, M. (1995). Tissue elasticity reconstruction based on ultrasonic displacement and strain images. *IEEE Trans. Ultrason. Ferroelectr. Freq. Control*, 42(4):747–765.

Skovoroda, A. R., Lubinski, M. A., Emelianov, S. Y., and O'Donnell, M. (1999). Reconstructive elasticity imaging for large deformations. *IEEE Trans. Ultrason. Ferroelectr. Freq. Control*, 46(3):523–35.

Stegmayr, B. G., Brannstrom, M., Bucht, S., Dimeny, E., Ekspong, A., Granroth, B., Grontoft, K. C., Hadimeri, H., Holmberg, B., Ingman, B., Isaksson, B., Johansson, G., Lindberger, K., Lundberg, L., Lundstrom, O., Mikaelsson, L., Mortzell, M., Olausson, E., Persson, B., Svensson, L., and Wikdahl, A. M. (2006). Minimized weight gain between hemodialysis contributes to a reduced risk of death. *Int. J. Artif. Organs*, 29(7):675–80.

United States Renal Data System (2016). USRDS 2016 annual data report: Epidemiology of kidney disease in the United States. Technical report, National

Institutes of Health, National Institute of Diabetes and Digestive and Kidney Diseases, Bethesda, MD.

Varghese, T. and Ophir, J. (1996). Estimating tissue strain from signal decorrelation using the correlation coefficient. *Ultrasound Med. Biol.*, 22(9):1249–1254.

Varghese, T. and Ophir, J. (1997a). A theoretical framework for performance characterization of elastography: the strain filter. *IEEE Trans. Ultrason. Ferroelectr. Freq. Control*, 44(1):164–72.

Varghese, T. and Ophir, J. (1997b). Enhancement of echo-signal correlation in elastography using temporal stretching. *IEEE Trans. Ultrason. Ferroelectr. Freq. Control*, 44(1):173–80.

Wu, J. (2001). Tofu as a tissue-mimicking material. *Ultrasound Med. Biol.*, 27(9):1297–1300.

Yashiro, M., Kamata, T., Yamadori, N., Tomita, M., and Muso, E. (2007). Evaluation of markers to estimate volume status in hemodialysis patients: atrial natriuretic peptide, inferior vena cava diameter, blood volume changes and filtration coefficients of microvasculature. *Ther. Apher. Dial.*, 11(2):131–7.

CHAPTER 3

Theory

3.1 Introduction

In this chapter, I describe some of the important theoretical models used in poroelastography. These models provide the basis for which poroelastograms are interpreted and serve as a means of estimating physical parameters from the measured strain or displacement data. I begin with a description of the Biot model of poroelasticity (Biot, 1941). This is the oldest poroelastic theory, and it will form the basis of finite element models described in Chapter 5 and the inverse problem poroelastography algorithm detailed in Chapter 6. It can be shown that the Biot model is equivalent to the later KLM biphasic model under normal assumptions applying to soft biological tissue. Following the Biot theory, I will briefly discuss Armstrong's analytical solution of the KLM equations for unconstrained uniaxial compression of a uniform cylinder. This will form the basis of one of the parameter estimation techniques utilized in Chapter 5.

3.2 Biot Theory of Poroelasticity

The general theory of poroelasticity has its roots in soil mechanics. Soil undergoes a process called consolidation whereby the material slowly deforms in response to

an applied load. Terzaghi (1923) was the first to propose a mechanism to explain this phenomenon, basing it on assumptions of one dimensional deformation and a constant load. It was Biot (1941) who outlined the first general theory in the three dimensional case.

Consider, as Biot did, an isotropic material composed of a porous matrix saturated by a pore fluid. It is helpful to require that pores of the matrix are small enough compared to the macroscopic behavior that the material can be considered homogeneous. In addition, it is reasonable to limit the analysis to assume small strains, linearity of the stress-strain relations, and reversibility of the equilibrium stress-strain relationship.

3.2.1 Constitutive Relationships

We begin the derivation by defining a variable ζ called the variation in fluid content that describes the increment of water volume per unit volume of the porous matrix. We also define the fluid pressure p that acts on the pore fluid. In the case that $\zeta = 0$, our material by definition will behave as a perfectly elastic solid – that is, there is no pore fluid and therefore no pore pressure ($p = 0$). We therefore expect the material to behave according to Hooke's law. Writing Hooke's law in terms of Young's modulus E and Poisson's ratio ν, we expect the following constitutive relationship between the stress tensor and the strain tensor:

$$\varepsilon_{ij} = \frac{1}{E}\left(\sigma_{ij} - \nu\left[\sigma_{kk} - \sigma_{ij}\right]\right), \tag{3.1}$$

where summation is implied over repeated indices. For a nonzero pressure, we note that isotropy requires that the pressure cannot produce any shearing strain. It must also act equally on the three principal directions. By our assumption of small strain, we may further assume a linear relationship between the strain and the pore

pressure. Letting H' denote some physical constant and δ_{ij} denote the Kronecker delta, we can then write the stress-strain-pressure relationship for a poroelastic material as

$$\varepsilon_{ij} = \frac{1}{E}\left(\sigma_{ij} - \nu\left[\sigma_{kk} - \sigma_{ij}\right]\right) + \frac{p}{H'}\delta_{ij}. \tag{3.2}$$

The volumetric strain $\epsilon = \varepsilon_{kk}$ can be written by summing the principal strains to give

$$\epsilon = \varepsilon_{11} + \varepsilon_{22} + \varepsilon_{33} = \frac{1}{E}\left(1 - 2\nu\right)\sigma_{kk} + \frac{3p}{H'}. \tag{3.3}$$

Solving equation 3.3 for σ_{kk} and defining $H' = 3H$ (for convenience) yields

$$\sigma_{kk} = \frac{E}{1-2\nu}\left(\epsilon - \frac{p}{H}\right). \tag{3.4}$$

This now allows us to determine the stress tensor for our poroelastic material. We combine equations 3.2 and 3.4, rearranging terms to solve for the stress. This yields

$$\sigma_{ij} = 2G\left(\varepsilon_{ij} + \frac{\nu\epsilon}{1-2\nu}\right) - \alpha p\delta_{ij}. \tag{3.5}$$

Here, we have defined two new constants – the shear modulus G and the Biot-Willis coefficient α. The shear modulus is not independent from the parameters E and ν. Rather, it can be written as a combination of the two – specifically,

$$G = \frac{E}{2(1+\nu)}. \tag{3.6}$$

The Biot-Willis coefficient α, as we shall later show, is a measure of the ratio of the fluid volume change to the total volume change of the porous matrix. It can be written in terms of the shear modulus and Poissons ratio, or alternatively in terms

of the bulk modulus K, and the poroelastic constant H as

$$\alpha = \frac{2(1+\nu)G}{3(1-2\nu)H} = \frac{K}{H}. \tag{3.7}$$

Let us now turn our attention back to the variation of fluid content ζ. As the simplest possible assumption, we take ζ to have the general linear form

$$\zeta = a_1\sigma_{11} + a_2\sigma_{22} + a_3\sigma_{33} + a_4\sigma_{12} + a_5\sigma_{13} + a_6\sigma_{23} + a_7 p. \tag{3.8}$$

As before, we make use of the isotropy assumption to eliminate shear terms ($a_4 = a_5 = a_6 = 0$). Since all three principal stresses must have equivalent effects on the fluid content, we are left with the following expression for the variation of fluid content:

$$\zeta = \frac{1}{H_1'}\sigma_{kk} + \frac{1}{R}p, \tag{3.9}$$

where H_1' and R are physical poroelastic constants. Assuming that the material has potential energy – this follows naturally if we assume the stress-strain relationship is reversible – it can be shown that $H_1' = H' = 3H$ (Biot, 1941). Combining equations 3.4 and 3.8, we can express the fluid content as a function of the volumetric strain and the pore pressure. After some algebraic manipulations, we obtain

$$\zeta = \alpha\epsilon + \frac{1}{M}p, \tag{3.10}$$

where $1/M = 1/R - \alpha/H$ is sometimes called the Biot modulus.

3.2.2 Physical Interpretation of the Poroelastic Parameters

It is worth mentioning now that we still have two unique poroelastic constants we have not fully defined: H and R, which enter our constitutive equations through

the Biot-Willis coefficient α and the Biot modulus $1/M$. In general, these represent physical constants that must be measured by experiment. In the case of an ideal porous solid, however, we can derive expressions for these in terms of more familiar material properties such as porosity, compressibility, and bulk modulus. By an ideal porous solid, we mean a material composed of a homogeneous, isotropic solid matrix containing a fully connected pore space. It turns out that such materials exhibit a very useful property. Consider applying a known confining pressure P' to the material while holding the fluid pore pressure at an equal magnitude – a useful thought experiment Detournay and Cheng (1993) termed a "Π-loading". Biot referred to this as an *unjacketed test*, and it is sometimes also referred to as an *undrained test*. Under a Π-loading, the solid matrix and pore space of an ideal porous solid deform with a uniform volumetric strain. This means that the porosity of an ideal porous solid is constant under a Π-loading, making our analysis much simpler.

Our first goal is to derive a simple physical interpretation of the Biot-Willis coefficient α. We imagine applying a Π-loading with an all around confining pressure P' to an ideal porous material. In other words, the three principle stresses all equal $-P'$ (where the negative denotes compression). It follows that the sum of the principle stresses can be written

$$\sigma_{kk} = \sigma_{11} + \sigma_{22} + \sigma_{33} = -3P'. \tag{3.11}$$

We now employ an equivalent form of equation 3.4, expressed in terms of the bulk modulus rather than the Youngs modulus and Poissons ratio

$$\sigma_{kk} = 3K\left(\epsilon - \frac{p}{H}\right). \tag{3.12}$$

By virtue of our chosen Π-loading, we can make some substitutions into equation

3.12. First, the pore pressure $p = P'$, and second, $\sigma_{kk} = -3P'$ from equation 3.11. Finally, we recall that for a Π-loading, the volumetric strain is uniform – that is, the volumetric strain in the bulk porous material is equal to the volumetric strain in the solid phase alone. These substitutions yield

$$-3P' = 3K\left(\epsilon_s - \frac{P'}{H}\right). \tag{3.13}$$

Focusing our attention on the solid components of our porous material only, we use the definition of the bulk modulus to describe the volumetric strain in the solid

$$-\epsilon_s \equiv -\left(\frac{\Delta V}{V}\right)_s = \frac{P'}{K_s}, \tag{3.14}$$

where V denotes volume and K_s is the bulk modulus of a homogeneous (non-porous) volume of the solid matrix material. Combining equations 3.6, 3.13, and 3.14 and rearranging, we find that

$$\alpha = 1 - \frac{K}{K_s}. \tag{3.15}$$

This means that α can be thought of as a measure of the relative compressibility of the solid matrix material itself and that of the porous material as a whole. In the case of an incompressible solid phase, K_s approaches infinity and we find that $\alpha = 1$.

We now turn our attention to the Biot modulus $1/M$. We know from equation 3.10 that this constant relates the variation of fluid content to the volumetric strain and pore pressure. In fact, the Biot modulus can be defined very precisely as the change in fluid content with respect to pressure under conditions of constant volumetric strain. We start therefore by considering changes in the pore fluid volume. If the pore space of our porous solid is saturated, the pore volume V_p and fluid

volume V_f are equal. The same holds for any changes in those two volumes. We can then write the decomposition

$$\frac{\Delta V_p}{V_p} = \frac{\Delta V_f}{V_f} = \frac{\Delta V_f^{(1)}}{V_f} + \frac{\Delta V_f^{(2)}}{V_f}, \tag{3.16}$$

where $\Delta V_f^{(1)}$ is associated with volume changes due to dilatation of the pore fluid and $\Delta V_f^{(2)}$ is due to fluid exchange between the pore space and the environment. By the definition of compressibility χ_f of the pore fluid

$$\frac{\Delta V_f^{(1)}}{V_f} = -\chi_f p. \tag{3.17}$$

We recall now that the variation in fluid content ζ describes the increment of water volume per unit volume of the porous matrix. That is,

$$\zeta \equiv \frac{\Delta V_f^{(2)}}{V_f}. \tag{3.18}$$

This is very close to the form seen in equation 3.16. Using the porosity of the material ϕ, defined as the ratio of pore volume to total volume, we can write equation 3.18 in terms of the total fluid volume (again noting that for a saturated pore space $V_p = V_f$)

$$\zeta = \frac{V_f}{V} \cdot \frac{\Delta V_f^{(2)}}{V_f} = \phi \frac{\Delta V_f^{(2)}}{V_f} \tag{3.19}$$

Substituting equations 3.17 and 3.19 into equation 3.16, noting that the left hand side of the equation is equal to the volumetric strain in the pore space, we obtain

$$\epsilon_p = -\chi_f + \frac{\zeta}{\phi} \tag{3.20}$$

We now use equation 3.9 to eliminate ζ from equation 3.20. With some mild rear-

ranging, this yields

$$\phi\epsilon_p = -\phi\chi_f p + \alpha\epsilon + \frac{1}{M}p, \tag{3.21}$$

As we did for the Biot-Willis coefficient, we now imagine applying a Π-loading to our ideal porous material. Recall that for a Π-loading, the following hold: (1) p equals a uniform confining pressure P' and (2) $\epsilon_p = \epsilon = \epsilon_s$. Applying these conditions to equation 3.21, we obtain

$$\phi\epsilon_s = -\phi\chi_f P' + \alpha\epsilon_s + \frac{1}{M}P'. \tag{3.22}$$

which can then be simplified further using equation 3.13:

$$-\phi\frac{P'}{K_s} = \left(-\phi\chi_f - \alpha\frac{1}{K_s} + \frac{1}{M}\right)P'. \tag{3.23}$$

From here, we eliminate P' and solve for the Biot modulus

$$\frac{1}{M} = \phi\chi_f + (\alpha - \phi)\frac{1}{K_s}, \tag{3.24}$$

or, equivalently, making use of our definition of α (equation 3.15),

$$\frac{1}{M} = \phi\chi_f + (\alpha - \phi)\frac{1-\alpha}{K}. \tag{3.25}$$

The poroelastic parameters now have clear physical interpretations, fully expressible in terms of the mechanical properties of the constituent materials (solid, fluid, and bulk matrix) and their internal structure (porosity). This will be particularly beneficial to poroelastography studies as we shall discuss later since it allows us to more easily make material assumptions. For example, we can consider the case where the bulk porous material is much more compressible than an equivalent block of the non-porous solid ($K_s \ll K$), which yields the case $\alpha = 1$ (from

equation 3.15). We might also assume that the pore fluid has the same properties as water. In many applications ranging from soil dynamics to poroelastography this is indeed the case. The constitutive equations under these assumptions then involve only bulk material properties (G, ν, K, ϕ) and one poroelastic parameter $1/M$ that we can calculate rather than measure.

3.2.3 Governing Equations

We now have a full constitutive model for our poroelastic material. That is, we can describe how stresses, strains, and pressures relate to each other. However, we do not yet have a closed system of equations that we can solve. This requires two equations: (1) an equilibrium equation for the stress and (2) an evolution equation for the pore pressure.

We start by assuming that the deformation of our poroelastic material can be described as quasi-static. That is, we require that deformation to an equilibrium state occurs very quickly, particularly when compared to the timescale over which the pore fluid pressure changes. This allows us to enforce an equilibrium condition. The equilibrium condition is identical to that for an elastic solid, in accordance with Cauchy's momentum equation. If we neglect gravitational effects, the divergence of the total stress tensor must equal zero:

$$\sigma_{ij,j} = 0. \tag{3.26}$$

Applying this to equation 3.5, this leads to the equilibrium pressure-strain relationship

$$2G\left(\varepsilon_{ij,j} + \frac{\nu}{1-2\nu}\epsilon_{,i}\right) - \alpha p_{,i} = 0, \tag{3.27}$$

or equivalently using the bulk modulus K instead of Poissons ratio ν

$$2G\varepsilon_{ij,j} + \left(K + \frac{2}{3}G\right)\epsilon_{,i} - \alpha p_{,i} = 0. \tag{3.28}$$

This equation has three components, one for each of the three spatial dimensions, and allows us to relate the fluid pore pressure to the displacement field u_i, since $\varepsilon_{ij} = (u_{i,j} + u_{j,i})/2$. We therefore have four unknowns – the three displacements u_i and the pore pressure p.

To close the system of equations, we now derive an equation for the evolution of the pore pressure. The pressure evolution is a time-dependent equation, but one that varies on a much slower time scale than the deformation. It is in this sense that the time-dependent behavior – for example, in the consolidation of soil or the creep response of biological tissue – enters the problem even though the deformation is assumed to be quasi-static. We begin by noting that continuity requires that the variation of fluid content is dependent on the volumetric flux q_i of fluid into and out of the porous matrix. Mathematically, we can write this relationship as

$$\frac{\partial \zeta}{\partial t} + q_{i,i} = 0. \tag{3.29}$$

Now we note that the volumetric flux of fluid moving through a porous matrix is described by Darcys law. If κ is the permeability of the porous matrix (with units of m^2) and μ is the viscosity of the pore fluid, then Darcys law states that the volumetric flux is proportional to the pressure gradient

$$q_i = -\frac{\kappa}{\mu} p_{,i}. \tag{3.30}$$

Combining equations 3.10, 3.29, and 3.30 gives the pressure evolution equation

$$\frac{1}{M}\frac{\partial p}{\partial t} - \frac{\kappa}{\mu}p_{,ii} = -\alpha\frac{\partial \epsilon}{\partial t}. \tag{3.31}$$

We now have enough equations to solve for all the unknown variables - three equations for the displacement components u, v, and w, and one equation for the pressure p - for some deformation problem. Table 3.1 gives a summary of the variables, parameters, and governing equations for poroelastic deformation.

3.3 Armstrong's Solution to the Kuei-Lai-Mow Model

The Kuei-Lai-Mow (KLM) biphasic model was developed in the 1980s to describe the behavior of articular cartilage (Kuei et al., 1978; Mow and Kuei, 1980; Mow and Lai, 1980). The KLM model provides separate equations for fluid and solid phases of a porous material saturated with a fluid. This differs from the Biot theory which does not explicitly treat the two phases separately. Under specific conditions, namely that both phases are incompressible, the KLM model and the Biot model are equivalent (Simon, 1992). Armstrong et al. (1984) developed an analytical solution to the KLM model for the unconfined compression of a biphasic cylinder. This analytical solution has been used extensively in poroelastography studies. In this section, I will briefly review the governing equations of the KLM model and Armstrong's solution for the stress relaxation and creep responses, insofar as they are used in poroelastography.

The KLM model defines stress-strain relations separately for the solid porous matrix and the pore fluid as

$$\sigma_{ij}^{s} = -\alpha p\delta_{ij} + \lambda\epsilon\delta_{ij} + 2\mu\varepsilon_{ij} \tag{3.32}$$

and

$$\sigma_{ij}^f = -p\delta_{ij}, \tag{3.33}$$

where λ and μ are the first Lamé parameter and shear modulus, respectively, and all other variables are defined similarly to the previous section. The only exception is the definition of α, which now denotes the ratio of solid volume to fluid volume and is related to the porosity ϕ by the relationship $1 + \alpha = \phi^{-1}$. The total stress is related to the individual phases by

$$\sigma_{ij}^t = \sigma_{ij}^s + \sigma_{ij}^f. \tag{3.34}$$

For these constitutive equations, conservation of mass and momentum for the mixture can be written

$$\text{div } \mathbf{v}^f + \alpha \text{div } \mathbf{v}^s = 0, \tag{3.35}$$

$$\text{div } \boldsymbol{\sigma}^s - \frac{1}{k(1+\alpha)^2}(\mathbf{v}^s - \mathbf{v}^f) = 0, \tag{3.36}$$

$$\text{div } \boldsymbol{\sigma}^f + \frac{1}{k(1+\alpha)^2}(\mathbf{v}^s - \mathbf{v}^f) = 0, \tag{3.37}$$

$$\text{div } \boldsymbol{\sigma}^t = 0, \tag{3.38}$$

where $\mathbf{v}^f$ and $\mathbf{v}^s$ are the fluid and solid phase velocities, respectively, and k is the permeability in units of $\text{m}^4\text{N}^{-1}\text{s}^{-1}$, related to the Biot permeability by $k = \kappa/\mu_f$.

In his solution, Armstrong considers the unconfined compression of a cylinder of radius a under small (infinitesimal) strain. The displacement and pressure fields are assumed to be axisymmetric, and it is assumed that the axial strain is uniform. Under these assumptions, the strain tensor in cylindrical coordinates is diagonal with nonzero components

$$\varepsilon_{rr} = \frac{\partial u}{\partial r}, \quad \varepsilon_{\theta\theta} = \frac{u}{r}, \quad \varepsilon_{zz} = \varepsilon(t). \tag{3.39}$$

This allows us to simplify the conservation of mass equation (3.35). Because of the small strain assumption, the temporal and space derivatives may be interchanged, allowing us to write

$$\left(\frac{\partial v_r^f}{\partial r} + \frac{v_r^f}{r} + \frac{\partial v_z^f}{\partial z}\right) + \alpha \frac{\partial}{\partial t}\left(\frac{\partial u}{\partial r} + \frac{u}{r} + \varepsilon(t)\right) = 0. \tag{3.40}$$

This equation can be integrated with respect to r and used together with the simplified governing equations to express a single equation relating the axial strain history $\varepsilon(t)$ to the radial displacement u:

$$\frac{\partial^2 u}{\partial r^2} + \frac{1}{r}\frac{\partial u}{\partial r} - \frac{u}{r^2} = \frac{1}{H_a k}\frac{\partial u}{\partial t} + \frac{1}{H_a k}\frac{r}{2}\frac{\partial \varepsilon}{\partial t}, \tag{3.41}$$

where $H_A = \lambda + 2\mu$ is the aggregate modulus.

For stress relaxation, the strain history $\varepsilon(t) = \varepsilon_0$ is a known constant, while for creep, the following integral constraint is imposed:

$$\int_0^a \sigma_{zz}^t 2\pi r dr = F(t). \tag{3.42}$$

Because the deformation is infinitesimal, the upper limit of the integral a may be treated as a constant defined by the reference configuration of the material. Under large strain, this assumption would not hold and the upper limit becomes a function of time.

Taking the Laplace transform of Equation 3.41 yields an ordinary differential equation in r, the solution of which may be written in terms of Bessel functions. The Heaviside Expansion Theorem can then be used to invert the solution to obtain the solution of the equation in the original time domain.

In the stress relaxation case, this yields an equation for the mean radial strain

in the cylinder,

$$\frac{u}{a}(a,t) = \varepsilon_0 \left[\nu + (1-2\nu)(1-\nu) \sum_{n=1}^{\infty} \frac{\exp\left(-\alpha_n^2 \frac{H_a k t}{a^2}\right)}{\alpha_n^2 (1-\nu)^2 - (1-2\nu)} \right], \tag{3.43}$$

where

$$H_a = \frac{E(1-\nu)}{(1+\nu)(1-2\nu)}, \tag{3.44}$$

and α_n are the roots of the characteristic equation

$$J_1(x) - (1-\nu)\frac{x J_0(x)}{1-2\nu} = 0. \tag{3.45}$$

The creep case yields an equation for the strain history,

$$\begin{aligned} \varepsilon(t) = -\frac{F_0}{E\pi a^2} \Big[& 1 - (1-\nu^2)(1-2\nu) \\ & \sum_{n=1}^{\infty} \frac{4}{9(1-\nu^2)\beta_n^2 - 8(1+\nu)(1-2\nu)} \exp\left(-\beta_n^2 \frac{H_a k t}{a^2}\right) \Big] \end{aligned} \tag{3.46}$$

where β_n are the roots of

$$J_0(x) - \frac{4(1-2\nu)}{3(1-\nu)} \frac{J_1(x)}{x} = 0. \tag{3.47}$$

Poroelastography studies typically employ these equations in curve fitting routines to estimate poroelastic parameters from ultrasound strain measurements. In addition, Equations 3.43 and 3.46 can be rearranged to obtain expressions for the mean radial-to-axial strain ratio in the cylinder. This value, also termed the effective Poisson's ratio (EPR), approaches the Poisson's ratio ν as $t \to \infty$ and gives an additional useful interpretation for the time evolution of poroelastograms.

Table 3.1: Summary of the Biot poroelasticity parameters and equations

Material parameters	K	Matrix bulk modulus
	G	Matrix shear modulus
	K_s	Solid bulk modulus
	κ	Matrix permeability
	ϕ	Matrix porosity
	χ_f	Fluid compressibility
	μ	Fluid viscosity
Poroelastic parameters	$\alpha = 1 - \frac{K}{K_s}$	Biot-Willis coefficient
	$\frac{1}{M} = \phi\chi_f + (\alpha - \phi)\frac{1-\alpha}{K}$	Biot Modulus
Governing equations	$2G\varepsilon_{ij,j} + \left(K - \frac{2}{3}G\right)\epsilon_{,i} - \alpha p_{,i} = 0$	Equilibrium equations
	$\frac{1}{M}\frac{\partial p}{\partial t} - \frac{\kappa}{\mu}p_{,ii} = -\alpha\frac{\partial \epsilon}{\partial t}$	Pressure evolution equation
Unknown variables	u, v, w	Displacement field
	p	Pore fluid pressure

BIBLIOGRAPHY

Armstrong, C. G., Lai, W. M., and Mow, V. C. (1984). An analysis of the unconfined compression of articular cartilage. *J. Biomech. Eng.*, 106(2):165–73.

Biot, M. A. (1941). General theory of three-dimensional consolidation. *J. Appl. Phys.*, 12(2):155–164.

Detournay, E. and Cheng, A.-D. (1993). Fundamentals of poroelasticity. In Hudson, J. A., Brown, E. T., Fairhurst, C., and Hoek, E., editors, *Compr. Rock Eng. Princ. Pract. Proj.*, chapter 5, pages 113–171. Pergamon Press, Oxford, 1 edition.

Kuei, S., Lai, W., and Mow, V. (1978). A biphasic rheological model of articular cartilage. In Eberhardt, R. and Burstein, A., editors, *Adv. Bioeng.*, page 17. American Society of Mechanical Engineers.

Mow, V. and Kuei, S. (1980). Biphasic creep and stress relaxation of articular cartilage in compression: theory and experiments. *J. . . .*, 102(February 1980):73–84.

Mow, V. and Lai, W. (1980). Recent developments in synovial joint biomechanics. *Siam Rev.*, 22(3).

Simon, B. R. (1992). Multiphase poroelastic finite element models for soft tissue structures. *Appl. Mech. Rev.*, 45(6):191–218.

Terzaghi, K. (1923). Die berechnung der durchlassigkeitsziffer des tones aus dem verlauf der hydrodynamischen spannungserscheinungen. *Math. Klasse*, 132:125–138.

CHAPTER 4

Design and testing of a single-element ultrasound viscoelastography system for point-of-care edema quantification

4.1 Introduction

Parts of this chapter have been published in "Design and testing of a single-element ultrasound viscoelastography system for point-of-care edema quantification", Ultrasound in Medicine and Biology (Pitre, Jr et al., 2016). As discussed earlier, careful monitoring of patient fluid overload is an essential part of standard care for patients with end stage renal disease (ESRD). Current monitoring techniques rely primarily on palpation to grade the degree of peripheral edema as an indication of fluid overload. This method provides an inadequate assessment, and fully quantitative methods based on new technologies have the potential to substantially improve patient fluid balance monitoring by providing a more consistent, observer-independent measurement (Kouw et al., 1993; Oe et al., 2000; Yashiro et al., 2007). A number of studies have proposed the use of ultrasound elastography as a potential tool for measuring the mechanical properties of edematous tissue (Righetti et al., 2007; Berry et al., 2008; Adriaenssens et al., 2012; Kruger et al., 2012).

Standard ultrasound elastography techniques rely on assumptions of stress

uniformity and linear elasticity. Biological tissue is more accurately described as poroelastic or viscoelastic, and various models have been developed to describe the stress-strain response of tissue under compression (Kuei et al., 1978; Mow and Kuei, 1980; Armstrong et al., 1984; Fung, 1993). Ultrasound viscoelastography (UVE) replaces the linear elastic tissue model with the more accurate, but still relatively simple, standard linear solid (SLS) model (Fung, 1993; Insana et al., 2004; Sridhar et al., 2007; Qiu et al., 2008). This lumped-parameter model can be represented as a collection of springs and dashpots (Figure 4.1). Under a constant stress step loading $\sigma_0 H(t)$, the SLS model exhibits the following creep response with strain ε:

$$\varepsilon(t) = \sigma_0 \left[\frac{1}{E_0} + \frac{1}{E_1} \left(1 - \exp(-t/\tau)\right) \right] H(t). \tag{4.1}$$

This simple, closed form expression for the strain response to compression is ideal for obtaining a bulk estimate of tissue properties. Point-of-care applications such as edema monitoring may benefit from such a simple tissue model.

In this chapter, I detail the development and testing of a point-of-care viscoelastography system. This system was designed around a single-element ultrasound transducer to decrease hardware complexity and computational expense. I investigated the use of this single-element viscoelastography system to quantify the viscoelastic properties of a tissue-mimicking material subjected to large strains.

4.2 Methods and Material

To demonstrate the feasibility of using UVE measurements to estimate the fluid content of edematous tissue, I conducted two similar experiments. One experiment was a standard creep compression test; the other was a creep compression test with simultaneous UVE measurements. The standard creep compression test served as a gold standard comparison for the UVE measurements. In this section,

I outline the procedure used to obtain and process data for each of these experiments.

In all experiments, I used cylindrical samples of extra-firm tofu (Nasoya, Ayer, MA) as an edematous tissue-mimicking phantom. Cylinders were cut from a single block of tofu using a 32 mm diameter tube of sharpened plastic at room temperature. Next, each cylinder was trimmed to a height of 20 ± 1 mm. This yielded a total of 12 samples per block of tofu. The samples were relatively uniform in structure although some macroscale variations in the structure (e.g. larger pores) were visibly present, as might be expected of a randomly porous material such as tofu. The samples were stored at room temperature for the course of the experiment (approximately 3 hours) in the original holes from which they were cut in the tofu block and submerged in the original preservation fluid from the tofu packaging. This ensured that the samples experienced constant structural and osmotic conditions when not in use.

During testing, individual tofu samples were submerged in a water tank and immediately subjected to a constant, step-like loading of 1.0 N (a mechanical creep test). A single-axis programmable test stand (ESM301L, Mark-10, Copiague, NY) and digital force gauge (Series 5, Mark-10, Copiague, NY) allowed for precise control of the loading. To create the step-like loading, the test stand subjected the samples to a steep ramp compression of 50 mm/min until the force gauge measured 1.0 N. After this point, the ramp loading ceased, and the test stand adjusted the loading to maintain a constant 1.0 N force for five minutes while data were collected. A schematic of the apparatus is shown in Figure 4.2. A fixture containing a single-element, 8 MHz focused ultrasound transducer made contact with the tofu samples and distributed the load uniformly across the surface of the sample. For standard creep compression tests, I used MesurGauge software (Mark-10, Copiague, NY) to collect displacement data from the test stand. As a side note, the

loading produced a steady state strain of approximately 10%. This constitutes a large strain at which nonlinear effects are not negligible. I accounted for this by using incremental strain estimation and finite strain theory in my analysis.

Although all of my experiments used the same brand and type of tofu, I did notice large variations between different blocks (Table 4.1). Because of this, I treated each pack as a separate data set and drew comparisons between standard creep compression and UVE tests for each block individually (3 total blocks). Because large strains can cause irreversible mechanical changes to the porous structure of the tofu and viscoelastic materials exhibit strong effects from loading history (Fung 1993), each tofu cylinder cut from a block was loaded only once. Half of the cylinders underwent the standard creep compression test, and the other half underwent the UVE test.

For UVE tests, I collected radio frequency (RF) ultrasound data using an in-house single-element ultrasound data acquisition system (Figure 4.3). This system was designed with point-of-care applications in mind where conventional high frame rates are not required, and minimizing device complexity is desirable. The design of this ultrasound system minimizes the dedicated hardware necessary compared with typical ultrasound systems. A 32-bit MIPS microcontroller (MCU) running at 80 MHz controls all the high-level functions of the device, while a complex programmable logic device (CPLD) is responsible for low-level sequencing of the ultrasound sub-systems. The MCU is responsible for configuring the CPLD with the specific parameters necessary to create the required pulse-receive sequence, for initiating the pulse/acquisition sequence, and for reading the received RF data via an 8-bit data bus interface. Specifically, the CPLD controls the transmit pulse duration and timing for the transmit circuit control and drivers consisting of a power amplifier (PA) and drivers. The system is configured to drive a single-element 8 MHz transducer (Acetara, Longmount, CO) at a frame rate of 16

kHz. The CPLD also controls the transmit/receive switch (T/R) as well as a programmable time-gain amplifier (TGA) and reads samples from the 3 MSPS 12-Bit ADC over a 48 MHz serial peripheral interface (SPI) bus. The MCU controls the demodulator (DeMod), which is followed by integrated low pass filters to provide noise removal and control of the RF signal acquired by the ADC.

In my experiments, I acquired the analog RF signal output from a low-pass filter following the transmit/receive switch. I then applied further filtering to the RF signal using an external analog filter board. The filter board consisted of a one-pole high pass filter with a 100 Hz cutoff frequency in series with a four-pole low pass Bessel filter with a 10 MHz cutoff frequency. The filtered RF signal was digitized at a sampling rate of 100 MHz using an oscilloscope (DSO7032B, Agilent Technologies, Santa Clara, CA). Data acquisition was controlled with a MATLAB (The Mathworks, Natick, MA) script on a Windows-based workstation. The MATLAB script triggered acquisitions of 1 ms windows of data from the oscilloscope via USB at a rate of approximately 4 Hz. Each 1 ms acquisition from the oscilloscope contained multiple ultrasound A-lines.

Following data collection, the digitized RF acquisitions were segmented into individual A-lines, and A-lines within each 1 ms window were averaged together. The averaged A-lines were then filtered with a second-order Butterworth bandpass filter with cutoff frequencies of 6 and 10 MHz. The final averaged and filtered RF signals were then converted to analytic signals using the Hilbert transform. These analytic signals were used to estimate the axial displacement of the tofu as a function of depth and time using an exhaustive-search speckle tracking algorithm with a normalized cross-correlation coefficient matching criteria. The speckle tracking kernel was 1.5 mm in length, and adjacent kernels were overlapped 50%. The speckle tracking algorithm utilized a search region of 0.5 mm in both the positive and negative axial directions to coarsely estimate the most likely

displacement of each kernel. Following coarse displacement estimation, the nearest zero crossing of the analytic signal phase was computed and defined as the final displacement estimate. The resulting displacement fields were cropped to include only depths of 5-15 mm (to exclude near field and far field), processed with a 2.3 mm local outlier filter (Westerweel and Scarano, 2005), and smoothed with a 1 mm median filter along the axial direction. The differential Green-Lagrange strain was computed from an ensemble average of the displacement fields using a simple finite difference (Equation 4.2). In Equation 4.2, w_m^n denotes the axial displacement at position k for ultrasound frame n, and z_k^0 denotes the axial position k in the reference (uncompressed) configuration. The Green-Lagrange strain is a metric used to describe large strains, usually those greater than 5%. I chose to use this metric to analyze my data since the measured strains were on the order of 10-15%. By integrating the differential strain function in time, I obtained the time-dependent Green-Lagrange strain function (Ammann et al., 2005). Creep curves were generated for both standard creep compression data and UVE data. Standard creep curves were computed from the displacement of the test stand, and UVE creep curves were generated by averaging the UVE strain function at all depths.

$$dE_k^n = \frac{\partial w}{\partial z} + \frac{1}{2}\left(\frac{\partial w}{\partial z}\right)^2 \approx \frac{w_k^n - w_{k-1}^n}{z_k^0 - z_{k-1}^0} + \frac{1}{2}\left(\frac{w_k^n - w_{k-1}^n}{z_k^0 - z_{k-1}^0}\right)^2 \tag{4.2}$$

The mechanical properties of the tofu were estimated by assuming that a modified version of the SLS viscoelastic model (Figure 4.1) could describe the material (Fung, 1993). This model is commonly used to model the behavior of viscoelastic materials in one dimension. The SLS model describes a solid as a combination of elastic (spring) and viscous (dashpot) elements. The strain in a standard linear solid in response to a constant stress σ_0 applied impulsively at time t_0 is given by Equation 4.1 (that is, applied as a Heaviside step function $H(t)$). The response depends upon three material properties: the elastic moduli E_0 and E_1 and the time

constant $\tau = E_1/\eta_1$. Note that the time constant contains the viscous constant η_1. In tissue, this means that the time constant carries information about fluid content and tissue porosity. The model was fit to the UVE ensemble creep curves at each depth using a nonlinear least squares trust-region fitting procedure (MATLAB Curve Fitting Toolbox, The Mathworks, Natick, MA). The fitting procedure yielded three material parameters for each data set – two elastic moduli (E_0 and E_1) and one time constant τ.

4.3 Results

Figure 4.4 shows the ensemble Green-Lagrange strain as well as the minimum correlation image for each of the three blocks of tofu used. The Green-Lagrange strain is displayed as a set of creep curves at various depths throughout the tofu. The minimum correlation images are displayed in an m-mode configuration with time on the horizontal axis and depth on the vertical axis. The ensemble strain shows clear depth dependence with larger strains closer to the upper surface (where the stress was applied) decaying to smaller strains nearer to the lower surface.

At each depth, the creep curves generated resemble the rising exponential function modeled by the SLS model (Equation 4.1). To illustrate this, Figure 4.5 shows some examples of the UVE strain and corresponding curve fits at depths of 5, 7.5, 10, 12.5, and 15 mm from one tofu block (labelled C in Figure 4.4). From these curve fits, we obtained time constants and elastic moduli for each depth (Figures 4.6-4.8 and Table 4.2). The instantaneous elastic modulus E_0 showed a slight upward trend with depth and median values of 15.5, 21.6, and 12.3 kPa for tofu blocks A-C, respectively. The secondary elastic modulus E_1 also showed a slight upward trend with depth and median values of 28.0, 42.5, and 18.9 kPa. Finally, the time constant showed large variations with some large spikes. Median values were 18.7,

8.7, and 30.3 s.

For comparison with these UVE measured parameters, Figure 4.9 shows creep curve data and fits obtained using displacement data from the mechanical test stand. These represent the mean behavior of the tofu samples as a whole. The viscoelastic parameter estimates obtained via curve fitting are given in Table 4.1. In general, the mechanical curve fits produced elastic moduli slightly smaller than those estimated by UVE. In contrast, the time constants obtained from the mechanical curve fits tended to be much larger than the UVE estimates.

To further describe the depth dependent strain and aid in validating this UVE system, it is useful to compare the steady state strain at each depth to a theoretical prediction. Figure 4.10 shows the steady state strain (at time t = 300 s) as a function of depth in tofu block A. For comparison, it also shows a numerical prediction based on a finite element model. The finite element model simulated axisymmetric compression of a cylinder with radius 16 mm, height 20 mm, a Young's modulus of 10 kPa, Poisson's ratio of 0.3, permeability of 10^{-11} $m^4N^{-1}s^{-1}$, and loading force of 1.0 N. The boundary conditions were defined as a no-slip condition on the top surface, a roller condition on the bottom, and atmospheric pressure on the sides. The material properties and boundary conditions used are simply meant to exhibit, for illustrative purposes, a *plausible* set of conditions for the experiment. The behavior of the UVE measured strain closely matches the predictions of the numerical model.

The correlation coefficient produced at each point in space and time by the speckle tracking algorithm provides a useful quality metric for the strain estimation. Each tofu sample in an ensemble yielded a correlation image. The minimum correlation of all displacement estimates included in an ensemble was chosen as a conservative quality metric (Figure 4.4). Regions of low correlation, defined here as less than or equal to 0.9, are indicative of large changes in speckle characteristics

between consecutive frames. In all experiments, I observed some low correlation during the initial compression. This is likely due to the higher strain rate causing larger changes in the speckle pattern between ultrasound frames. Speckle tracking of tofu block B resulted in noticeably lower correlations (shown in purple) throughout the experiment. Over the course of the experiments, tracking of tofu blocks A and C resulted in a mean estimated elastographic signal-to-noise ratio (SNRs) (Lindop et al., 2008; Treece et al., 2011) of 30.6 and 30.5 dB, respectively, while tofu block B resulted in a mean SNRs of 28.2 dB.

As a final metric of quality, I compared the creep curves obtained by standard creep tests to those obtained by averaging the UVE generated creep curves over all depths at each time point (Figure 4.11). In all three cases, UVE underestimated the mean strain with a maximum absolute error of approximately 4% for tofu block B and 2% for tofu blocks A and C.

4.4 Discussion

The data suggest that this UVE method can accurately estimate strain, including depth dependence, in a viscoelastic tissue mimicking material. This is most clear when comparing the depth-averaged UVE generated creep curves with the results of standard mechanical creep testing (Figure 4.11). The small errors (2-4%) show that in an average sense, the system can accurately measure the compression-induced strain in tofu samples. More importantly though, it can also accurately quantify depth dependent changes in strain. As shown in Figure 4.4 and highlighted in Figure 4.10, the steady state strain in each tofu block decreased with depth. This depth dependence cannot be fully explained by the data available in this study, but plausible answers are easy to evaluate. The results of the finite element model show that differences in boundary conditions may lead to observed

depth dependent strain even for cylinders with spatially uniform material properties. This is due to fluid pressure inside the porous tofu structure acting as a support for the solid matrix, thus resulting in lower observed strains (Figure 4.12). This explanation is not without caveats however. The material properties used in the finite element model may not be the best fit to the data – they only represent a reasonable set of values. Likewise, there is no way to verify the boundary conditions assumed by the model compared to the experiments. The boundary condition assumptions may be reasonable though, expecially since the top compressor was substantially rougher than the lower one (3D printed vs smooth plastic, respectively).

In addition, the random porous structure of tofu could lead to spatial variations that cannot be predicted theoretically. While the UVE measurement shows much more variation and noise than the numerical prediction, the same general trend is observed. Alternatively, other material effects such as consolidation of the porous structure over time or different surface material properties could play a role in the observed depth dependence.

This UVE method also performed well when considering two quality metrics: the speckle tracking correlation coefficient and the elastographic signal-to-noise ratio. As mentioned earlier, decreased correlation is indicative of changes in the speckle pattern and therefore less reliable displacement estimation. This manifests itself as errors in the strain field which will affect the viscoelastic curve fits. In Figure 4.4, it was observed that the high initial strain rates during the step compression may have caused decreased correlation. As seen in Figure 4.11, however, this initial decreased correlation did not seem to negatively affect the UVE measured strains, at least in tofu blocks A and C. Lower correlation and SNRs for tofu block B were observed at all times, especially for depths below 10 mm. This is the most likely mechanism for the strain measurement errors seen in tofu block B

(Figure 4.11).

The decreased correlation in tofu block B also may explain some of the differences in the estimation of the elastic moduli E_0 and E_1. When performed for data from tofu block B, the curve fitting procedure estimated values of E_0 and E_1 that were slightly higher than blocks A and C (21.6 kPa versus 15.5 kPa and 12.3 kPa for E_0, and 42.5 kPa versus 28.0 kPa and 18.9 kPa for E_1). These same differences were not present in the mechanically measured moduli.

The previous analyses suggest successful benchtop validation for this point-of-care UVE system. I have shown that depth dependent maps of tissue strain and viscoelastic properties can be generated for a tissue mimicking material. Although these laboratory tests demonstrate the possible usefulness of this point-of-care UVE system, clinical studies must be able to show the system can be used to improve patient care. That is, UVE measurements of tissue time constants and elastic moduli must be able to guide clinical decision making by providing a consistent, quantitative metric for grading peripheral edema. Ideally, this would take the form of an estimated volume of mobilizable fluid that could be removed from the edematous limb to reach dry weight. Theoretically, the time constant should provide some insight into excess fluid volumes. Such an analysis was outside the scope of this study but should be the focus of future clinical studies that may investigate the correlation between UVE-measured time constants and elastic moduli and the degree of clinical edema observed in patients.

The transition from the controlled laboratory environment to the clinic raises a number of challenges for this imaging system. Perhaps chief among these is the sensitivity to poorly defined geometry within the edematous limb. In vivo, the lack of a 2D image from this single-element ultrasound system may make it difficult for clinicians to identify suitable regions of interest for UVE edema measurements. Additionally, the test geometry described in this study, where the tissue

is compressed between two hard, parallel surfaces, may not always be available clinically. I envision this system being used to take UVE measurements on the lower calf of patients, where the tibia may provide a hard lower surface for the compression. In general, however, this will not provide a parallel surface to the upper compressor and may result in out-of-plane motion that may confound this one-dimensional measurement through large decorrelation errors. The two problems previously mentioned are likely surmountable provided the clinician receives adequate training in choosing a region of interest and applying the compression. Future clinical studies mimicking the image processing algorithms of this system (tracking motion along a single A-line) using an array transducer could clarify the extent of this these challenges. Finally, tissue is not isotropic, and slip boundaries between different layers of tissue (skin, fat, fascia, muscle, bone, etc.) may lead to discontinuities in the speckle tracking process. This will likely manifest itself as errors in the depth-dependent creep curves. This can possibly be compensated for by a more clever integration of the differential Green-Lagrange strain field that integrates along material path lines defined by the displacement estimates. Future clinical studies should explore the impact of these challenges on the system for UVE measurements in vivo.

Other mechanical parameters may prove to be useful to classifying edema and may be less susceptible to errors when compared to elastic and viscous moduli. The compressibility of a material, defined as the volumetric response to a pressure change, naturally lends itself to a description of edematous tissue. In response to an applied stress, fluid movement out of edematous tissue leads to a volume change in the compressed region of interest. This volumetric response can be described as a function of Poisson's ratio or measured directly. Poroelastography methods provide a natural avenue for determining the Poisson's ratio and the Poisson's ratio time constant. The application of these methods to edema monitoring

may therefore lead to useful metrics for tissue fluid content.

4.5 Conclusions

In this study, I tested a simplified single-element viscoelastography system for point-of-care edema monitoring. This system has the potential to reduce hardware complexity as well as computational expense. Using this system, I measured the viscoelastic properties of a tissue-mimicking material (tofu) in creep tests under large strains, as would be used clinically to diagnose edema. The Green-Lagrange strain creep curves generated for all depths in the tofu samples could be described accurately by the SLS model. Using this model, I demonstrated that the UVE system was capable of generating depth-dependent maps of viscoelastic material parameters including time constants and elastic moduli. A quality analysis of my results showed that the speckle tracking algorithm produced a good estimate of the internal displacement field with high correlation and SNRs. Estimates of the mean creep response were highly sensitive to tracking errors, and experiments with lower SNRs showed poor agreement with the creep response measured using a standard creep compression test. My results suggest successful benchtop validation of this UVE system. Future clinical studies will be required to fully establish the feasibility of using this method and ultrasound system for edema monitoring. This translation to the clinic will bring with it a number of challenges, but the results of this work provide a good foundation for future studies, which should investigate the relationship between UVE measurements and current methods of assessing peripheral edema.

Table 4.1: Material properties of the individual tofu blocks (with 95% confidence intervals), as measured using mechanical creep tests

Tofu Block	E_0 (kPa)	E_1 (kPa)	τ (s)
A	12.7 (12.5, 12.8)	25.6 (24.9, 26.2)	79.5 (74.2, 85.0)
B	13.2 (13.1, 13.4)	28.3 (27.6, 29.0)	92.9 (85.7, 100.)
C	10.7 (10.6, 10.9)	17.8 (17.4, 18.1)	81.1 (77.0, 85.0)

Table 4.2: Material properties of the individual tofu blocks, median values as measured using UVE

Tofu Block	E_0 (kPa)	E_1 (kPa)	τ (s)
A	15.5	28.0	18.7
B	21.6	42.5	8.70
C	12.3	18.9	30.3

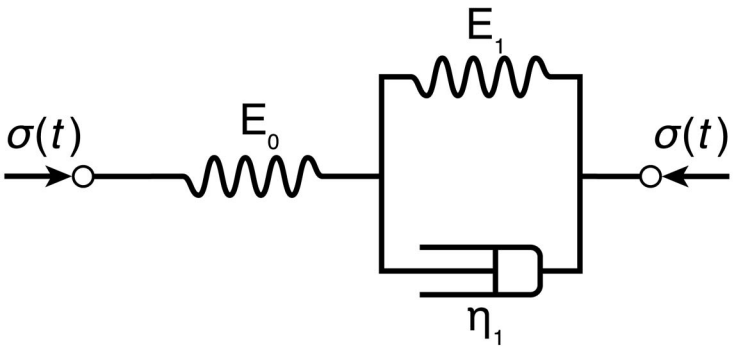

Figure 4.1: Spring-dashpot representation of the standard linear solid (SLS) viscoelastic model used to describe both the ultrasound viscoelastography and standard creep measurements.

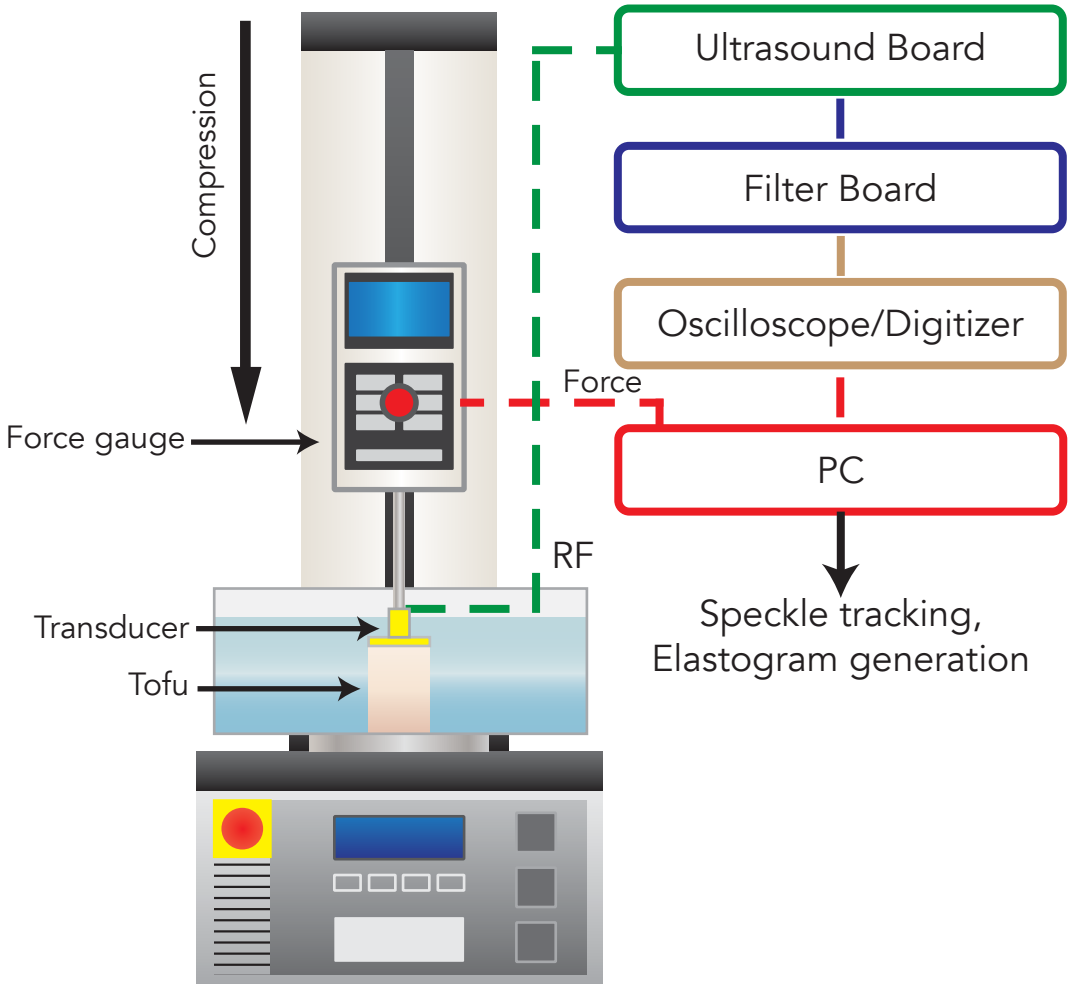

Figure 4.2: Schematic of ultrasound viscoelastography system depicting the mechanical test stand, single-element ultrasound transducer and tofu sample under test, as well as block diagrams for the electronics and acquisition hardware. Note that the mechanical test stand could be replaced with a portable or hand-held pressure source in the clinic. RF=radiofrequency.

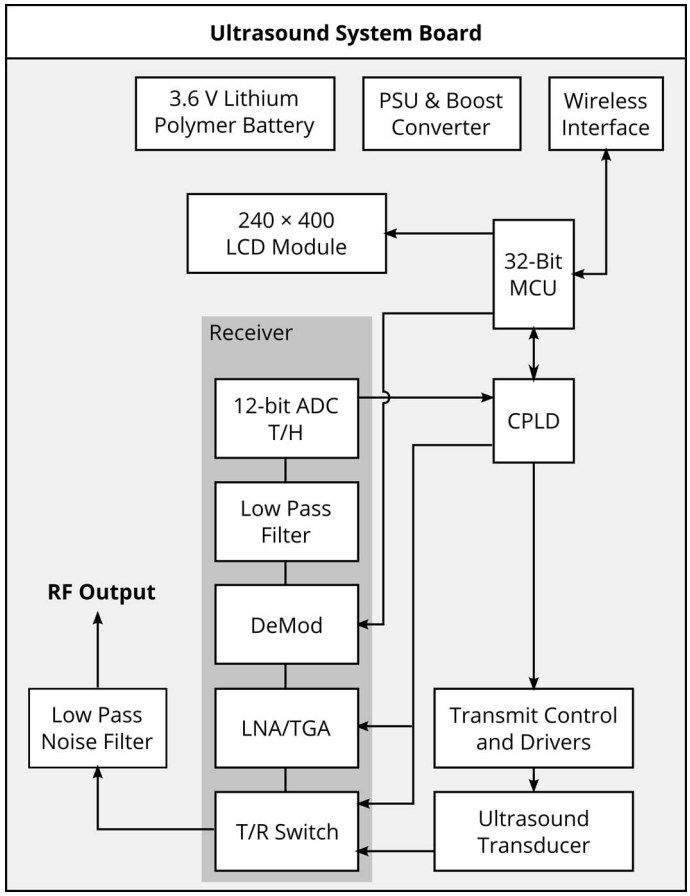

Figure 4.3: Block diagram of the portable ultrasound board used in our ultrasound viscoelastography experiments. ADC T/H = analogue-to-digital converter with track and hold function; CPLD = complex programmable logic device; DeMod = demodulator; LNA = low noise amplifier; MCU = microcontroller unit; PSU = power supply unit; RF = radiofrequency; TGA = time-gain amplifier; T/R = transmit/receive; serial peripheral interface bus.

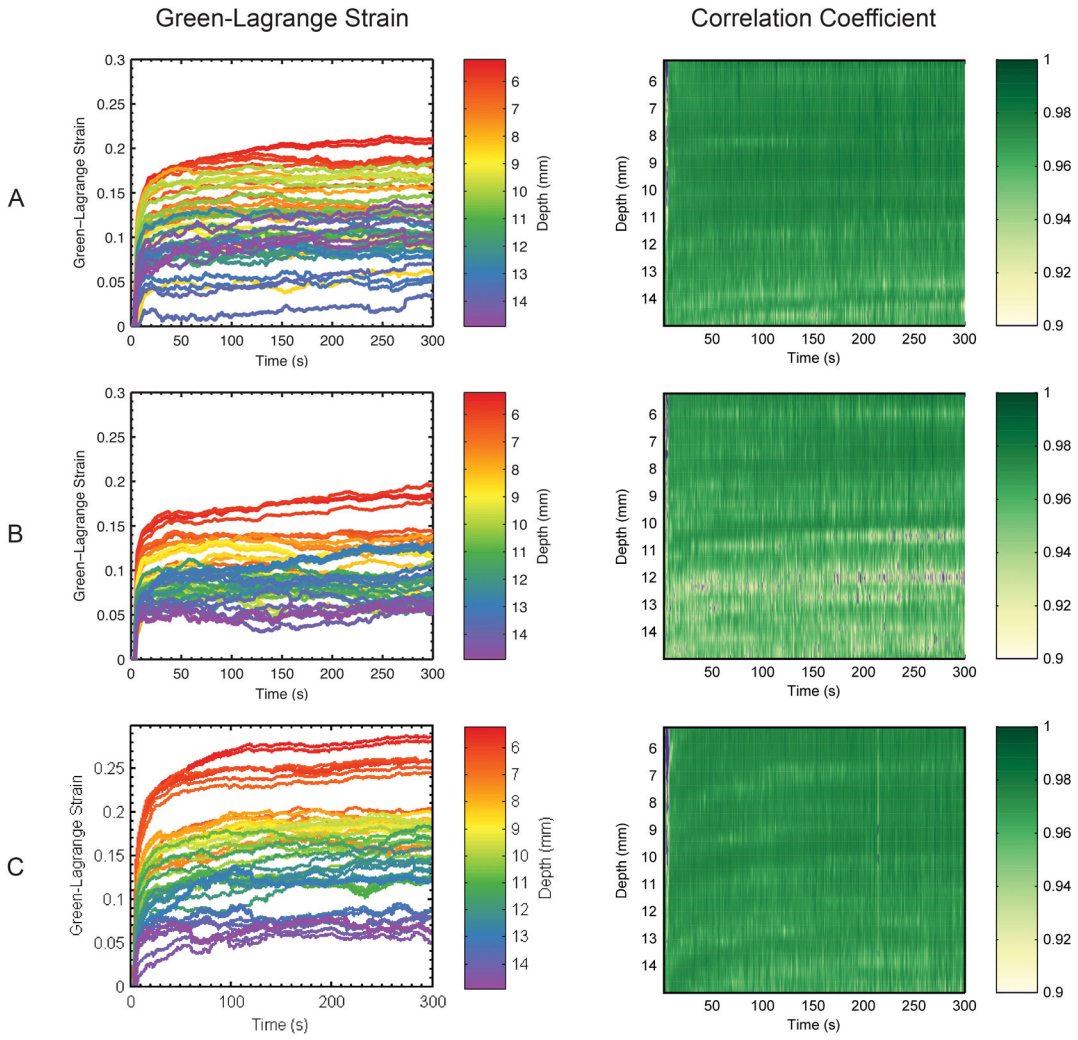

Figure 4.4: Ensemble Green–Lagrange strain creep curves and minimum correlation images obtained from samples in three blocks (A-C) of extra firm tofu. Ensemble strain creep curves are computed from an ensemble mean of measured displacement fields (n = 5, 6, and 6 for blocks A-C, respectively). These indicate a clear depth dependence in the mechanical response of the tofu samples. The minimum correlation images (rendered in an m-mode configuration) illustrate the pointwise minima of all computed correlation coefficients in each ensemble. In all cases (A-C), we found high correlation, with slightly less quality in tofu block B.

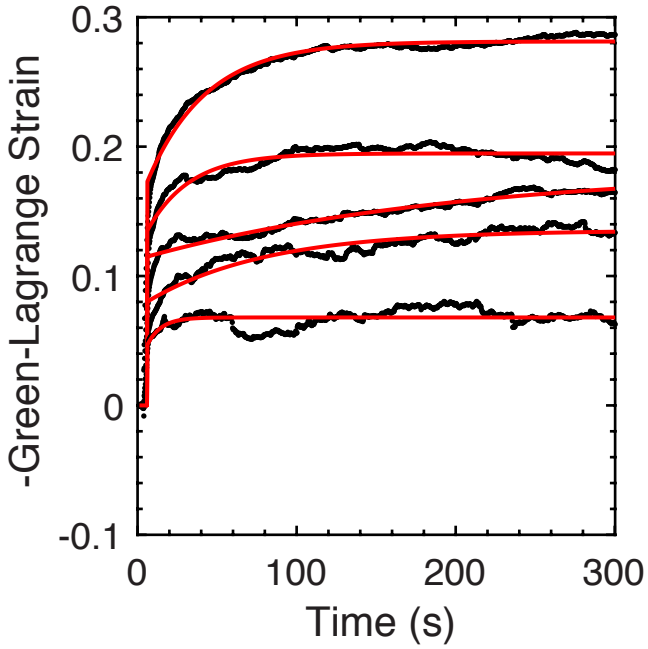

Figure 4.5: Example ultrasound viscoelastography creep curves at depths of 5, 7.5, 10, 12.5 and 15 mm from tofu block C, as well as curve fits using the SLS model of viscoelasticity. These curve fits were used to estimate the viscoelastic properties of the tofu samples at all depths.

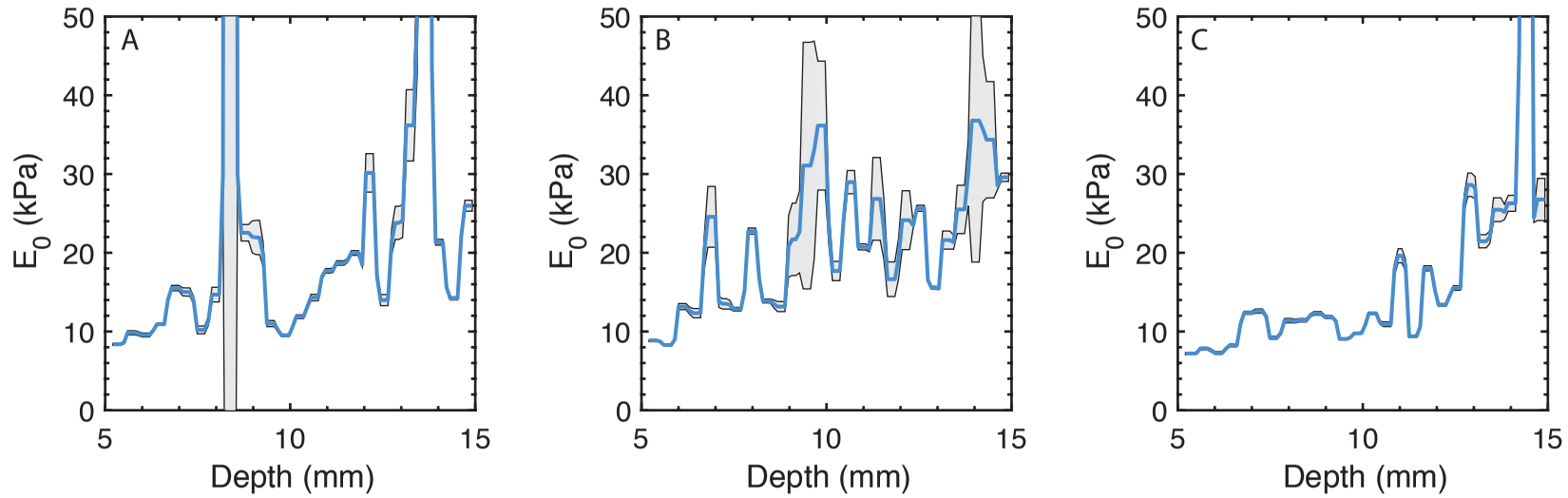

Figure 4.6: Viscoelastic instantaneous elastic modulus estimates (E_0) obtained by fitting the SLS viscoelastic model to the Green–Lagrange strain creep curves at all depths in tofu blocks (A-C). A slight upward trend is observed in the estimated value of E_0 (solid curves, 95% confindence interval shaded) through the entire depth of the tofu, with median values of 15.5, 21.6, and 12.3 kPa, respectively.

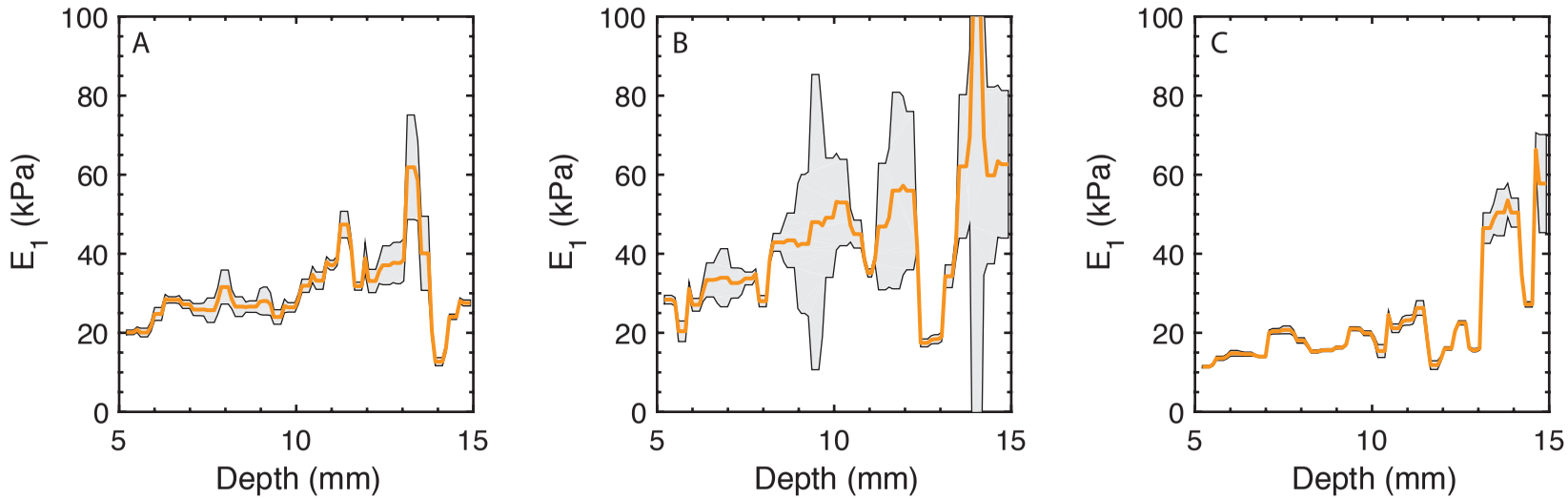

Figure 4.7: Viscoelastic secondary elastic modulus estimates (E_1) obtained by fitting the SLS viscoelastic model to the Green–Lagrange strain creep curves at all depths in tofu blocks (A-C). A slight upward trend is observed in the estimated value of E_1 (solid curves, 95% confindence interval shaded) through the entire depth of the tofu, with median values of 28.0, 42.5, and 18.9 kPa, respectively.

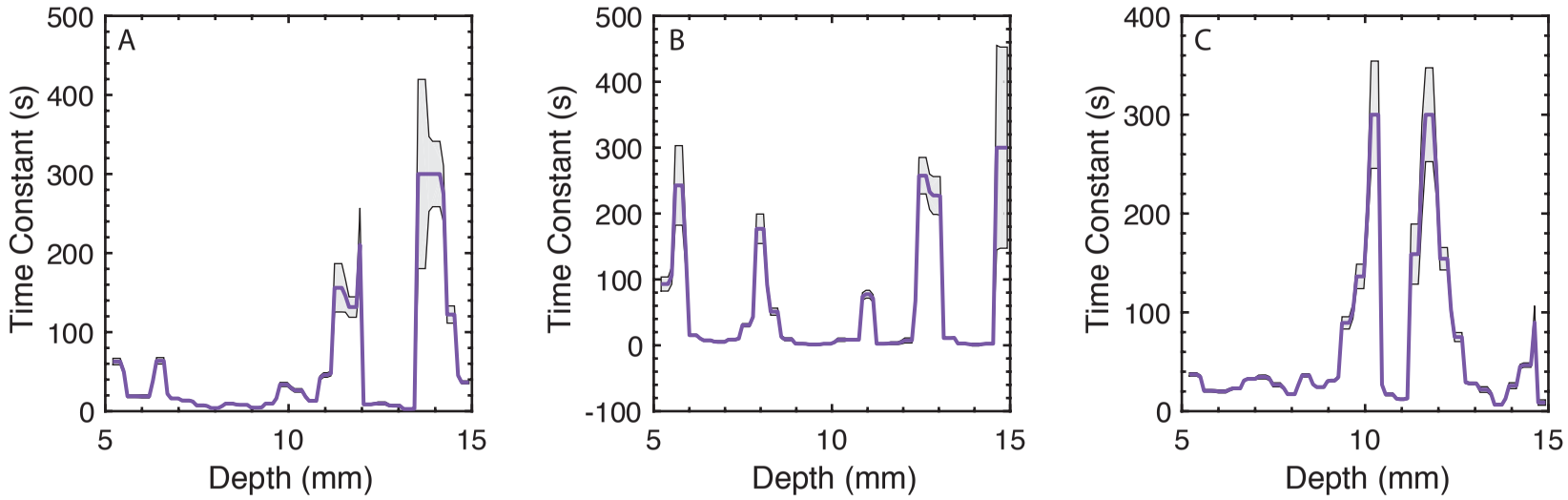

Figure 4.8: Viscoelastic time constants (τ) obtained by fitting the SLS viscoelastic model to the Green–Lagrange strain creep curves at all depths in tofu blocks (A-C). Large variations are observed in the estimated value of τ (solid curves, 95% confindence interval shaded), with median values of 18.7, 8.7, and 30.3 s, respectively.

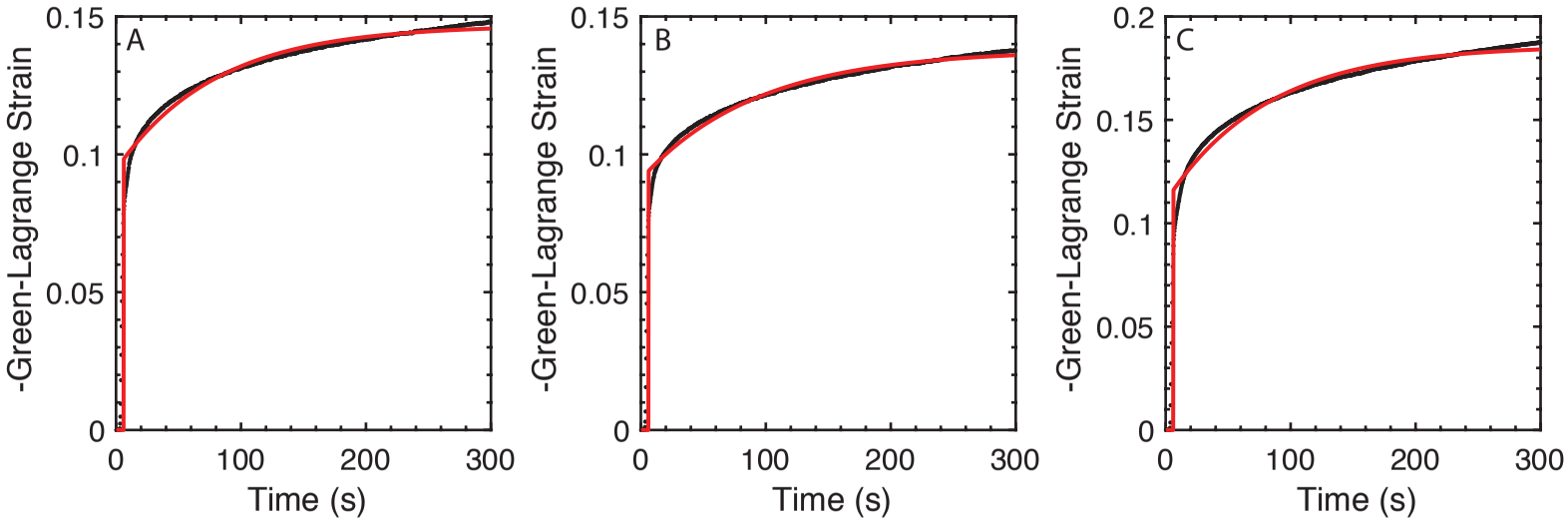

Figure 4.9: Mean creep curves from the standard creep compression test (black lines) and curve fits (red lines) for tofu blocks (A-C).

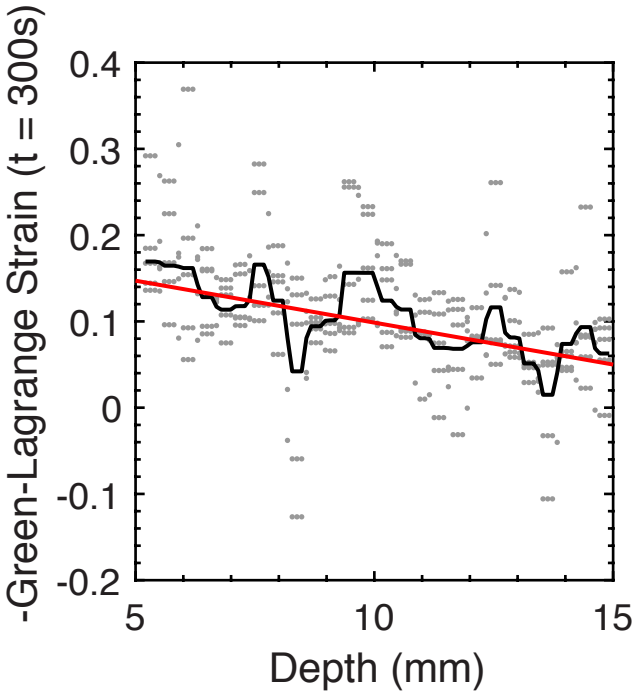

Figure 4.10: Comparison of the steady-state strained measured using UVE (gray dots = individual strain measurements; black line = mean strain) with a similar finite element model (red line) assuming a no-slip boundary along the top compressor. The strain shows a clear depth dependence. The finite element model suggests that it is possible that this dependence may be a result of the loading state rather than the material properties.

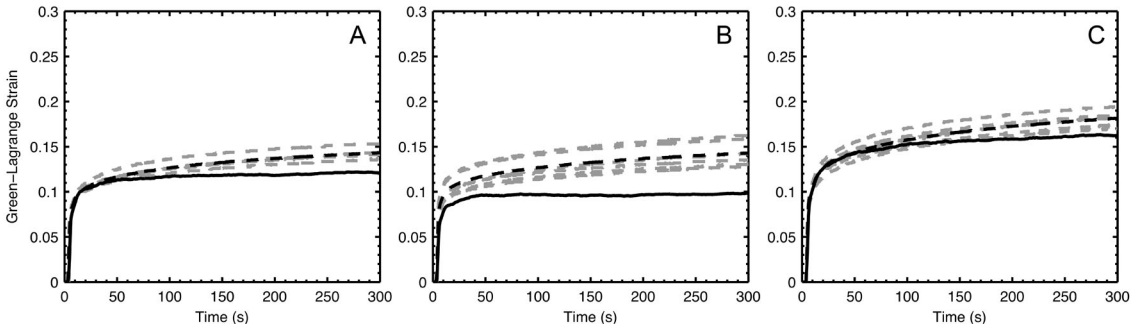

Figure 4.11: Comparison of mean creep curves from the mechanical displacement measurements (black dashed curves) with those obtained by averaging the strain measured using ultrasound viscoelastography over the depth of the sample (black solid curves) for tofu blocks (A–C). The individual realizations (n=6) of the mechanical creep measurements for each tofu block are shown as well (gray dashed curves).

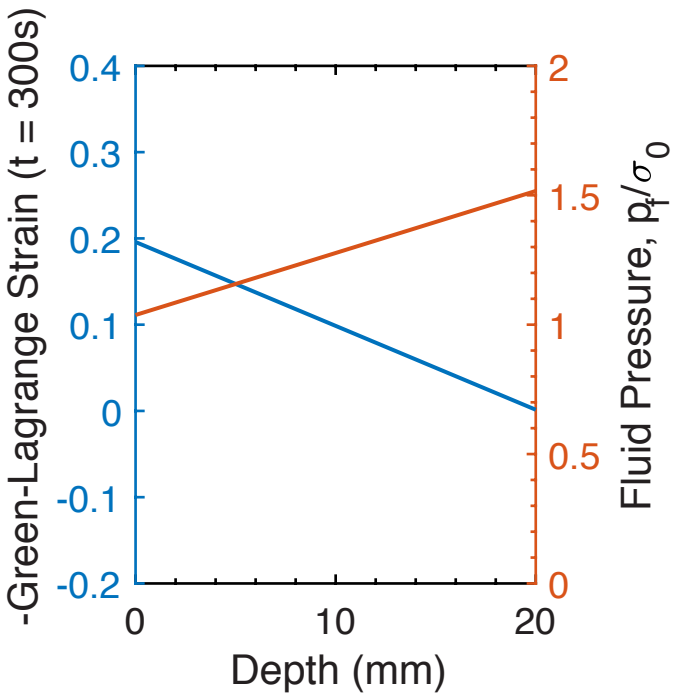

Figure 4.12: Comparison of the steady-state strained predicted by the finite element model (blue line) assuming a no-slip boundary along the top compressor and the fluid pressure field, normalized by the applied stress (orange line). The strain decreases at deeper depths while the pressure increases, potentially providing additional support for the solid matrix.

BIBLIOGRAPHY

Adriaenssens, N., Belsack, D., Buyl, R., Ruggiero, L., Breucq, C., De Mey, J., Lievens, P., and Lamote, J. (2012). Ultrasound elastography as an objective diagnostic measurement tool for lymphoedema of the treated breast in breast cancer patients following breast conserving surgery and radiotherapy. *Radiol. Oncol.*, 46(4):284–95.

Ammann, J., Rivera, R., and Ophir, J. (2005). Viscoelastic characterization of soft materials through creep test experiments. In *Fourth Int. Conf. Ultrason. Meas. Imaging Tissue Elast.*, page 54.

Armstrong, C. G., Lai, W. M., and Mow, V. C. (1984). An analysis of the unconfined compression of articular cartilage. *J. Biomech. Eng.*, 106(2):165–73.

Berry, G. P., Bamber, J. C., Mortimer, P. S., Bush, N. L., Miller, N. R., and Barbone, P. E. (2008). The spatio-temporal strain response of oedematous and nonoedematous tissue to sustained compression in vivo. *Ultrasound Med. Biol.*, 34(4):617–29.

Fung, Y. (1993). *Biomechanics: Mechanical Properties of Living Tissues*. Springer New York, New York, NY, 2nd edition.

Insana, M. F., Pellot-Barakat, C., Sridhar, M., and Lindfors, K. K. (2004). Viscoelastic imaging of breast tumor microenvironment with ultrasound. *J. Mammary Gland Biol. Neoplasia*, 9(4):393–404.

Kouw, P. M., Kooman, J. P., Cheriex, E. C., Olthof, C. G., de Vries, P. M., and Leunissen, K. M. (1993). Assessment of postdialysis dry weight: a comparison of techniques. *J. Am. Soc. Nephrol.*, 4(1):98–104.

Kruger, G. H., Dodde, R. E., Koziol, L. B., and Weitzel, W. F. (2012). Novel method and device for viscoelastic tissue characterization of edema. In *IEEE Int. Ultrason. Symp. IUS*, pages 2368–2371.

Kuei, S., Lai, W., and Mow, V. (1978). A biphasic rheological model of articular cartilage. In Eberhardt, R. and Burstein, A., editors, *Adv. Bioeng.*, page 17. American Society of Mechanical Engineers.

Lindop, J. E., Treece, G. M., Gee, A. H., and Prager, R. W. (2008). Dynamic Resolution Selection in Ultrasonic Strain Imaging. *Ultrasound Med. Biol.*, 34:809–823.

Mow, V. and Kuei, S. (1980). Biphasic creep and stress relaxation of articular cartilage in compression: theory and experiments. *J. . . .*, 102(February 1980):73–84.

Oe, B., de Fijter, C. W., Geers, T. B., Vos, P. F., Donker, A. J., and de Vries, P. M. (2000). Diameter of inferior caval vein and impedance analysis for assessment of hydration status in peritoneal dialysis. *Artif. Organs*, 24(7):575–7.

Pitre, Jr, J. J., Koziol, L., Kruger, G. H., Vollmer, A., Ophir, J., Ammann, J., Weitzel, W. F., and Bull, J. L. (2016). Design and testing of a single-element ultrasound viscoelastography system for point-of-care edema quantification. *Ultrasound Med. Biol.*, 42(9):2209–2219.

Qiu, Y., Sridhar, M., Tsou, J. K., Lindfors, K. K., and Insana, M. F. (2008). Ultrasonic viscoelasticity imaging of nonpalpable breast tumors: preliminary results. *Acad. Radiol.*, 15(12):1526–33.

Righetti, R., Garra, B. S., Mobbs, L. M., Kraemer-Chant, C. M., Ophir, J., and Krouskop, T. A. (2007). The feasibility of using poroelastographic techniques for distinguishing between normal and lymphedematous tissues in vivo. *Phys. Med. Biol.*, 52(21):6525–41.

Sridhar, M., Liu, J., and Insana, M. F. (2007). Viscoelasticity imaging using ultrasound: parameters and error analysis. *Phys. Med. Biol.*, 52(9):2425–43.

Treece, G., Lindop, J., Chen, L., Housden, J., Prager, R., and Gee, A. (2011). Real-time quasi-static ultrasound elastography. *Interface Focus*, 1(4):540–552.

Westerweel, J. and Scarano, F. (2005). Universal outlier detection for PIV data. *Exp. Fluids*, 39:1096–1100.

Yashiro, M., Kamata, T., Yamadori, N., Tomita, M., and Muso, E. (2007). Evaluation of markers to estimate volume status in hemodialysis patients: atrial natriuretic peptide, inferior vena cava diameter, blood volume changes and filtration coefficients of microvasculature. *Ther. Apher. Dial.*, 11(2):131–7.

CHAPTER 5

The effects of geometry and strain magnitude on poroelastography curve fitting

5.1 Introduction

In the previous chapter, I demonstrated a method for estimating the material parameters of a tissue-mimicking material using ultrasound viscoelastography. These ultrasound measurements were taken at large strain magnitudes, on the order of 10%, with a motorized test stand applying a constant compressive force to the cylindrical tofu samples. Using the standard linear solid (SLS) constitutive model, I obtained elastic moduli and time constants to characterize the tofu.

While this study detailed a potentially useful method for obtaining viscoelastic coefficients of edematous tissue, it also faced a number of limitations that could hinder its clinical application. The viscoelastic coefficients obtained from the SLS model are primarily descriptive in nature. They are based on a spring-dashpot representation rather than a continuum model, and their interpretation is not as straightforward as the physical parameters normally associated with continuum mechanics, such as Young's modulus and Poisson's ratio. Poroelastography offers one avenue for circumventing this difficulty by providing a continuum model that exhibits similar creep behavior. Ultimately however, clinical usefulness is the most important measure of a method's promise. The difficulty of interpreting parame-

ters does not necessarily preclude this method from finding uses, and only future clinical studies can assess this.

More fundamentally, the previous study faced limitations also common to many poroelastography studies. These limitations stem from the assumptions inherent in the constitutive model, the loading configuration, and the test sample geometry, and they are not as easily surmounted. Because it is zero-dimensional, the SLS model in some sense assumes spatial uniformity, uniaxial loading, and stress uniformity. In a similar way, most poroelastography studies fundamentally rely on Armstrong's solution to the KLM biphasic model (Armstrong et al., 1984). This solution, as detailed in Chapter 3, assumes a cylindrical geometry, axisymmetry, uniaxial loading, small strain, uniform axial strain, and no dependence on the axial coordinate. In the first paper describing poroelastography, Konofagou et al. (2001) used Armstrong's solution to argue that the lateral-to-axial strain ratio, or the effective Poisson's ratio (EPR), approaches the Poisson's radius of the drained porous matrix as the behavior approaches steady state. Multiple studies have expanded on this assumption and have relied on Armstrong's solution to estimate the Young's modulus, Poisson's ratio, and permeability of poroelastic phantoms via curve fitting (Righetti et al., 2004, 2005b; Berry et al., 2006a,b; Galaz and Acevedo, 2017). These benchtop experimental studies satisfy all the assumptions of Armstrong's solution, and so their findings are entirely in line with biphasic theory.

The restrictive assumptions of Armstrong's solution may hinder clinical applicability of poroelastography methods that rely on curve fitting. It is infeasible to obtain cylindrical samples of tissue for external laboratory testing in most cases. While tumor biopsies represent one more reasonable example, this approach would border on the absurd for the commonly proposed application of edema quantification. Clinical studies must instead rely on in-vivo measurements of a

large region of tissue, for example the arms or legs (Righetti et al., 2007b; Berry et al., 2008). In these cases, most of the assumptions of Armstrong's solution are no longer valid. The tissue is not a cylinder, the imaged region may not be spatially uniform, and boundary conditions at tissue borders may not match the simple slip conditions required.

Another aspect of Armstrong's solution that may potentially hinder clinical applications is its requirement of small strains. Small strains are known to increase the elastographic signal to noise ratio (SNRe), which decreases rapidly above 10% strain where signal decorrelation becomes problematic (Varghese and Ophir, 1997). Small strains are easy to enforce in the laboratory using motorized compression devices, but these devices may limit imaging locations or take too much time to configure in the clinic. Free hand elastography may therefore be more desireable in clinical settings (Hall, 2003b). Free hand elastography studies tend to differ in their approach of applying strain. Many apply strains on the order of 1-2% (Doyley et al., 2001; Zhu and Hall, 2002; Treece et al., 2008; Qiu et al., 2008), but others tend to prefer applying larger strains ranging from 5-20% (Zhu and Hall, 2002; Hall, 2003a; Righetti et al., 2007a; Berry et al., 2008; Goenezen et al., 2012). Large strain studies must make use of more complicated processing methods such as summing incremental strains (Hall, 2003a), multicompression averaging (Varghese et al., 1996), and moving reference frames (Righetti et al., 2005a). These adjustments to the strain estimation procedure circumvent the large strain limitations of the SNRe. Large strains offer the additional advantage that it is simply easier to accurately and reproducibly apply a large strain to soft tissue. Furthermore, for poroelastography applications, large strains more closely mirror the physical examination for edema.

The extent to which model assumptions of geometry and strain magnitude play a role in affecting poroelastic measurements has not been investigated previously.

In this chapter, I analyze these effects using a finite element model of poroelastic deformation of a rectangular block compressed only in a small region at its center. This is meant to mirror the case of a clincian applying compression using an ultrasound transducer. This has important implications both for the expected axial strain measurements and the observed EPR. I also show the limitations of the Armstrong solution at large strain using a finite element model of a poroelastic cylinder under creep compression. The importance of these results is then demonstrated using ultrasound measurements of tofu under compression, mimicking both of the cases described by the finite element models.

5.2 Methods and Materials

5.2.1 Poroelastic Block Model

To analyze the importance of geometry on poroelastography curve fitting methods, I developed a finite element model of the deformation of a rectangular block of poroelastic material using Comsol Multiphysics (Comsol, Burlington, MA). Deformation was governed by Biot's poroelastic model (Biot, 1941):

$$\frac{E}{1+\nu}\varepsilon_{ij} + \frac{\nu}{(1+\nu)(1-2\nu)}\epsilon_{,i} - \alpha p_{,i} = 0 \tag{5.1}$$

$$\frac{1}{M}\frac{\partial p}{\partial t} - \frac{\kappa}{\mu}p_{,ii} = -\alpha\frac{\partial \epsilon}{\partial t} \tag{5.2}$$

$$\frac{1}{M} = \phi\chi_f + (\alpha - \phi)\frac{1-\alpha}{K}, \tag{5.3}$$

where E, K, ν, and κ are the Young's modulus, bulk modulus, Poisson's ratio, and permeability of the drained porous matrix, respectively, ε is the strain tensor, ϵ is the volumetric strain, p is the pore fluid pressure, α is the Biot-Willis coefficient, χ_f is the fluid compressibility, μ_f is the fluid viscosity, and ϕ is the matrix porosity.

The values for these parameters used in the model are given in Table 5.1. Of note, the Biot-Willis coefficient α was set to 1, corresponding to a case where the solid and fluid constituents are both incompressible. This assumption is reasonable for biological tissue, and also matches the formulation of the KLM biphasic model. Additionally, the porosity ϕ was arbitrarily set to 0.3. Since porosity only factors into the definition of the Biot modulus $1/M$ where it is multiplied by the fluid compressibility $\chi_f = 0$ and the term $1 - \alpha = 0$, the chosen value will have no effect on the material behavior.

The height of the poroelastic block was defined as 40 mm. A compressive load was applied to the top surface of the block inside a rectangular region 26 mm wide by 17 mm deep (A_{load}). The total width and depth of the block were defined by an area ratio $\hat{A} = A/A_{load}$, where A = width $\times$ depth. I tested area ratios of 2, 5, 10, and 25. The block geometries including the load area for each area ratio are shown in Figure 5.1.

The model's boundary conditions are shown in Figure 5.2. The bottom surface was assigned a roller condition, and two of the bottom edges were constrained to move only along their respective axes. All other faces were allowed to deform freely. Along the side faces, the fluid pressure was set to atmospheric pressure, $p = 0$. The top face outside the loading area was set either to an atmospheric pressure condition or a no flow condition. The loading area and bottom surface were also set to no flow conditions. The boundary load inforced on the loading area was a constant force condition with the force $F_0 = E\varepsilon_{nom}A_{load}$, for some nominal strain ε_{nom}. For small strain tests, $\varepsilon_{nom} = 0.02$, while for large strain, $\varepsilon_{nom} = 0.20$. It is important to note that at large strains, this is not equivalent to a constant stress condition since the loading area may change with time as the material deforms.

The domain was discretized using a free tetrahedral mesh and quadratic elements for both the displacements and pressures. An implicit backwards differen-

tiation formula (BDF) method was used for time stepping with the solver free to choose the size of the time step (SUNDIALS, Lawrence Livermore National Labs, (Hindmarsh et al., 2005)). The equations were solved either to t = 240 s to mirror the experiments detailed later in this chapter or to t = 960 s to reach steady state. The engineering strain was obtain from the model by dividing the maximum displacement within the loading area w_{max} by the original height of the block h = 0.04 m.

5.2.2 Poroelastic Cylinder Model

To analyze the effect of strain magnitude on curve fitting poroelastography measurements, I developed a second finite element model, this time of the unconfined compression of a cylinder, using Comsol. This model mirrors the one used by Konofagou et al. (2001) and Berry et al. (2006a) with the exception of the loading conditions. In those studies, the authors enforced stress-relaxation conditions – a constant axial displacement of the top surface. This configuration has some advantages in ease of experimental implementation, but would likely face clinical challenges since the internal strain in the tissue is a goal of the poroelastic measurement rather than an enforceable condition. Furthermore, the stress-relaxation solution developed by Armstrong (Equation 5.4) does not allow the permeability k to be independently determined from the other poroelastic constants, as noted by Berry et al. (2006a). In contrast, Armstrong's solution for creep loading (Equation 5.5) allows for E, ν, and k to all be determined uniquely from curve fitting.

$$\frac{u}{a}(a,t) = \epsilon_0 \left[\nu + (1-2\nu)(1-\nu) \sum_{n=1}^{\infty} \frac{\exp\left(-\alpha_n^2 \frac{H_a k t}{a^2}\right)}{\alpha_n^2 (1-\nu)^2 - (1-2\nu)} \right] \tag{5.4}$$

$$\varepsilon(t) = -\frac{F_0}{E\pi a^2}\left[1-(1-\nu^2)(1-2\nu)\right. \\ \left.\sum_{n=1}^{\infty}\frac{4}{9(1-\nu^2)\beta_n^2-8(1+\nu)(1-2\nu)}\exp\left(-\beta_n^2\frac{H_a k t}{a^2}\right)\right] \tag{5.5}$$

$$H_a = \frac{E(1-\nu)}{(1+\nu)(1-2\nu)}. \tag{5.6}$$

The cylindrical domain was defined with height h = 40 mm and radius a = 17.5 mm to mirror benchtop experiments. All material properties were kept the same as the poroelastic block model (Table 5.1). The domain was discretized using a regular grid with 400 elements in the radial direction and 1 element in the axial direction, identical to the grid used by Berry et al. (2006a). The axisymmetric form of equations 5.1, 5.2, and 5.3 was solved using quadratic elements for both the displacements and pressures, using the same time stepping scheme described in the previous section. As before, the engineering strain was obtain from the model by dividing the maximum displacement w_{max} by the original height.

Boundary conditions for the cylinder finite element model are shown in Figure 5.3. These are nearly identical to those required by Armstrong's solution, with the subtle exception of the boundary load. The boundary load was enforced as a constant force condition, $F_0 = E\varepsilon_{nom}\pi a^2$, for some nominal strain ε_{nom}. For small strain tests, $\varepsilon_{nom} = 0.02$, while for large strain, $\varepsilon_{nom} = 0.20$. Again, this constant force condition is only equivalent to the constant stress condition imposed by Armstrong at infinitesimal strain. The top and bottom surfaces were both set as roller conditions (implying that vertical displacements were uniform on the top face, and vertical displacements were zero along the bottom face). The outer surface of the cylinder was allowed to deform freely, and the fluid pressure was set to atmospheric, $p = 0$.

5.2.3 Biphasic Cylinder Model

As a comparison for the block and cylinder models, I implemented Armstrong's solution for a biphasic cylinder of radius a under constant stress loading (creep conditions). Equation 5.5 was solved in MATLAB (The Mathworks, Natick, MA) to obtain the strain history in the material under compression. To find the roots β_n of the characteristic equation, a coarse zero crossing routine was first used to bracket the locations of the zeros. Next, a combination of bisection and interpolation methods were used to find a finer estimate of the bracketed zero (fzero, MATLAB, The Mathworks, Natick, MA).

5.2.4 Experiments - Tofu Cylinders

The objective of these experiments was to demonstrate the implications of the theoretical assumptions associated with each of the above models. To do this, I first performed creep compression experiments on cylinders of tofu. The properties of tofu as a tissue-mimicking ultrasound phantom are well documented (Wu, 2001; Kim et al., 2009), and tofu has become the de facto choice of phantom in poroelastography studies (Righetti et al., 2004, 2005a; Berry et al., 2006b; Righetti et al., 2007b; Perriñez et al., 2010b,a; Nair et al., 2011; Nair and Righetti, 2015). Cylinders of extra firm tofu (House Foods America, Golden Grove, CA) were cut to dimensions of 40 mm tall and 35 mm in diameter (n = 65). These were placed atop an electronic scale, and ultrasound coupling gel was applied to the top surface of the cylinders. The scale was then zeroed.

Compression was applied by placing a cylindrical compressor holding a 3.3 MHz phased array ultrasound transducer (SA4-2, BK Ultrasound, Peabody, MA) onto the sample (Figure 5.4). The compressor consisted of a cylindrical plastic enclosure with a window cut in the bottom for the ultrasound transducer face. The

transducer was placed inside this enclosure with its face completing the bottom of the contact surface of the compressor. Modeling clay was then packed around the transducer to hold it securely in place and add weight to the compressor. The total mass of this assembly was 220 g. When placed on the tofu samples, the compressor was stabilized by hand, but its weight was allowed to freely deform the tofu. Observations of the scale showed that the force could be held relatively constant within a range of +/- 2 N. The radius of the tofu cylinders together with the applied force imply a nominal applied stress of 2.2 kPa. Compression was maintained for 4 minutes while ultrasound RF data were acquired by a SonixRP ultrasound scanner (Ultrasonix, BK Ultrasound, Peabody, MA) at a frame rate of 30 Hz. The imaging depth was set to 5 cm, and the scan sector to 50% (45 degree sector). The frame buffer could not store all 4 minutes of images, so RF data sets were saved in intervals of 90, 90, and 60 seconds.

The time series of ultrasound data were processed offline using two methods. Each method produced an estimate of the axial strain history in the sample. I will refer to the first method as boundary tracking. For these measurements, the RF frames were converted into brightness (B-mode) images using the envelope of the RF data and logarithmic compression. The sector line data were resampled on a 512×512 pixel regular grid. To identify a reference frame, the pixel brightnesses were summed in each image, and the reference frame chosen by the sudden jump in brightness created when the transducer properly coupled to the sample (Figure 5.5). For each image, the lower boundary of the tofu was identified manually, and a 31×31 pixel window created containing the boundary. This window was tracked vertically with respect to the initial reference frame for every tenth frame in the data set using normalized cross correlation. The strain was then estimated as the tracked displacement in pixels divided by the pixel index of the boundary.

The second method tracked motion using the RF data directly. In this method

a moving reference frame was used to ensure that each interframe strain was approximately 2% (Righetti et al., 2005a). Motion was tracked along the radial direction of each scan line (corresponding to different angular coordinates) using normalized cross correlation with a 1 cm axial kernel window with a 75% overlap. Temporal stretching was not applied to the RF windows because the compression was not perfecly parallel to the scan lines. These radial displacements were then converted to cartesian displacement components. The displacement estimates corresponding to the five central scan lines were then extracted. These scan lines were the only ones that spanned the full depth of the image (due to the sector to cartesian conversion). Furthermore, these lines represented the closest set of measurements for which the scan line was nearly parallel to the compression direction. An axial region of interest was then created using the boundary tracking method to crop measurements that were beyond the lower boundary of the tofu cylinder. The incremental strain for each frame pair was then estimated using the slope of a linear fit over the axial displacement measurements in the region of interest. These incremental strains were then summed, ensuring that the correct series of increments were summed from the first frame to any given interrogation frame.

5.2.5 Experiments - Tofu Blocks

As a point of comparison for the poroelastic block model, I also performed experiments using rectangular blocks of tofu. Blocks of extra firm tofu (House Foods America, Golden Grove, CA) were cut to dimensions of 122 mm $\times$ 94 mm (n = 9). As in the previous experiments, the tofu blocks were placed on an electronic scale and ultrasound coupling gel was applied to the middle of the block. Using the 3.3 MHz phased array ultrasound transducer (SA4-2, BK Ultrasound, Peabody, MA), I applied a freehand compression of 1 N, using the measurement on the scale for feedback (Figure 5.6). The face of the transducer had an area of 26 mm $\times$ 17

mm yielding an applied stress of approximately 2.2 kPa. Note that this is the same as the nominal stress applied in the cylinder experiments. The compression was again sustained for 4 minutes, and data were acquired using the same ultrasound settings and processed using the same strain estimation techniques as the previously described cylinder experiments.

5.2.6 Curve Fitting Parameter Estimation

The mean strain creep curves obtained in all experiments were fit using a nonlinear least squares procedure to obtain estimates of E, ν, and k. For the tofu cylinder data, fits were performed using both the Armstrong solution and the finite element poroelastic cylinder model to solve the forward problem. For the tofu block data, the finite element poroelastic block model was used in addition to the two cylinder models. This corresponds to the potential misuse of the cylindrical geometry assumption in estimating poroelastic parameters. The fit parameters were initialized as $E = 16$ kPa, $\nu = 0.0$, and $k = 1 \times 10^{-10}$ m^{4}N^{-1}s^{-1}. The Young's modulus and permeability were bounded below by zero, but unbounded above. Poisson's ratio was bounded to the range [-0.49, 0.49] to ensure that the forward problem remained non-singular. Previous poroelastography studies have not observed negative values of Poisson's ratio for tofu (Righetti et al., 2004, 2005b,a, 2007b; Berry et al., 2006b), and so additional fits were performed with the Poisson's ratio constrained to only positive values. Because the fitting parameters spanned several orders of magnitude (ranging from approximately 10^{-11} to 10^4), scaling was introduced to improve the performance of the least squares solver:

$$\begin{bmatrix} E \\ \nu \\ k \end{bmatrix} = \begin{bmatrix} p_1 \times 10^4 \\ p_2 \times 10^{-1} \\ p_3 \times 10^{-11} \end{bmatrix}. \tag{5.7}$$

5.3 Results

5.3.1 Finite Element Models

Figure 5.7 shows the predicted engineering strain at time t = 240 s for the poroelastic cylinder finite element model at both small and large strain for various meshes. Figures 5.8 and 5.9 show the same metric for various meshes for the poroelastic block finite element at different area ratios $\hat{A} = 2$, 5, 10, and 25 at small and large strains, respectively. These show that the solutions are independent of the chosen mesh element size.

Figure 5.10 compares the engineering strain history at small strain for Armstrong's creep solution, the poroelastic cylinder finite element model, and the poroelastic block finite element model for various area ratios $\hat{A}$. The finite element model of the cylinder closely resembles the analytical solution, diverging from it only slightly as the time increases. All of the creep curves obtained from the block model show substantially lower strains that decrease as the area ratio increases and tend to converge toward each other with increasing $\hat{A}$.

Figure 5.11 presents the same comparison of the engineering strain history at large strain. In this case, Armstrong's analytic creep solution differs greatly from the finite element cylinder model with the difference becoming much more pronounced as time increases. As before, the poroelastic block model exhibits decreasing strain as $\hat{A}$ increases, and the creep curves tend to converge for larger values of $\hat{A}$.

Figure 5.12 shows the evolution of the effective Poisson's ratio in the poroelastic block model for $\hat{A} = 25$. This area ratio most closely approximates the size of the tofu blocks used in my experiments. The EPR, defined here by $EPR = -\varepsilon_{xx}/\varepsilon_{zz}$, is shown at various depths below the loading area with coordinates $(x, y, z) = (0, 0, z)$. Figure 5.12b shows the evolution when a no flow boundary condition is

enforced on the top surface of the block, mirroring conditions likely to be seen in a clinical measurement. Figure 5.12c shows the evolution when an atmospheric pressure condition is enforced, mirroring the benchtop tofu block experiments. At time t = 0, the EPR exhibits its maximum value, typically in the range of 0.3-0.5. As time progresses, the EPR decays until it approaches a steady state value. The steady state EPR varies with depth and differs slightly between the two boundary conditions investigated (Figure 5.13). Greater differences are observed near the bottom of the block.

5.3.2 Ultrasound Measurements and Parameter Estimates

Figure 5.14 shows the mean creep curves (n = 65) generated by ultrasound measurements of tofu cylinders under compression as well as curve fits obtained using Armstrong's solution and the finite element cylinder model. The two strain estimation methods produced very similar measurements. Allowing the Poisson's ratio estimate to be negative produced better fits than constraining it to be positive. While it is not the most rigorous quality of fit metric for nonlinear data, the coefficient of determination R^2 of the negative Poisson's ratio images was in all cases higher than the corresponding positive Poisson's ratio fit. Also of note, for positive Poisson's ratio fits, the R^2 of the fits obtained using the finite element model was greater than those obtained using Armstrong's solution.

Tables 5.2 and 5.3 show the parameter estimates for the negative and positive Poisson's ratio fits, respectively. In the former case, the Poisson's ratio tended to fall between -0.15 and -0.32, while in the latter, it consistently produced an estimate of 0.00. Differences in the Young's modulus estimates were rather independent of the Poisson's ratio constraint and instead differed primarily with respect to the strain estimation method and the curve fitting method, producing estimates between 12.2 and 18.0 kPa. Permeability estimates fell in the range of 1.01 $\times 10^{-10}$ to

2.60×10^{-10} $m^4N^{-1}s^{-1}$.

Figure 5.15 shows the mean creep curves (n = 9) generated by ultrasound measurements of tofu blocks under compression and the curve fits obtained from Armstrong's solution, the finite element cylinder model, and the finite element block model. In this set of measurements, the choice of strain estimation method greatly affected the generated creep curves. The block model produced the best fit, with R^2 increasing as one moves from the Armstrong solution to the finite element cylinder model to the block model for the positive Poisson's ratio constraint.

Tables 5.4 and 5.5 show the parameter estimates for the boundary tracking and RF tracking strain estimators. Here, the Poisson's ratio constraint primarily affected the estimates of ν and k. The Young's modulus depended primarily on the choice of model and different fits produced a range of values from 10 kPa to 50.9 kPa. The poroelastic block models produced estimates closest to those observed in the cylinder experiments.

5.4 Discussion

5.4.1 Finite Element Models

The finite element models described in this chapter highlight the importance of model assumptions on the expected strain history of a poroelastic material under creep compression. Past poroelastography studies have relied heavily on the assumptions of Armstrong's solution to the biphasic KLM model. These assumptions chiefly include cylindrical geometry and small strain. In clinical practice, however, these conditions may not always be appropriate. Even at small strain, large differences in the expected strain history are predicted as the geometry shifts from a cylinder to a wider slab (Figure 5.10). These differences become even more pronounced at large strains. This is a result of the subtle difference in how the

boundary load is defined. For a constant force loading, deformation of the compressed material leads to a change in the area to which compression is applied, assuming the compressor is larger than the cylinder being compressed. This implies that the applied stress actually decreases with time, despite the force remaining constant. This could pose problems for freehand poroelastography where large deformations may be preferable to small ones.

Even when using a deformation model that accounts for the change in configuration, the large variations observed between the cylinder models and the block model, especially for large values of $\hat{A}$ suggest that the choice of deformation model geometry may be very important in obtaining reliable poroelastic parameter estimates. Furthermore, the poroelastic block finite element model reveals that one of the fundamental assumptions of poroelastography – that the EPR decays to the Poisson's ratio at steady state – is itself subject to the same limitations of geometric assumptions. While it is a useful property of poroelastic cylinder deformation, it does not hold true for the block model and may not hold true in clinical measurements. Indeed, it could be argued that some of the clinical poroelastograms generated by Righetti et al. (2007b) exhibit a depth-dependent EPR (see Figures 2-5, 10-13 in that study). The authors seemed to have noted these features, but suggested that they were the result of spatial variations in the poroelastic properties that were not visible in the standard sonograms. While this interpretation may be reasonable, the models presented in the present study provide an alternate explanation that should be investigated with further benchtop and clinical experiments. Note that the Righetti et al. study enforced stress relaxation conditions rather than creep, and the differences between these loadings should be examined carefully in future studies.

5.4.2 Ultrasound Measurements and Parameter Estimates

The strain measurements obtained experimentally for cylinders of tofu at large strain closely resemble the classical creep response typically described for viscoelastic and poroelastic materials (Fung, 1993). Both Armstrong's biphasic solution and the finite element model developed in this study produce reasonably good fits to the experimental data, though they perform somewhat poorly for data within the first minute, particularly when the Poisson's ratio is constrained to positive values (Figure 5.14). There is some ambiguity to the correct choice in this matter. While not exactly common, materials with negative Poisson's ratio do exist (Greaves et al., 2011). However, such materials are typically synthetic metamaterials, and previous poroelastography studies that have quantified the Poisson's ratio of tofu using both mechanical tests and poroelastograms have placed its value between 0 and 0.3 (Righetti et al., 2004, 2005b,a, 2007b; Berry et al., 2006b). In light of this, the constraint $\nu \geq 0$ may be more reasonable despite the apparent lack of fit (Table 5.3). This study consistently estimated the Poisson's ratio to be equal to zero, which is consistent with measurements of tofu by Berry et al. (2006b). The Young's modulus estimates found in this study were on the order of 12.5-18.0 kPa. The permeability estimates were on the order of 1×10^{-10} $\mathrm{m^4N^{-1}s^{-1}}$. These estimates are large compared to the values reported in the aforementioned studies, roughly an order of magnitude higher in both cases. It is unclear if this corresponds to an actual difference in material properties or if the conditions of large strain lead to a different measured parameter.

Taking the coefficient of determination R^2 as a metric for the quality of fit, it is clear that the finite element cylinder model produces a better fit than Armstrong's solution (Table 5.3). While the R^2 is not strictly valid for nonlinear least squares, the plots of the obtained fits show that the finite element based fits are slightly better (Figure 5.14). This conclusion can be supported by the theoretical advantage of the

finite element model, namely, that it accounts for the effects of radial deformation of the cylinder in enforcing the loading condition. In contrast, Armstrong's model assumes that the radius of the cylinder changes only infinitesimally, an assumption that may be inaccurate for the strains considered in this study.

Parameter estimates obtained for the mean ultrasound creep curves from the tofu block differed greatly from those estimated for the tofu cylinders when cylindrical models were used in the curve fitting, typically producing Young's modulus values on the order of 32-50 kPa (Tables 5.4 and 5.5). In contrast, the finite element block model was able to produce much closer Young's modulus estimates of approximately 14-20 kPa, nearly identical to the range of the cylinder test estimates. In addition, the block model fit exhibited the highest R^2 value when the Poisson's ratio was constrained to be positive, and clearly produced the best fit to the experimental data (Figure 5.15). All of this highlights the large error that can result from applying the wrong poroelastic model to the curve fitting routine. Clinical experiments are more likely to mirror the loading of the tofu block, and so more appropriate models must be incorporated into poroelastic parameter estimation in those settings.

While the present study has made progress in demonstrating the importance of model assumptions in poroelastography parameter estimation, there is still much that can be done to increase our understanding of these effects, improve curve fitting procedures, and provide more flexible frameworks for poroelastography. Future studies should examine in more detail the effect of spatial variations, particularly in the temporal evolution of the EPR at large and small strains. These studies should also vary the compressor size to simulate various values of the area ratio $\hat{A}$. Other avenues of research include developing analytical models of poroelastic deformation in an infinite slab of finite height in response to a point load. This would simulate the condition $\hat{A} \to \infty$, and it may serve to be useful since the

poroelastic block solutions seem to converge towards each other as the area ratio increases. Finally, future work should focus on developing more flexible poroelastography methods that do not depend on such rigid assumptions. In particular, the present study did not address the assumption of spatial uniformity, which is perhaps the most likely assumption to fail in the clinic. To account for this, more general methods that reconstruct the poroelastic properties on a pixel by pixel basis must be developed. Posing the poroelastographic parameter estimation as an inverse problem using a full poroelastic continuum model with a spatially varying parameter field provides one approach for doing so. An initial investigation into this will be the subject of the next chapter.

5.5 Conclusions

In this chapter, I detailed the development of two finite element models of poroelastic deformation – a cylinder and a rectangular block – and used these to demonstrate the importance of geometric and strain magnitude assumptions on poroelastic parameter estimation methods that utilize curve fitting. In particular, I showed that Armstrong's solution to the KLM equations may not be accurate in poroelastography measurements utilizing large strains. Furthermore, I showed that assumptions of cylindrical geometry behave very differently from an alternative loading that clinical use may find more suitable. These differences exist not only in the axial strain history, but also in the behavior of the effective Poisson's ratio, a key component of poroelastography imaging. The predictions of the computational models were verified using experimental measurements of tofu cylinders and blocks under large strain. The results demonstrate the importance of utilizing accurate assumptions in poroelastic parameter estimation and suggest that more general methods may be more useful for obtaining accurate measurements in the

clinic.

Table 5.1: Material properties used in the finite element model of a poroelastic block under compression

Parameter	Value	Description
E	16	Young's Modulus (kPa)
ν	0.0	Poisson's Ratio
κ	$k\mu_f$	Permeability (m^2)
k	1×10^{-10}	Permeability ($m^4N^{-1}s^{-1}$)
α	1	Biot-Willis Coefficient
χ_f	0	Fluid compressibility (Pa^{-1})
μ_f	1.002	Fluid viscosity (mPa·s)
ϕ	0.3	Porosity (arbitrary)

Table 5.2: Parameter estimates and 95% confidence intervals obtained from curve fitting routines applied to creep curves measured experimentally from cylinders of tofu under compression. The Poisson's ratio was allowed to be negative in these fits. Method denotes the strain estimation method, either boundary tracking (BT) or RF tracking (RF). Model denotes the curve fit model, either Armstrong's solution (Arm) or the finite element cylinder model (FE).

Method	Model	ν	E (kPa)	$k \times 10^{-10}$ m^{4}N^{-1}s^{-1}	R^2
BT	Arm	-0.255 (-0.261, -0.250)	12.23 (12.20, 12.27)	2.299 (2.243, 2.354)	0.9889
RF	Arm	-0.318 (-0.326, -0.311)	13.70 (13.64, 13.75)	2.602 (2.523, 2.681)	0.9855
BT	FE	-0.146 (-0.151, -0.141)	16.49 (16.47, 16.52)	1.712 (1.668, 1.757)	0.9884
RF	FE	-0.220 (-0.227, -0.212)	17.85 (17.80, 17.90)	2.037 (1.970, 2.104)	0.9849

Table 5.3: Parameter estimates and 95% confidence intervals obtained from curve fitting routines applied to creep curves measured experimentally from cylinders of tofu under compression. The Poisson's ratio was required to be positive in these fits. Method denotes the strain estimation method, either boundary tracking (BT) or RF tracking (RF). Model denotes the curve fit model, either Armstrong's solution (Arm) or the finite element cylinder model (FE).

Method	Model	ν	E (kPa)	$k \times 10^{-10}$ m^{4}N^{-1}s^{-1}	R^2
BT	Arm	0.000 (-0.012, 0.012)	12.54 (12.35, 12.73)	1.206 (1.014, 1.397)	0.8458
RF	Arm	0.000 (-0.027, 0.027)	14.20 (13.89, 14.51)	1.243 (0.963, 1.523)	0.7947
BT	FE	0.001 (-0.011, 0.012)	16.58 (16.49, 16.68)	1.066 (1.066, 1.066)	0.9310
RF	FE	0.000 (-0.018, 0.018)	18.04 (17.83, 18.26)	1.068 (0.911, 1.225)	0.8763

Table 5.4: Parameter estimates and 95% confidence intervals obtained from curve fitting routines applied to creep curves measured experimentally from rectangular blocks of tofu under compression. The Poisson's ratio constraint is noted as positive (+) or free (+/-). Boundary tracking was used for the strain estimation. Model denotes the curve fit model, either Armstrong's solution (Arm), the finite element cylinder model (FE-Cyl), or the finite element block model (FE-Blk).

Model	ν	E (kPa)	$k \times 10^{-10}$ $m^4N^{-1}s^{-1}$	R^2	ν Constraint
Arm	-0.490 (-0.517, -0.464)	30.15 (29.85, 30.46)	0.682 (0.615, 0.721)	0.9076	+/-
FE-Cyl	-0.490 (-0.517, -0.463)	33.89 (33.61, 34.16)	0.670 (0.620, 0.721)	0.9155	+/-
FE-Blk	-0.490 (-0.575, -0.405)	10.16 (9.07, 11.25)	1.396 (1.229, 1.563)	0.9030	+/-
Arm	0.000 (-0.055, 0.055)	31.95 (30.85, 33.07)	0.253 (0.149, 0.357)	0.5818	+
FE-Cyl	0.000 (-0.049, 0.049)	35.36 (34.32, 36.40)	0.235 (0.148, 0.322)	0.6098	+
FE-Blk	0.000 (-0.003, 0.004)	13.95 (13.51, 14.40)	0.796 (0.634, 0.968)	0.7666	+

Table 5.5: Parameter estimates and 95% confidence intervals obtained from curve fitting routines applied to creep curves measured experimentally from rectangular blocks of tofu under compression. The Poisson's ratio constraint is noted as positive (+) or free (+/-). RF tracking was used for the strain estimation. Model denotes the curve fit model, either Armstrong's solution (Arm), the finite element cylinder model (FE-Cyl), or the finite element block model (FE-Blk).

Model	ν	E (kPa)	$k \times 10^{-10}$ $m^4N^{-1}s^{-1}$	R^2	ν Constraint
Arm	-0.490 (-0.520, -0.460)	40.94 (39.72, 42.16)	0.344 (0.302, 0.386)	0.8820	+/-
FE-Cyl	-0.490 (-0.518, -0.462)	44.11 (43.00, 45.22)	0.333 (0.296, 0.371)	0.8957	+/-
FE-Blk	-0.490 (-0.586, -0.394)	13.50 (11.74, 15.26)	0.655 (0.540, 0.770)	0.8567	+/-
Arm	0.000 (-0.081, 0.081)	47.62 (44.56, 5.067)	0.174 (0.060, 0.288)	0.4882	+
FE-Cyl	0.000 (-0.076, 0.076)	50.89 (47.96, 53.82)	0.166 (0.065, 0.267)	0.5059	+
FE-Blk	0.000 (-0.078, 0.081)	20.13 (18.86, 21.40)	0.470 (0.283, 0.657)	0.6733	+

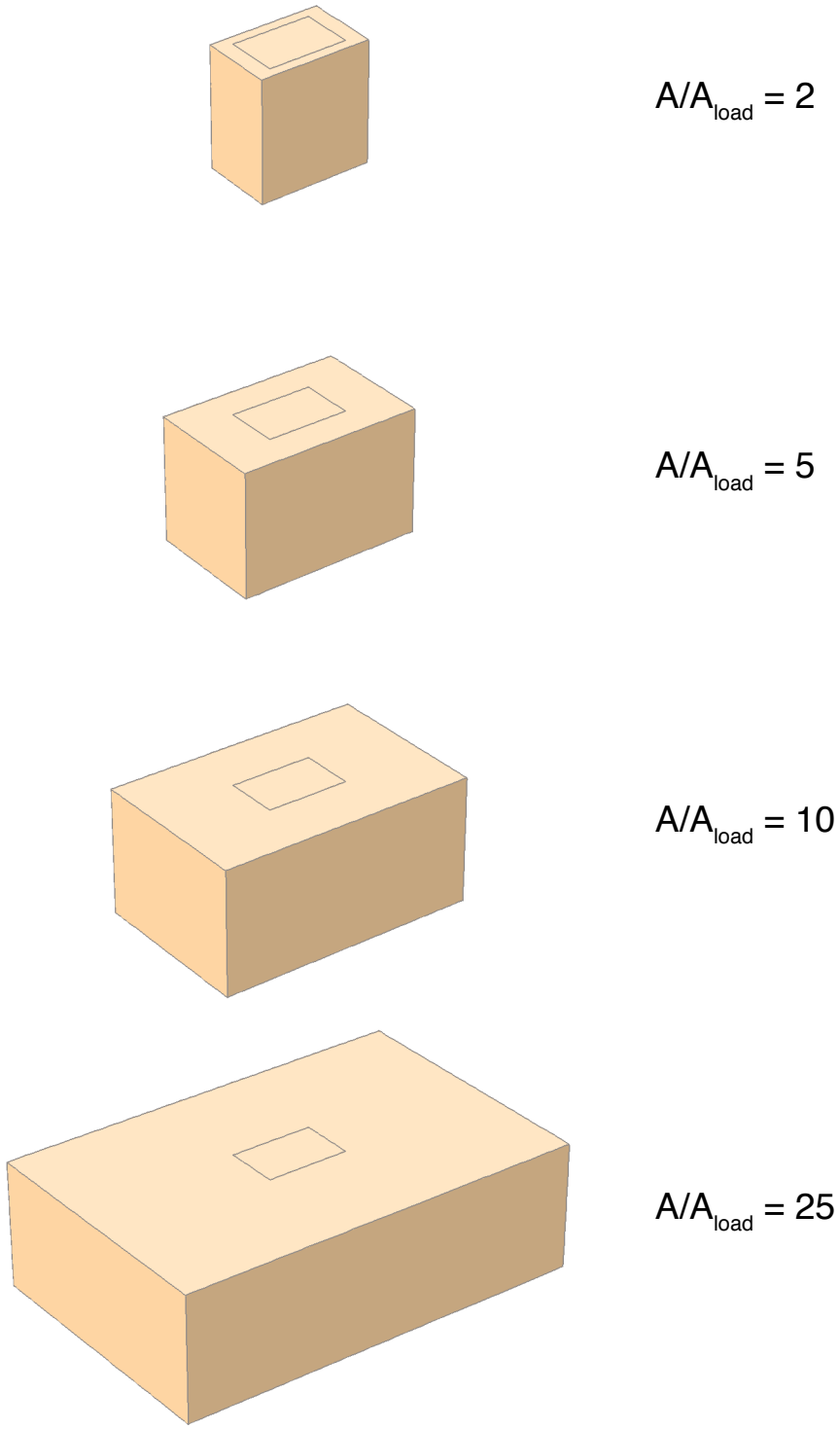

Figure 5.1: Poroelastic block geometry for different area ratios $\hat{A} = A/A_{load} = 2, 5, 10, 25$. The loading area is outlined in the center of the domain.

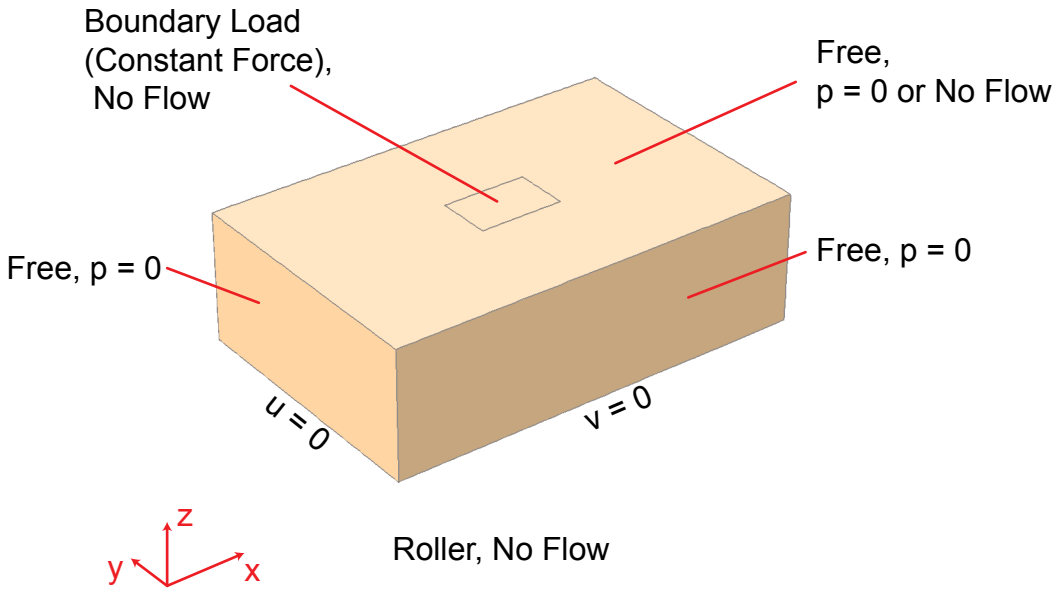

Figure 5.2: Boundary conditions for the poroelastic block finite element model.

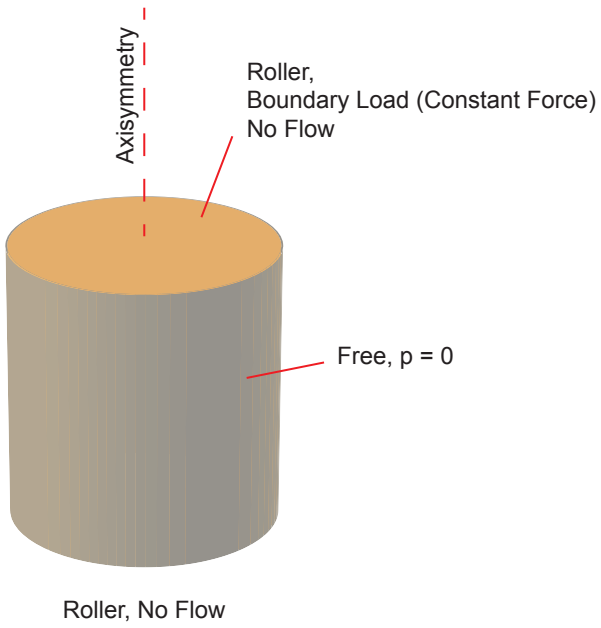

Figure 5.3: Boundary conditions for the poroelastic cylinder finite element model.

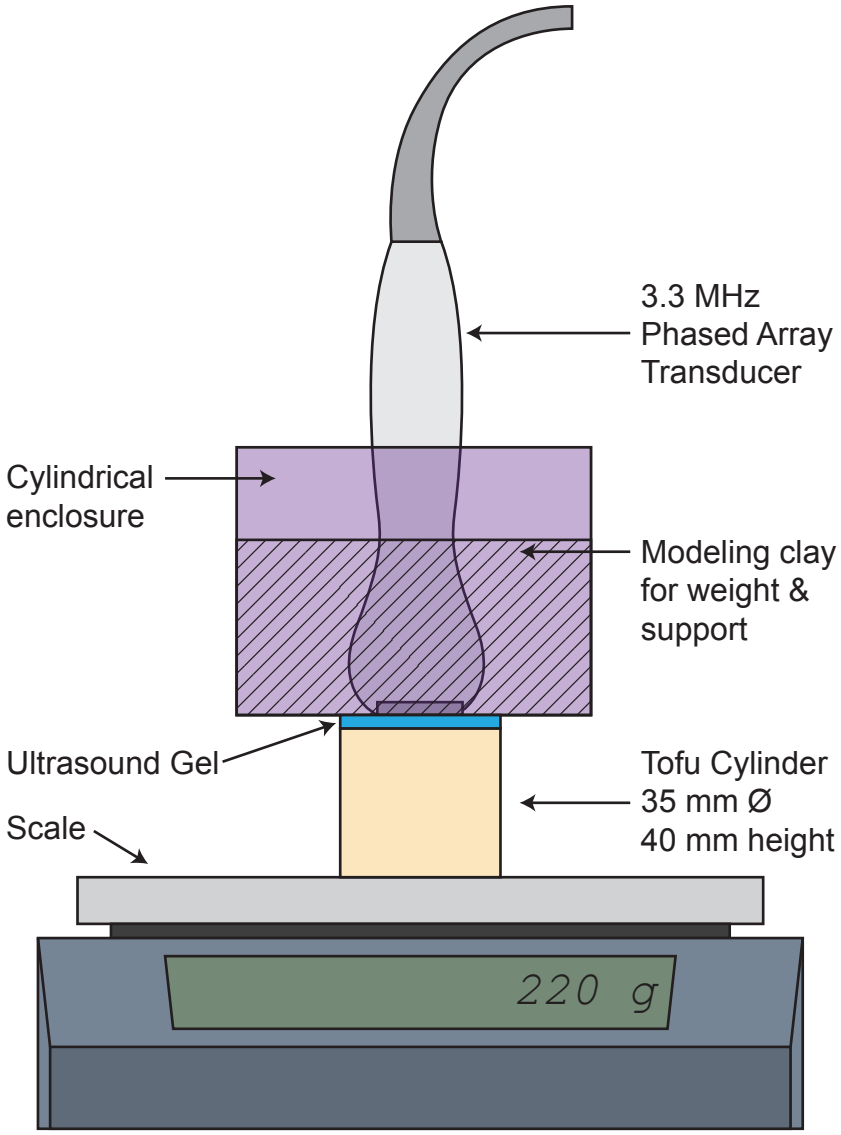

Figure 5.4: Experiment schematic for tofu cylinder experiments. An ultrasound transducer embedded in a cylindrical compressor was used to compress cylindrical samples of tofu.

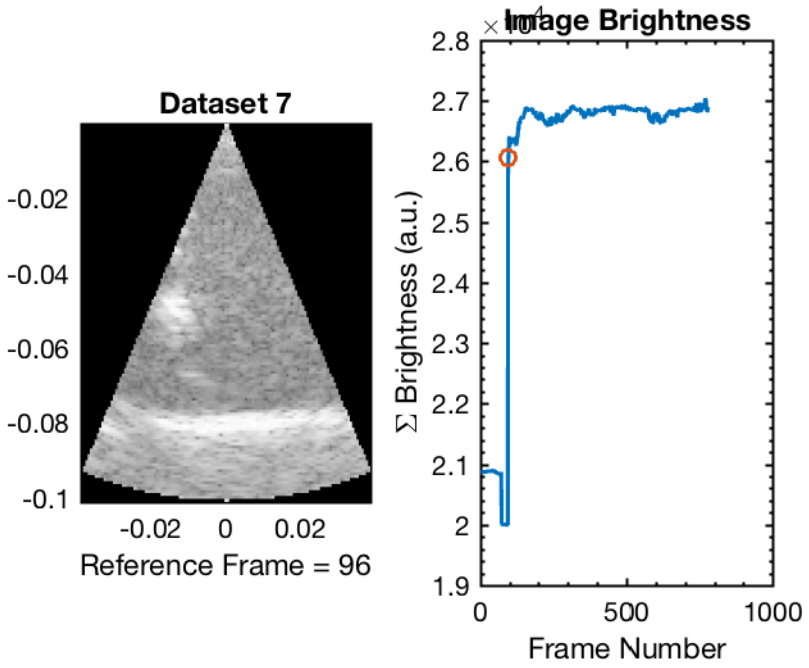

Figure 5.5: Example Bmode image and reference frame identification using the total pixel brightness.

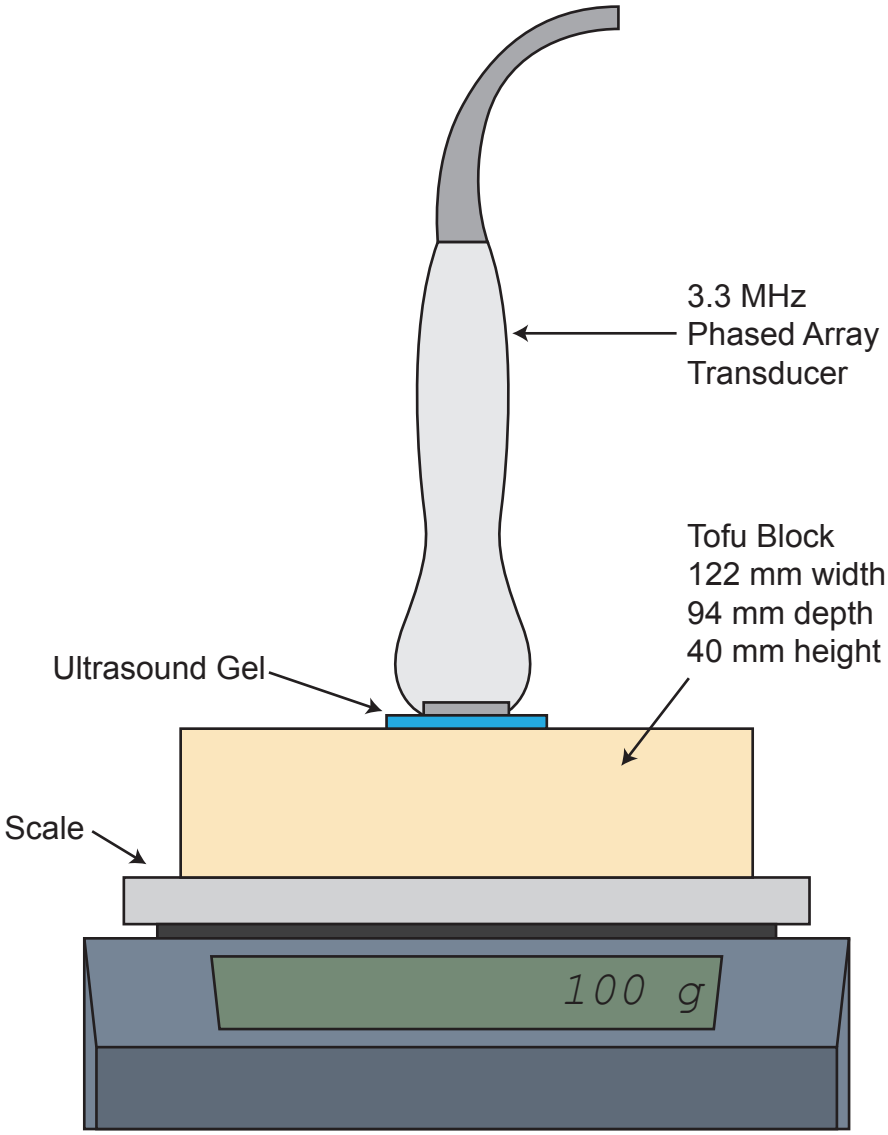

Figure 5.6: Experiment schematic for tofu block experiments. An ultrasound transducer was used to freehand compress a central region of a larger block of tofu.

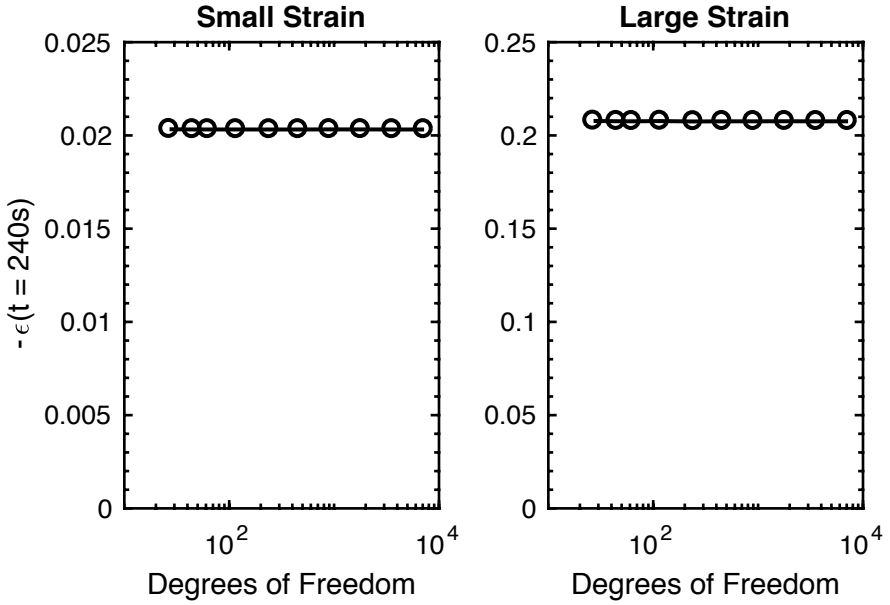

Figure 5.7: Mesh independence of the poroelastic cylinder finite element model showing that the axial strain at time t = 240 s does not change with the number of degrees of freedom in the model.

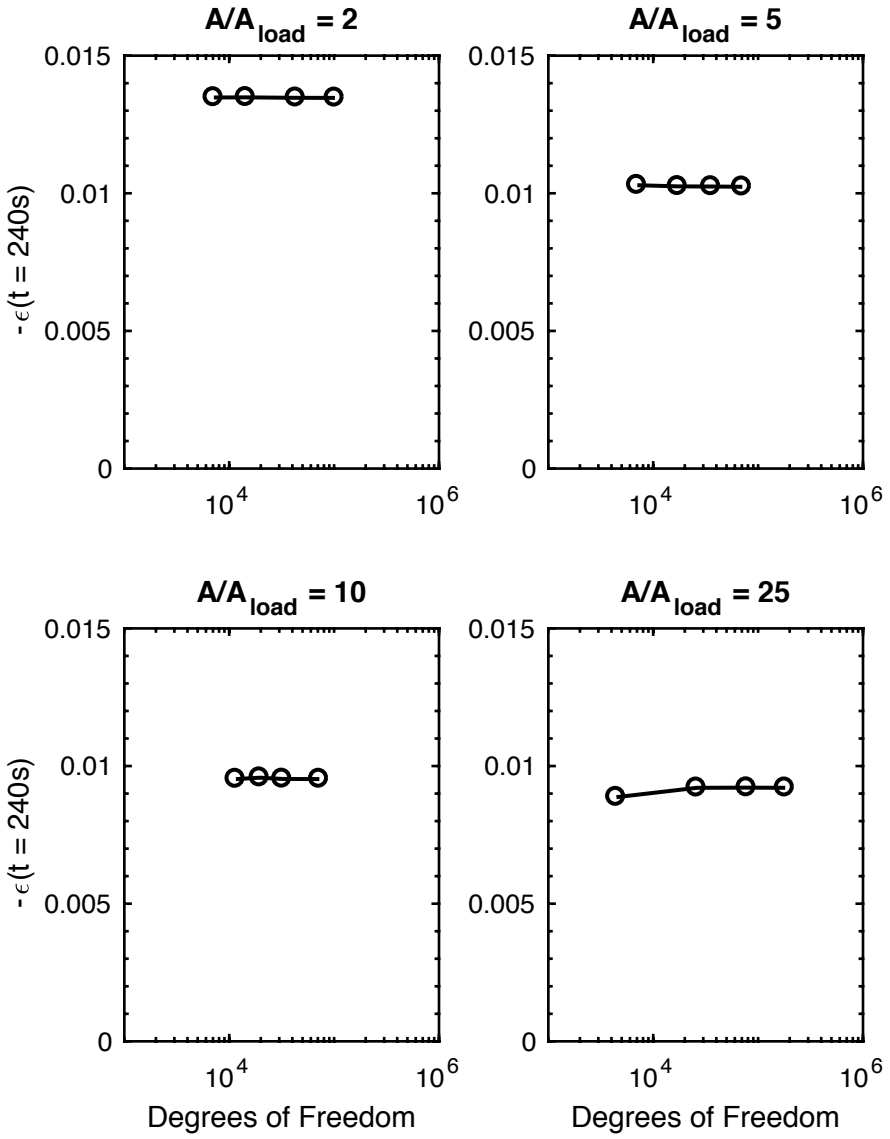

Figure 5.8: Mesh independence of the poroelastic block finite element model showing that the axial strain at time t = 240 s does not change with the number of degrees of freedom in the model for small strain.

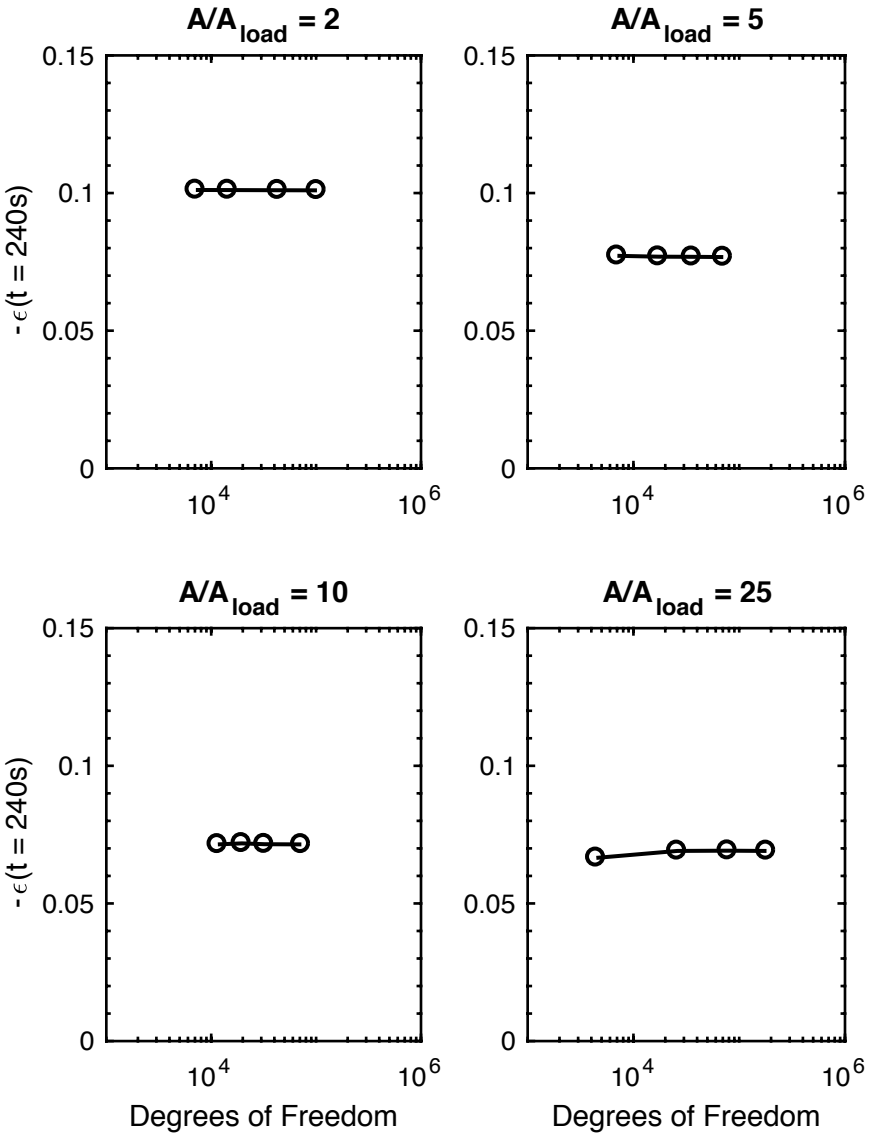

Figure 5.9: Mesh independence of the poroelastic block finite element model showing that the axial strain at time t = 240 s does not change with the number of degrees of freedom in the model for large strain.

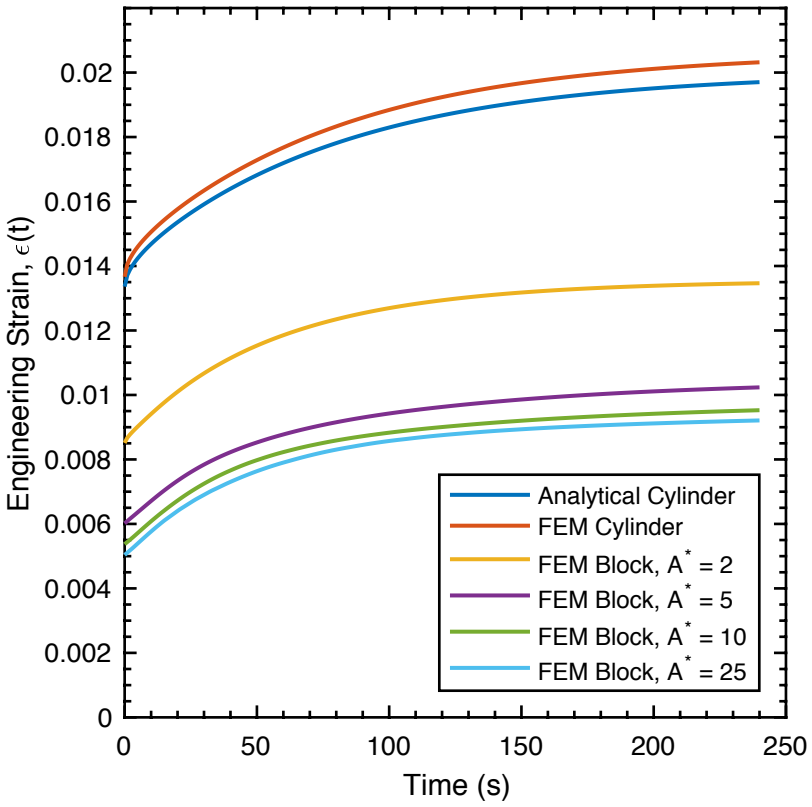

Figure 5.10: Comparison of Armstrong's biphasic creep solution to the poroelastic cylinder and block finite element models at small strain. The finite element cylinder model behaves similarly to the analytical solution, but the block geometry differs greatly as a consequence of the different loading conditions.

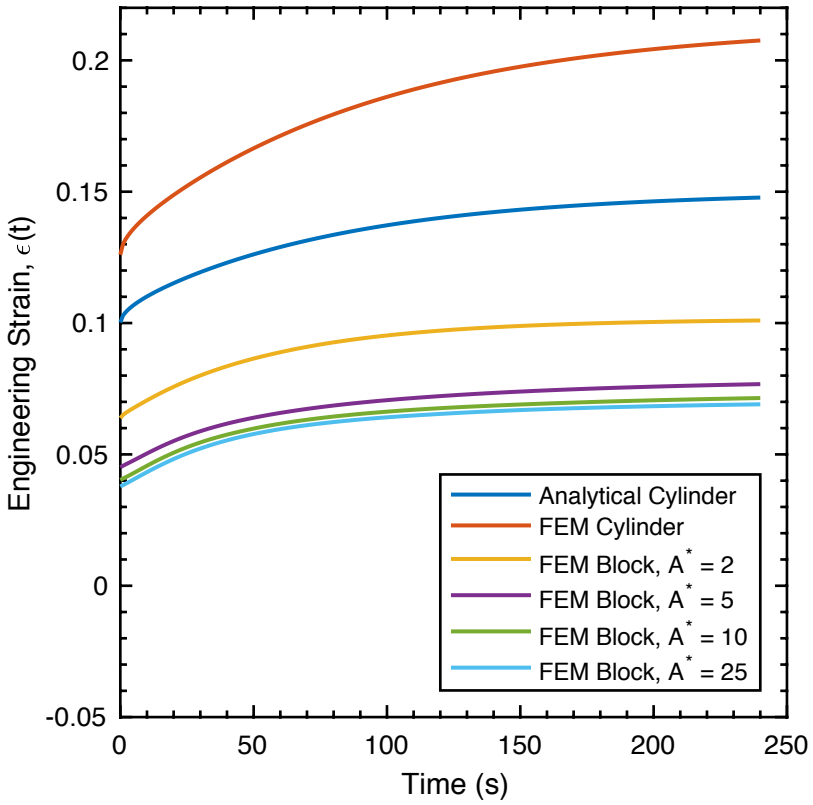

Figure 5.11: Comparison of Armstrong's biphasic creep solution to the poroelastic cylinder and block finite element models at large strain. Under these conditions, the finite element cylinder model differs greatly from the analytical solution, as does the the block geometry. This points to the increased importance of geometry and strain magnitude assumptions in poroelastography parameter estimation.

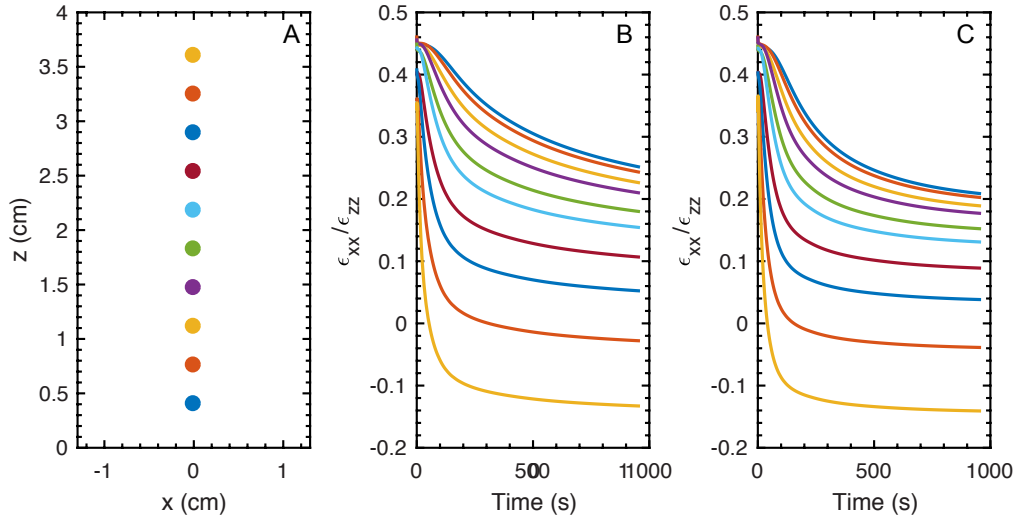

Figure 5.12: Evolution of the effective Poisson's ratio (EPR) as a function of time at various depths (A) below the compressor in the block finite element model when the top face is set to no flow conditions (B) or atmospheric pressure (C).

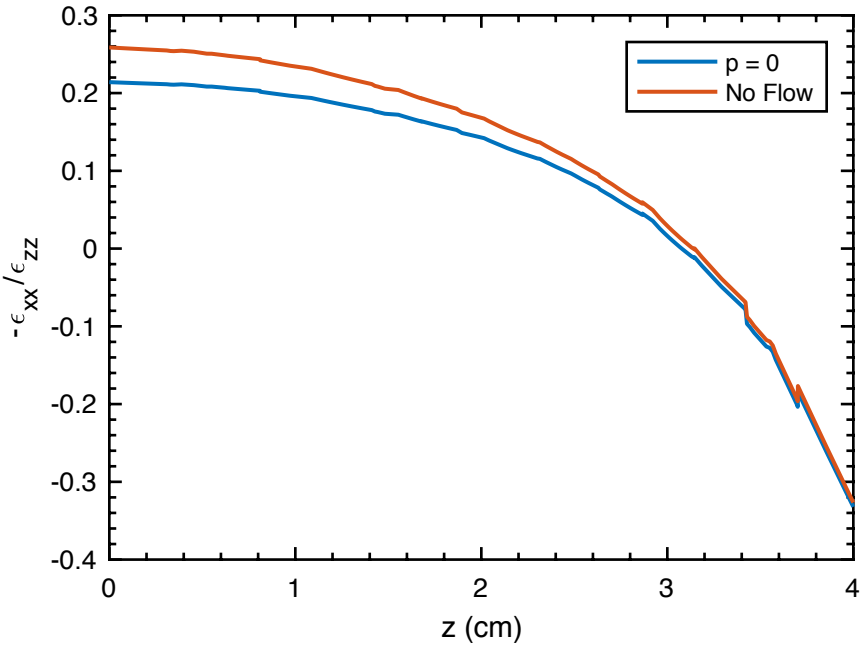

Figure 5.13: The effective Poisson's ratio (EPR) at steady state as a function depth in the block finite element model when the top face is set to no flow conditions or atmospheric pressure.

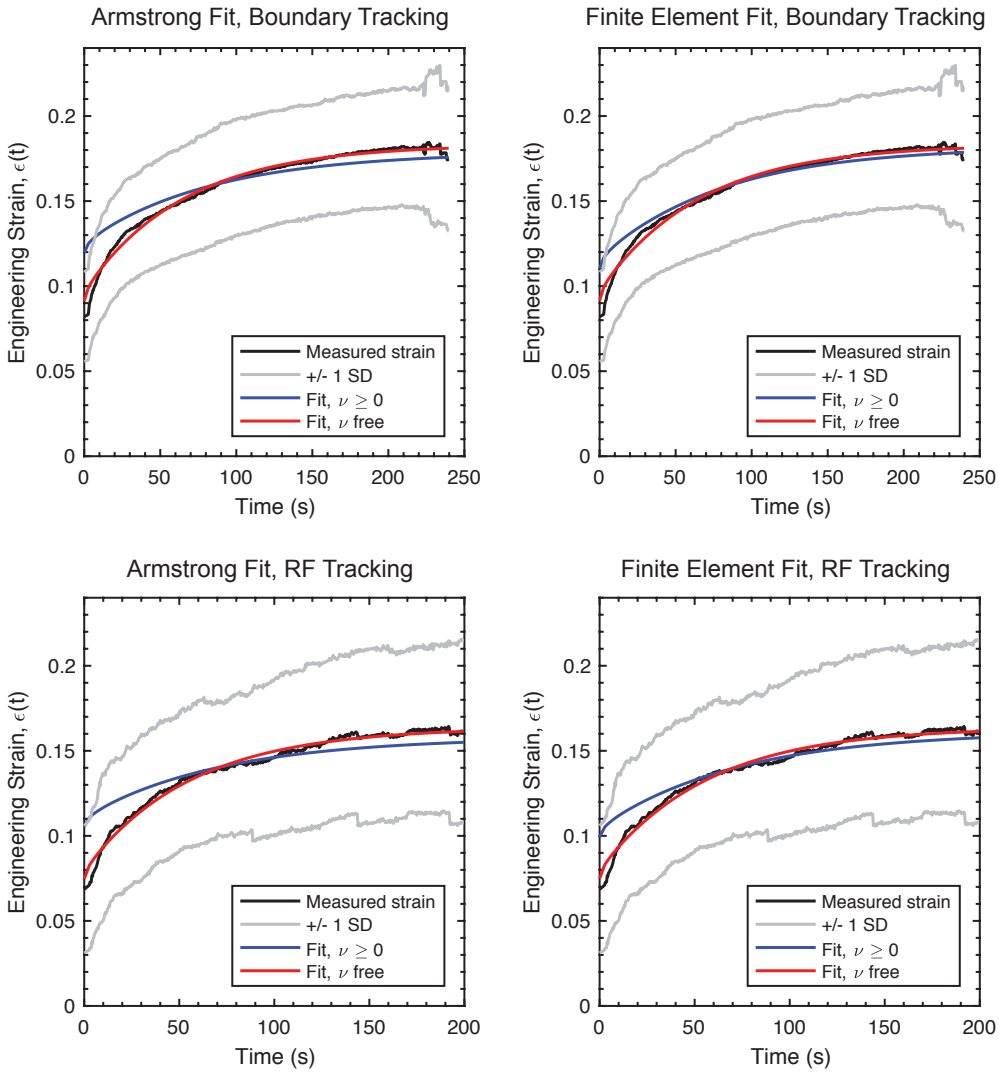

Figure 5.14: Mean strain history measured in tofu cylinders using ultrasound boundary tracking and RF tracking for strain estimation. The Armstrong and finite element cylinder models were fit to the measured data to yield poroelastic parameter estimates.

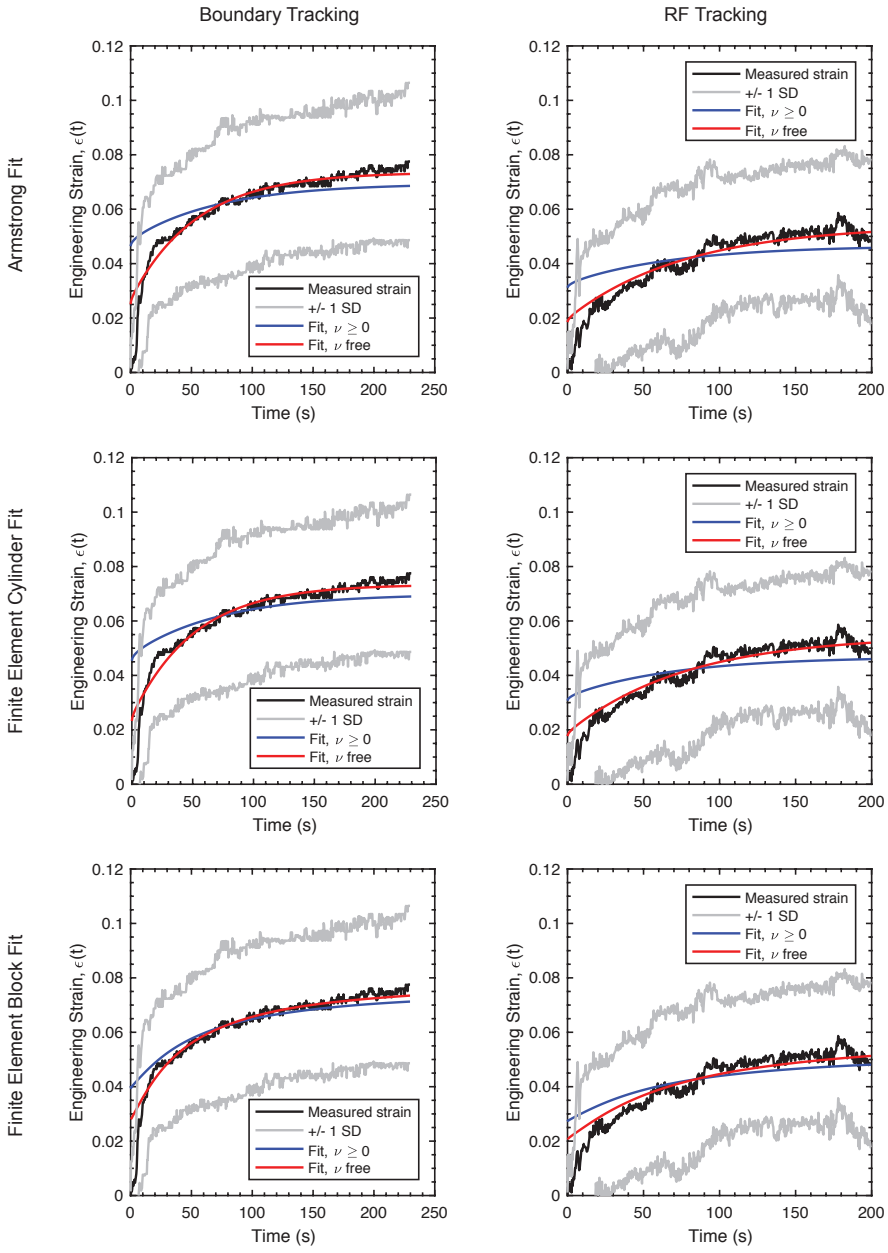

Figure 5.15: Mean strain history measured in tofu blocks using ultrasound boundary tracking and RF tracking for strain estimation. The Armstrong and finite element cylinder and block models were fit to the measured data to yield poroelastic parameter estimates.

BIBLIOGRAPHY

Armstrong, C. G., Lai, W. M., and Mow, V. C. (1984). An analysis of the unconfined compression of articular cartilage. *J. Biomech. Eng.*, 106(2):165–73.

Berry, G. P., Bamber, J. C., Armstrong, C. G., Miller, N. R., and Barbone, P. E. (2006a). Towards an acoustic model-based poroelastic imaging method: I. Theoretical foundation. *Ultrasound Med. Biol.*, 32(4):547–67.

Berry, G. P., Bamber, J. C., Miller, N. R., Barbone, P. E., Bush, N. L., and Armstrong, C. G. (2006b). Towards an acoustic model-based poroelastic imaging method: II. experimental investigation. *Ultrasound Med. Biol.*, 32(12):1869–85.

Berry, G. P., Bamber, J. C., Mortimer, P. S., Bush, N. L., Miller, N. R., and Barbone, P. E. (2008). The spatio-temporal strain response of oedematous and nonoedematous tissue to sustained compression in vivo. *Ultrasound Med. Biol.*, 34(4):617–29.

Biot, M. A. (1941). General theory of three-dimensional consolidation. *J. Appl. Phys.*, 12(2):155–164.

Doyley, M. M., Bamber, J. C., Fuechsel, F., and Bush, N. L. (2001). A freehand elastographic imaging approach for clinical breast imaging: system development and performance evaluation. *Ultrasound Med. Biol.*, 27(10):1347–57.

Fung, Y. (1993). *Biomechanics: Mechanical Properties of Living Tissues*. Springer New York, New York, NY, 2nd edition.

Galaz, B. A. and Acevedo, R. H. (2017). Optimization of a Pixel-to-Pixel Curve-Fitting Method for Poroelastography Imaging. *Ultrasound Med. Biol.*, 43(1):309–322.

Goenezen, S., Dord, J.-F., Sink, Z., Barbone, P. E., Jiang, J., Hall, T. J., and Oberai, A. a. (2012). Linear and nonlinear elastic modulus imaging: an application to breast cancer diagnosis. *IEEE Trans. Med. Imaging*, 31(8):1628–37.

Greaves, G. N., Greer, A. L., Lakes, R. S., and Rouxel, T. (2011). Poisson's ratio and modern materials. *Nat Mater*, 10(11):823–837.

Hall, T. (2003a). In vivo real-time freehand palpation imaging. *Ultrasound Med. Biol.*, 29(3):427–435.

Hall, T. J. (2003b). AAPM/RSNA physics tutorial for residents: topics in US: beyond the basics: elasticity imaging with US. *Radiographics*, 23(6):1657–71.

Hindmarsh, A. C., Brown, P. N., Grant, K. E., Lee, S. L., Serban, R., Shumaker, D. E., and Woodward, C. S. (2005). SUNDIALS: Suite of Nonlinear and Differential/Algebraic Equation Solvers. *ACM Trans. Math. Softw.*, 31(3):363–396.

Kim, Y. T., Kim, H. C., Inada-Kim, M., Jung, S. S., Yun, Y. H., Jho, M. J., and Sandstrom, K. (2009). Evaluation of tissue mimicking quality of tofu for biomedical ultrasound. *Ultrasound Med. Biol.*, 35(3):472–81.

Konofagou, E. E., Harrigan, T. P., Ophir, J., and Krouskop, T. A. (2001). Poroelasticity: Imaging the poroelastic properties of tissues. *Ultrasound Med. Biol.*, 27(10):1387–1397.

Nair, S. P. and Righetti, R. (2015). Resimulation of noise: a precision estimator for least square error curve-fitting tested for axial strain time constant imaging. *Phys. Med. Biol.*, 60(9):3515–3529.

Nair, S. P., Yang, X., Krouskop, T. a., and Righetti, R. (2011). Performance analysis of a new real-time elastographic time constant estimator. *IEEE Trans. Med. Imaging*, 30(2):497–511.

Perriñez, P. R., Kennedy, F. E., Van Houten, E. E. W., Weaver, J. B., and Paulsen, K. D. (2010a). Magnetic resonance poroelastography: an algorithm for estimating the mechanical properties of fluid-saturated soft tissues. *IEEE Trans. Med. Imaging*, 29(3):746–55.

Perriñez, P. R., Pattison, A. J., Kennedy, F. E., Weaver, J. B., and Paulsen, K. D. (2010b). Contrast detection in fluid-saturated media with magnetic resonance poroelastography. *Med. Phys.*, 37(7):3518–3526.

Qiu, Y., Sridhar, M., Tsou, J. K., Lindfors, K. K., and Insana, M. F. (2008). Ultrasonic viscoelasticity imaging of nonpalpable breast tumors: preliminary results. *Acad. Radiol.*, 15(12):1526–33.

Righetti, R., Garra, B. S., Mobbs, L. M., Kraemer-Chant, C. M., Ophir, J., and Krouskop, T. A. (2007a). The feasibility of using poroelastographic techniques for distinguishing between normal and lymphedematous tissues in vivo. *Phys. Med. Biol.*, 52(21):6525–41.

Righetti, R., Ophir, J., Garra, B. S., Chandrasekhar, R. M., and Krouskop, T. A. (2005a). A new method for generating poroelastograms in noisy environments. *Ultrason. Imaging*, 27(4):201–220.

Righetti, R., Ophir, J., and Krouskop, T. A. (2005b). A method for generating permeability elastograms and Poisson's ratio time-constant elastograms. *Ultrasound Med. Biol.*, 31(6):803–16.

Righetti, R., Ophir, J., Srinivasan, S., and Krouskop, T. A. (2004). The feasibility of using elastography for imaging the Poisson's ratio in porous media. *Ultrasound Med. Biol.*, 30(2):215–28.

Righetti, R., Righetti, M., Ophir, J., and Krouskop, T. A. (2007b). The feasibility of estimating and imaging the mechanical behavior of poroelastic materials using axial strain elastography. *Phys. Med. Biol.*, 52(11):3241–59.

Treece, G. M., Lindop, J. E., Gee, A. H., and Prager, R. W. (2008). Freehand Ultrasound Elastography with a 3-D Probe. *Ultrasound Med. Biol.*, 34(3):463–474.

Varghese, T. and Ophir, J. (1997). A theoretical framework for performance characterization of elastography: the strain filter. *IEEE Trans. Ultrason. Ferroelectr. Freq. Control*, 44(1):164–72.

Varghese, T., Ophir, J., and Cespedes, I. (1996). Noise reduction in elastograms using temporal stretching with multicompression averaging. *Ultrasound Med. Biol.*, 22(8).

Wu, J. (2001). Tofu as a tissue-mimicking material. *Ultrasound Med. Biol.*, 27(9):1297–1300.

Zhu, Y. N. and Hall, T. J. (2002). A modified block matching method for real-time freehand strain imaging. *Ultrason. Imaging*, 24:161–176.

CHAPTER 6

Evaluation of a model-based ultrasound poroelastography algorithm

6.1 Introduction

The mechanical properties of tissue have long been associated with its pathological state. Indeed, the practice of palpation for diagnosis has been around for millenia, since at least the time of Hippocrates (Walker, 1990). A natural extension of this diagnostic practice is to measure tissue mechanical properties quantitatively. Accurate quantitative estimates of tissue elasticity, compressibility, and temporal responses may help to improve a wide variety of diagnoses ranging from noninvasive tumor biopsy (Garra et al., 1997) to management of edema (Mridha and Odman, 1986).

Traditionally, ultrasound elastography has provided a useful platform for these investigations. Many different approaches to ultrasound elastography have been developed since the method was first proposed (Ophir et al., 1991). In its most basic form though, the method proceeds as follows. An ultrasound transducer is aligned with some region of interest, and a reference radiofrequency (RF) ultrasound image of the region is acquired. A small compressive stress is then applied to the tissue, and a second image is acquired. By applying time delay estimation techniques between corresponding RF A-lines in the pre- and post-compression

images, accurate estimates of the axial tissue displacement field can be obtained. Differentiation of this axial displacement with respect to the axial position yields a quantitative image of the axial tissue strain ε. Assuming stress uniformity, Hooke's law can be invoked to determine the Young's modulus E, or stiffness, of the tissue, provided the stress σ is known.

$$E = \frac{\sigma}{\varepsilon}$$

In tissues with non-uniform stiffness, the assumption of stress uniformity may not be accurate, leading to artifacts in the Young's modulus images. In addition, differentiation of the displacement estimates tends to amplify noise in the images. To address these issues, several studies have reformulated the Young's modulus estimation as an inverse problem (Skovoroda et al., 1994, 1995; Kallel et al., 1996; Doyley et al., 2000; Oberai et al., 2003, 2004; Doyley et al., 2005). While direct inversion schemes can be used (Skovoroda et al., 1994, 1995), they require sufficient knowledge of boundary loads and boundary properties to remain well-posed (Barbone and Bamber, 2002). More typically, these inverse problem approaches are posed as an iterative minimization,

$$E_{opt} = \underset{E}{\operatorname{argmin}} \|u_m - u(E)\|_2^2,$$

where u_m denotes a measured axial displacement and $u(E)$ is the solution to the forward elasticity problem for a given Young's modulus estimate. These inverse problem approaches tend to produce higher quality elastograms with more accurate quantitative estimates, particularly when the Young's modulus contrast is large (Doyley et al., 2005), though they do incur a greater computational expense.

Besides image quality, inverse problem formulations of elastography offer another advantage. They can be generalized to include material models other than linear elasticity. This is especially important given that many tissues, particularly

soft tissues, cannot adequately be described as linearly elastic (Fung, 1993). Rather, they often exhibit some combination of time-dependent behavior and nonlinear stress-strain relationships. This has led to interest in developing elastography approaches based on viscoelastic (Insana et al., 2004; Sridhar et al., 2007; Qiu et al., 2008; Zhang et al., 2012; Pitre, Jr et al., 2016), hyperelastic (Samani and Plewes, 2004; Goenezen et al., 2011), and poroelastic models (Konofagou et al., 2001; Berry et al., 2006a,b; Perriñez et al., 2009, 2010b,a).

One potentially useful application of elastography methods is quantifying the degree of clinical edema in patients with end stage renal disease (ESRD). In these patients, the kidneys no longer function to adequately control filtration and fluid balance. This can easily lead to fluid overload which can manifest as peripheral edema or life-threatening congestive heart failure. Studies have shown that 30% of ESRD dialysis patients may exceed recommended levels of fluid retention (Lindberg et al., 2009), and 10% of all ESRD clinical care episodes may be associated with fluid overload (Arneson et al., 2010). The current diagnosis for fluid overload is based on imprecise semi-quantitative measures such as observing the degree of indentation or "pitting" present when a clinician compresses the edematous limb with his or her thumb. Other methods such as the measurement of biochemical markers, interior vena cava diameter, bioimpedance, and blood volume have repeatedly shown that the clinical exam alone underestimates fluid overload in 24-37% of patients, making it an inadequate measure of fluid status (Kouw et al., 1993; Oe et al., 2000; Yashiro et al., 2007).

Poroelastography was originally proposed as a possible technique for improving edema quantification (Konofagou et al., 2001). With the development of new algorithms capable of accurately measuring both axial and lateral displacements and strains (Konofagou and Ophir, 1998), it became possible to also produce an accurate estimate of the tissue Poisson's ratio. For an isotropic linear elastic solid

under uniaxial compression, the Poisson's ratio is related to the lateral and axial strains ε_{lat} and ε_{axi}, respectively, by

$$\nu = -\frac{\varepsilon_{lat}}{\varepsilon_{axi}}.$$

As mentioned before, many tissues do not behave as linearly elastic solids, and this is particularly true of edematous tissue which exhibits a time-dependent stress response driven by fluid transport. Poroelastography therefore relies on, predictably, a poroelastic description of tissue.

The general three dimensional form of the linear poroelasticity equations was first derived by Biot (1941) within the context of soil consolidation. The Biot model describes the deformation of a porous solid matrix saturated with fluid. According to the this model, a poroelastic material deforms with the following constitutive relationship between the stress σ_{ij}, strain ε_{ij}, and pore pressure p, expressed here in tensor notation:

$$\sigma_{ij} = \lambda\epsilon\delta_{ij} + 2\mu\varepsilon_{ij} - \alpha p\delta_{ij}. \tag{6.1}$$

Here, $\epsilon = \varepsilon_{kk}$ is the volumetric strain, λ and μ are the first Lamé parameter and shear modulus of the bulk porous matrix, respectively, and α is the Biot-Willis coefficient. We also note that the strain tensor ε_{ij} can be defined in terms of the displacement field $u_i = (u, v, w)$,

$$\varepsilon_{ij} = \frac{1}{2}\left(u_{i,j} + u_{j,i}\right). \tag{6.2}$$

For an ideal porous matrix, α describes the compressibility of the bulk porous material relative to the compressibility of its solid phase. This is usually written in terms of the bulk modulus of the poroelastic material K and that of the solid phase

K_s,

$$\alpha = 1 - \frac{K}{K_s}. \tag{6.3}$$

For a poroelastic material with an incompressible solid phase, $K_s \to \infty$, and $\alpha = 1$.

The equilibrium equations for a poroelastic material can then be derived to describe the material's response to applied forces F_i,

$$\lambda \epsilon_{,i} + 2\mu \varepsilon_{ij,j} - \alpha p_{,i} + F_i = 0. \tag{6.4}$$

In three dimensions, this system of equations contains four unknowns u, v, w, and p. To close the system, we require a fourth equation to describe the evolution of the pressure field. Such an equation is obtained by assuming that fluid flow through the porous matrix behaves according the Darcy's law. The resulting pressure evolution equation is given by

$$\frac{1}{M}\frac{\partial p}{\partial t} - \frac{\kappa}{\mu_f} p_{,ii} = -\alpha \frac{\partial \epsilon}{\partial t}, \tag{6.5}$$

where κ is the permeability of the material and μ_f is the viscosity of the pore fluid. For an ideal poroelastic solid, the empirical Biot modulus $\frac{1}{M}$ can be defined in terms of more fundamental material constants,

$$\frac{1}{M} = \phi \chi_f + (\alpha - \phi)\frac{1 - \alpha}{K}, \tag{6.6}$$

where ϕ is the material porosity, χ_f is the pore fluid compressibility, and K is the bulk modulus. It is important to note that the bulk modulus K can be calculated from the parameters λ and μ and is therefore not an additional independent poroelastic parameter.

A separate model of poroelasticity, the biphasic Kuei-Lai-Mow (KLM) model, was developed in the 1980s to describe the poroelastic stress response of cartilage

(Kuei et al., 1978; Mow and Kuei, 1980; Mow and Lai, 1980). It has been shown that this model is equivalent to the Biot model (Simon, 1992). For the case of uniaxial compression of a uniform poroelastic cylinder, Armstrong et al. (1984) derived an analytical solution to the KLM model. In the steady state limit, this solution predicts that the strain ratio $-\varepsilon_{lat}/\varepsilon_{axi}$ approaches the Poisson's ratio of the drained poroelastic material. Previous poroelastography studies have taken advantage of this behavior and of Armstrong's solution, leading to two common poroelastography approaches.

The first poroelastography approach is analogous to the basic elastography process described previously (Konofagou et al., 2001; Righetti et al., 2004). In this case, however, lateral and axial displacements and strains are estimated over a time series of ultrasound images. The strain ratio, also termed the effective Poisson's ratio (EPR), is then computed for each image to display the time dependent behavior of the material under compression

$$EPR = -\frac{\varepsilon_{lat}}{\varepsilon_{axi}}.$$

As the system approaches steady state, the EPR is assumed to approach the drained Poisson's ratio.

The second common poroelastography approach seeks to construct parametric images of other important poroelastic parameters. This approach builds on the first approach, using the same estimates of the lateral strain, axial strain, and EPR. For each pixel in the time series of poroelastograms, either Armstrong's analytical model (Righetti et al., 2005; Berry et al., 2006a,b) or a simple exponential function (Righetti et al., 2007b; Nair et al., 2011; Nair and Righetti, 2015) is then fit to the measurements. This curve fitting procedure produces parametric images of poroelastic parameters that are more difficult to measure directly, for exam-

ple, the permeability, aggregate modulus, axial strain time constant, and EPR time constant. In the case of permeability and aggregate modulus (derived from Armstrong's model) these parametric images are not interpreted as spatial variations since the model assumes homogeneity. In the case of time constants, the exponential model is meant to be descriptive rather than predictive and so the images can be interpreted as showing spatial material property variations, but these properties cannot be directly linked to the poroelastic properties of the Biot or KLM models.

In the previous chapter, I highlighted the importance of geometry and strain magnitude assumptions on poroelastography parameter estimation. The assumption that the EPR decays uniformly to the drained Poisson's ratio is not valid in all geometries and loading configurations. As such, care should be taken in interpreting EPR poroelastograms quantitatively. In addition, I showed that the choice of model and the validity of its assumptions greatly affect the parameter estimates produced by curve fitting methods. All of these principles may lead to difficulty in clinical translation for poroelastography.

Pilot clincial studies using traditional poroelastography to quantify lymphedema have met only limited success (Righetti et al., 2007a; Berry et al., 2008). These studies presented clinical case studies including the evolution of axial strain in edematous versus non-edematous limbs, time evolution of the EPR, and maps of the EPR time constant. Both studies showed that lymphedematous tissues and normal tissues exhibit significantly different behavior as measured by the EPR time constant and axial strain. As mentioned before, however, these parameters are descriptive of the fundamental poroelastic properties, but not fundamental properties themselves.

My goal in this study was to develop and test a new model-based poroelastography approach capable of producing accurate spatially varying images of fundamental poroelastic parameters. Unlike traditional elastograms and poroelas-

tograms, I sought to develop a method that did not assume spatial uniformity, was flexible in assigning boundary conditions, was robust against noise, and yielded fewer image artifacts. My approach poses poroelastography as an inverse problem based on the Biot poroelastic model. In this way, I make no assumptions of homogeneity or symmetry, and thus the approach represents a more general attempt at quantifying poroelastic tissue properties. In this chapter, I outline the formulation and implementation of this method and show that it outperforms traditional poroelastography techniques for ideal data corrupted by Gaussian noise. I then go on to analyze some difficulties associated with extending this behavior to displacement data measured from simulated ultrasound images.

6.2 Methods

This study focuses on developing a new poroelastography algorithm based on the Biot model of poroelasticity. In this section, I outline the formulation of the forward and inverse poroelasticity problems and my implementation for solving each in MATLAB (The Mathworks, Natick, MA). I then describe two simulation studies meant to test the performance of the algorithm, first using an ideal solution corrupted with various levels of Gaussian noise and second using simulated ultrasound data. All simulations were run on a machine with an Intel Xeon E5 processor with 6 cores running at 3.5 GHz. The machine had 64 GB of RAM, though typical memory usage was less than 2 GB.

6.2.1 Forward Poroelasticity Problem

The forward poroelasticity problem is defined as follows. Given the set of poroelastic parameters $\{\lambda, \mu, \kappa, \phi, \alpha\}$ and the set of pore fluid properties $\{\chi_f, \mu_f\}$, and given known body forces F_i and suitable boundary conditions, determine the dis-

placement field u_i and pressure field p that satisfy Equations 6.4 and 6.5. By suitable boundary conditions, I mean that the following must be prescribed: 1) the displacement, its derivative, or optionally an applied force on each boundary, and 2) the pressure or fluid flux on each boundary. In the present work, I consider the forward problem shown in Figure 6.1. I simplify the equations by considering only two-dimensional motion (plane strain) and by assuming that the body forces F_i are negligible. For boundary conditions, I enforce a constant force and uniform vertical displacement along the top boundary, a roller condition along the bottom boundary, and allow free displacement along the left and right boundaries. One corner of the domain is fixed to ensure that the solution is not singular. I also prescribe no flow conditions along the top and bottom boundaries and atmospheric pressure conditions along the left and right boundaries.

I implemented the forward poroelasticity problem solver using the finite element method in MATLAB. The weak form of the governing equations was discretized on a triangular mesh using isoparametric linear triangle finite elements. This produced a system of differential equations

$$\begin{bmatrix} 0 & 0 \\ M & L^T \end{bmatrix} \begin{bmatrix} \dot{u} \\ \dot{p} \end{bmatrix} + \begin{bmatrix} K & -L \\ 0 & H \end{bmatrix} \begin{bmatrix} u \\ p \end{bmatrix} - \begin{bmatrix} f \\ q \end{bmatrix} = \begin{bmatrix} 0 \\ 0 \end{bmatrix} \tag{6.7}$$

with $3N$ degrees of freedom. The submatrices are defined by sums over the finite

elements

$$K = \sum_e \int_{\Omega_e} B_e^T D_e B_e \mathrm{d}\Omega_e \tag{6.8}$$

$$L = \sum_e \int_{\Omega_e} \alpha B_e^T m N \mathrm{d}\Omega_e \tag{6.9}$$

$$H = \sum_e \int_{\Omega_e} \frac{\kappa}{\mu_f} (\nabla N)_e^T (\nabla N)_e \, \mathrm{d}\Omega_e \tag{6.10}$$

$$M = \sum_e \int_{\Omega_e} \phi \chi_f N^T N \mathrm{d}\Omega_e \tag{6.11}$$

where B_e is the element strain differential operator matrix, D_e is the elasticity coefficient matrix, N is the shape function vector, and ∇ is the gradient operator matrix. For more information, I refer the reader to Detournay and Cheng (1993) and Zienkiewicz and Taylor (2000). For present purposes, it is sufficient to note that only D_e is dependent on the first Lamé parameter and shear modulus. Specifically, D_e takes the form

$$D_e = \begin{bmatrix} \lambda_e + 2\mu_e & \lambda_e & 0 \\ \lambda_e & \lambda_e + 2\mu_e & 0 \\ 0 & 0 & \mu_e \end{bmatrix}. \tag{6.12}$$

The parameters λ and μ were assumed to be spatially varying, and their values were assigned on a regular grid of 15×15 pixels spanning the 5×5 cm domain. The values from this regular grid were linearly interpolated onto the element centroid coordinates of the free triangular finite element mesh. This mapping can be written as a matrix multiplication $x_{tri} = \mathcal{L} x_{grid}$, where $\mathcal{L} \in \mathbb{R}^{Nelm \times 15^2}$ is dependent only on the distances between the grid points and element centroids. This implementation is very convenient for relating the grid parameters, which will be very important in the inverse problem, and the element parameters λ_e and μ_e, which are very important in the forward problem. Specifically, the parameters for a given element in the finite element mesh are obtained by taking the dot product between

the e^{th} row of the $\mathcal{L}$ matrix and the vector of gridded parameter values.

$$\lambda_e = \mathcal{L}_e \cdot \lambda_{grid} \tag{6.13}$$

$$\mu_e = \mathcal{L}_e \cdot \mu_{grid} \tag{6.14}$$

The other parameters $\kappa, \phi, \alpha, \chi_f, \mu_f$ were assumed to be constant throughout the domain. Their assigned values are summarized in Table 6.1. Along the top boundary, I enforced a constant compressive stress of 12.9 Pa. This was meant to yield an approximate steady state strain of 1% in simulations. For time integration of the governing equations, I used an implicit backwards differentiation formula (BDF) solver (ode15i, MATLAB Version 2015a). The equations were solved from time 0-300 seconds. The solver was allowed to freely choose the optimal time steps, and solutions were exported at three second intervals.

Once the equations were solved, the results of the forward problem $f(x)$ were arranged as a column vector with the following organization:

$$f(x) = [u_1^{t_1}, v_1^{t_1}, u_2^{t_1}, v_2^{t_1}, ..., u_N^{t_1}, v_N^{t_1}, \tag{6.15}$$

$$u_1^{t_2}, v_1^{t_2}, u_2^{t_2}, v_2^{t_2}, ..., u_N^{t_2}, v_N^{t_2}, \tag{6.16}$$

$$..., \tag{6.17}$$

$$u_1^{t_f}, v_1^{t_f}, u_2^{t_f}, v_2^{t_f}, ..., u_N^{t_f}, v_N^{t_f}]^T. \tag{6.18}$$

The first $2N$ entries of $f(x)$ are the lateral and axial displacements at the first measurement time point $t_1 = 3$ s. The next $2N$ entries correspond to the next measurement time $t_2 = 6$ s, and this pattern continues until all measurement times are included, up to 300 s in 3 s increments with a final additional time point at 1500 s (approaching steady state).

6.2.2 Forward Sensitivity Problem

Solving the poroelastic inverse problem, as detailed in the next section, requires some knowledge of how the solution of the forward problem $f(x)$ varies with respect to the parameters λ and μ. Specifically, we wish to compute the derivative of the solution with respect to a given parameter. This is known as the sensitivity problem. The sensitivity is often computed using finite differences and two solves of the forward problem. In the present implementation, the forward sensitivity matrix S is computed by taking partial derivatives of the finite element system of equations, Equation 6.7, with respect to the elements of the parameter vector x_j, which might represent either λ_j or μ_j. For notational convencience, we rewrite Equation 6.7 in the condensed form

$$\hat{C}\dot{u} + \hat{K}u - \hat{f} = 0. \tag{6.19}$$

Taking the partial derivative with respect to x_j and remembering to apply the product rule, we find

$$\frac{\partial \hat{C}}{\partial x_j}\dot{u} + \hat{C}\frac{\partial \dot{u}}{\partial x_j} + \frac{\partial \hat{K}}{\partial x_j}u + \hat{K}\frac{\partial u}{\partial x_j} = 0. \tag{6.20}$$

From Equations 6.7-6.11, we note that only the K finite element submatrix depends on λ or μ via the elasticity coefficient matrix D_e. It follows then that we can simplify Equation 6.20 to

$$\hat{C}\frac{\partial \dot{u}}{\partial x_j} + \hat{K}\frac{\partial u}{\partial x_j} = -\frac{\partial \hat{K}}{\partial x_j}u. \tag{6.21}$$

Note that the matrices $\hat{C}$ and $\hat{K}$ and the solution vector u may be precomputed, and these are independent of parameter x_j that appears in the partial derivatives.

To solve Equation 6.21 for a given x_j, we must construct first the matrix $\frac{\partial \hat{K}}{\partial x_j}$.

Again referencing Equations 6.7-6.11, we see that

$$\frac{\partial \hat{K}}{\partial x_j} = \frac{\partial}{\partial x_j} \begin{bmatrix} K & -L \\ 0 & H \end{bmatrix} = \begin{bmatrix} \frac{\partial K}{\partial x_j} & 0 \\ 0 & 0 \end{bmatrix}. \tag{6.22}$$

By Equation 6.8, noting that only D_e depends on the parameters, we obtain

$$\frac{\partial K}{\partial x_j} = \sum_e \int_{\Omega_e} B_e^T \left(\frac{\partial D_e}{\partial x_j} \right) B_e \mathrm{d}\Omega_e \tag{6.23}$$

To determine $\frac{\partial D_e}{\partial x_j}$, we must first determine $\frac{\partial \lambda_e}{\partial x_j}$ and $\frac{\partial \mu_e}{\partial x_j}$. Refering to Equations 6.13-6.14, we have

$$\frac{\partial \lambda_e}{\partial x_j} = \mathcal{L}_e \cdot \frac{\partial \lambda_{grid}}{\partial x_j} = \begin{cases} \mathcal{L}_{ej} & x_j = \lambda_j \\ 0 & \text{otherwise} \end{cases} \tag{6.24}$$

$$\frac{\partial \mu_e}{\partial x_j} = \mathcal{L}_e \cdot \frac{\partial \mu_{grid}}{\partial x_j} = \begin{cases} \mathcal{L}_{ej} & x_j = \mu_j \\ 0 & \text{otherwise} \end{cases} \tag{6.25}$$

By combining Equations 6.12, 6.24, and 6.25, we can derive $\frac{\partial D_e}{\partial x_j}$ and, therefore, $\frac{\partial \hat{K}}{\partial x_j}$ via Equations 6.22 and 6.23. This means we now can compute the entire right hand side of Equation 6.21. As with the forward problem solution, we may solve this system of equations for $\frac{\partial u}{\partial x_j}$ using an implicit numerical integration scheme.

6.2.3 Inverse Poroelasticity Problem

The reconstruction of poroelastic constants from ultrasound measurements can be cast in the form of an inverse poroelasticity problem. The full inverse problem involves estimating the set of poroelastic parameters and fluid properties given known forces, boundary conditions, displacement field, and pressure field. In this study, I simplify the inverse problem by assuming that I have some a priori knowl-

edge of some of the poroelastic parameters, specifically κ and ϕ, and that they are uniform through out the domain. I also assume that the solid phase of the tissue is incompressible and therefore $\alpha = 1$. Finally, I assume that the pore fluid is water, thus providing values for both χ_f and μ_f.

With these simplifications, define the inverse problem as follows. Given the known body forces and suitable boundary conditions, and given measurements of the displacement field u, determine the parameters λ and μ that minimize the objective function

$$\Phi(x) = \|W(d - f(x))\|_2^2 + \beta R(x), \tag{6.26}$$

where W is a diagonal weighting matrix, d is the vector of the measured displacement data, $f(x)$ is the solution of the forward problem for the parameter vector x, β is a regularization parameter, and $R(x)$ is a regularization function. The parameter vector x here is defined

$$x = [\lambda_{grid}, \mu_{grid}]^T = [\lambda_1, \lambda_2, ..., \lambda_N, \mu_1, \mu_2, ..., \mu_N]^T. \tag{6.27}$$

and contains the Lamé parameters and shear moduli for N discrete points, defined on a regular grid of 15×15 pixels spanning a 5×5 cm domain. The data vector d has the same structure as the forward model solution $f(x)$ described in Equation 6.15. For the regularization function R, we choose an edge-preserving hyperbola regularizer

$$R(\lambda_{grid}) = \sum_{i=1}^{N} \psi_i \left([C\lambda_{grid}]_i \right), \tag{6.28}$$

$$\psi(t) = \delta^2 \left[\sqrt{1 + \left| \frac{t}{\delta} \right|^2} - 1 \right]. \tag{6.29}$$

where C is a two-dimensional, first order finite difference matrix and δ is a parameter that controls the level of the edge preservation. The regularizer, potential

function, and finite difference matrix were implemented using Jeff Fessler's Image Reconstruction Toolbox, available at `web.eecs.umich.edu/~fessler/`. The regularization parameter β controls the relative effect of the regularization term on the value of the objective function compared to the least squares term. In this study, I chose values of β that resulted in good images. This was a accomplished largely by trial-and-error. In practice, one may not have a priori knowledge of the true solution, and more rigorous techniques for choosing the regularization parameter can be applied such as the L-curve criteria or Generalized Cross Validation.

The goal of solving the inverse problem is to find the optimal parameter vector

$$x_{opt} = \underset{x}{\operatorname{argmin}}\, \Phi(x). \tag{6.30}$$

A number of approaches exist to solve this problem, but my approach is to use a trust-region algorithm, an iterative method for solving nonlinear least squares problems. This can be handled by the MATLAB function lsqnonlin, a nonlinear least squares solver, using only minor modifications. I first rewrite the objective function in the following form:

$$\Phi(x) = \|F\|_2^2, \tag{6.31}$$

$$F = \begin{bmatrix} W(d - f(x)) \\ \sqrt{\beta\left(\psi_i\left([C\lambda_{grid}]_i\right) + 1\right)} \\ \sqrt{\beta\left(\psi_i\left([C\mu_{grid}]_i\right) + 1\right)} \end{bmatrix}. \tag{6.32}$$

It can easily be shown that this objective is identical to Equation 6.26 up to an additive constant and thus represents an identical minimization problem.

At each iteration, the algorithm proceeds by minimizing a quadratic approximation to the objective function within some neighborhood of the current param-

eter estimate. That is, it solves the trust-region sub-problem

$$\min\{\frac{1}{2}s^T Hs + s^T g \text{ such that} \|Ds\| < \Delta\}, \tag{6.33}$$

where s is the update step, H is an approximation to the Hessian matrix of second derivatives, g is the gradient of the objective function, D is a diagonal scaling matrix, and Δ is the radius of the trust region. In the least squares case, this simplifies to solving

$$s = \text{argmin} \|Js - F\|_2^2, \tag{6.34}$$

where $J = J_{ij}$ is the Jacobian matrix of F, that is, the partial derivatives of the components F_i with respect to each parameter λ_j or μ_j.

To construct the Jacobian matrix, one must describe how each entry of F varies with respect to each parameter. Differentiating Equation 6.32 with respect to each parameter yields

$$J_{ij} = \frac{\partial F_i}{\partial x_j} = \begin{bmatrix} -W\frac{\partial u_i}{\partial \lambda_j} & -W\frac{\partial u_i}{\partial \mu_j} \\ P([C\lambda_{grid}]) & 0 \\ 0 & P([C\mu_{grid}]) \end{bmatrix} \tag{6.35}$$

$$P_j(t_i) = \frac{\sqrt{\beta}t_i C e_j}{2\sqrt{[\psi_i(t_i)+1]\left[1+\left|\frac{t_i}{\delta}\right|^2\right]}} \tag{6.36}$$

The matrices $\frac{\partial u_i}{\partial \lambda_j}$ and $\frac{\partial u_i}{\partial \mu_j}$ represent the forward sensitivities, obtained by solving the forward sensitivity problem once for each parameter λ_j and μ_j, as detailed in the previous section. Each solution vector of the forward sensitivity problem makes up a column of one of these matrices, and each row corresponds to a row of the vector $f(x)$, as described in Equation 6.15. The matrices $P(t_i)$ are simply the derivatives of the regularization terms with respect to the parameters. As before, C is a finite difference matrix and e_j is a vector of zeros with a one as the j^{th} entry.

I initialize the parameter vector x to some initial guess using standard elastography assumptions such as linear elasticity and stress uniformity. I first estimated the axial strain by differentiating the steady state displacement field with a local-least squares strain estimator with a 9-point stencil. This gave estimates of the lateral and axial strain. By dividing the known applied axial stress by the axial strain, I obtained an estimate of Young's modulus E_{obs}. I initialized the Poisson's ratio ν_{obs} using the observed lateral-to-axial strain ratio. These "observed" values of the Young's modulus and strain ratio are not equivalent to the true Young's modulus and Poisson's ratio in the plane strain case since the loading no longer corresponds to uniaxial compression. I therefore apply a correction to estimate the Young's modulus and Poisson's ratio:

$$E = \frac{E_{obs}}{1 - \nu_{obs}^2}, \tag{6.37}$$

$$\nu = \frac{\nu_{obs}}{1 + \nu_{obs}}. \tag{6.38}$$

The Young's modulus and Poisson's ratio were then converted into the Lamé parameter λ and shear modulus μ to form the initial parameter vector:

$$\lambda = \frac{E\nu}{(1+\nu)(1-2\nu)}, \tag{6.39}$$

$$\mu = \frac{E}{2(1+\nu)}. \tag{6.40}$$

6.2.4 Computer Simulations with Ideal Data

I first tested the poroelastic parameter reconstruction using synthetic displacement data generated by solving the forward poroelasticity problem as detailed previously. I set the "true" values of the poroelastic parameters λ and μ according to the following procedure. The domain consisted of a uniform background surround-

ing a more rigid and less compressible circular inclusion with a radius of 8.5 mm. For background values, I assigned a Young's modulus of 1290 Pa and a Poisson's ratio of 0.3 (for comparison, see Berry et al. (2006a)). The inclusion values were 6450 Pa for Young's modulus (five times stiffer than the background) and 0.45 for Poisson's ratio. I then converted these values to the λ, μ form. After solving the forward model, I added Gaussian white noise to each displacement field, varying the signal-to-noise ratio (SNR) with values of infinity (no noise), 50 dB, 40 dB, and 30 dB. This corresponds roughly to noise levels of 0, 0.3, 1, and 3%, respectively, which is identical to the cases tested by Oberai et al. (2003). Of note, a signal-to-noise ratio of 40 dB is typical of sonograms (Doyley et al., 2000), although this may be different from the noise level of ultrasound-based displacement estimates. The regularization parameter β was set to 1×10^{-10}, 1×10^{-6}, 3×10^{-6}, and 1×10^{-4} for each noise level, respectively (∞, 50, 40, 30 dB). These values were found by trial-and-error to yield the optimal results, but a more systematic approach, such as the L-curve criteria or Generalized Cross Validation, could be also be implemented. Because the noise is Gaussian with uniform SNR for all displacements, I set the weighting matrix W in Equation 6.26 equal to the identity matrix.

6.2.5 Computer Simulations with Simulated Ultrasound Data

I also tested the poroelastic parameter reconstruction using simulated ultrasound RF data. Two simulated phantoms were used. Both were similar to that described in the idealized data simulations. That is, the domain was a 5 cm $\times$ 5 cm square containing a circular inclusion of radius 8.5 mm. In both cases, the background Young's modulus was 1290 Pa, and the inclusion Young's modulus was 6450 Pa. In the first simulated phantom, the background value of the Poisson's ratio was 0.3 and the inclusion value was 0.45. In the second phantom, this was reversed so that the background value was 0.45 and the inclusion value was 0.3. A regularization

parameter of $\beta = 5 \times 10^{-4}$ was used for the first phantom, and a value of $\beta = 1 \times 10^{-4}$ was used for the second. As before, these were found by trial-and-error to yield the best images, but a more systematic approach could also be implemented. Boundary conditions and loads were the same as those described earlier.

For each simulated phantom, a time series of images was computed using a convolution model. Briefly, I assumed a 128 element linear array transducer with 5 MHz center frequency, 60% fractional bandwidth, 0.4 mm pitch, and 2 mm beamwidth. The two dimensional point spread function was written in the following form

$$\mathcal{P}(x, y) = \mathcal{P}_x(x)\mathcal{P}_y(y). \tag{6.41}$$

For a Gaussian pulse, one can assume that $\mathcal{P}_y(y)$ takes the form

$$\mathcal{P}_y(y) = \exp \frac{y^2}{2\sigma_y^2} \cos \frac{2\pi y}{\lambda_w}, \tag{6.42}$$

where σ_y is the pulse length and λ_w is the wavelength. I also assume that the lateral point spread function mimics a Gaussian function. This gives

$$\mathcal{P}_x(x) = \exp \frac{x^2}{2\sigma_x^2}, \tag{6.43}$$

where σ_x is related to the beamwidth b by

$$\sigma_x^2 = \frac{1}{8} \left(\frac{b}{\ln 2} \right)^2. \tag{6.44}$$

The RF frame $\mathcal{R}(x, y, t)$ was then computed by spatially convolving the point spread function $\mathcal{P}(x, y)$ with a scatterer distribution $\mathcal{S}(x, y, t)$, defined by a uniform field of scatterers with normally distributed scattering strength resampled

according to a known displacement field at each time t,

$$\mathcal{R}(x, y, t) = \mathcal{P}(x, y) * \mathcal{S}(x, y, t). \tag{6.45}$$

I verified that the envelope of each of the generated RF images followed a Rayleigh distribution, ensuring that each contained fully developed speckle.

Displacement estimation in the series of RF frames was perfomed using a similar algorithm to that described by Konofagou and Ophir (1998) using 3 mm kernels with 75% overlap, 16:1 lateral interpolation, 2.5 mm lateral search width, and no temporal stretching (since the strain is non-uniform, time varying, and not assumed to be known a priori). Displacement estimates were refined using a local cosine fit (Cespedes et al., 1995) of the normalized cross correlation peak to achieve subpixel accuracy. I then applied global and local outlier filters (Westerweel and Scarano, 2005) to remove spurious estimates which were then replaced with an inpainting algorithm based on a spring metaphor (D'Errico, 2012). The resulting displacement fields were then smoothed using robust spline smoothing (Garcia, 2010, 2011). Finally, the lateral and axial strains were estimated using a least-squares strain estimator with a 9-point stencil (Kallel and Ophir, 1997). The displacement estimates were then interpolated from the speckle tracking grid onto a finite element triangular mesh using spline interpolation.

The tracked displacement data require a more careful choice for the weighting matrix W. Each measurement carries with it a different degree of uncertainty, and this must be accounted for in the minimization. The Cramér-Rao Lower Bound (CRLB) gives the lowest theoretical estimate of the variance of an unbiased time-delay estimator. In the context of ultrasonic speckle tracking, an expression of the CRLB for displacement estimates was originally derived by Walker and Trahey

(Walker and Trahey, 1994),

$$\sigma^2_{CRLB} = \frac{3}{2f_c^3\pi^2 T(B^3 + 12B)} \left(\frac{1}{\rho^2} \left(1 + \frac{1}{SNR^2} \right)^2 - 1 \right), \tag{6.46}$$

where f_c is the center frequency, T is the kernel length, B is the fractional bandwidth, ρ is the normalized cross correlation coefficent, and SNR is the electronic signal-to-noise ratio of the RF data. In the present case, I did not add any additional noise to the simulated RF signals, and so $SNR \to \infty$. It is also worth noting that the lateral displacement estimates are far less accurate than the axial displacements. This is due to the higher resolution of ultrasound in the axial direction. In light of this, I set the weights of the horizontal displacement components to zero so that they are not used in the reconstruction. Furthermore, because the data are measured at points insided the domain and some padding is introduced by the speckle tracking procedure, it is possible that some of the elements of the data vector are extrapolated from the true measured data. I set the weights of these extrapolated values to zero as well. Together, these three ideas led to define the diagonal elements of the weighting matrix as follows:

$$W_{ii} = \begin{cases} 0 & \text{lateral displacements} \\ 0 & \text{extrapolated data} \\ \frac{1}{\sigma_{CRLB}} & \text{otherwise} \end{cases} \tag{6.47}$$

In this implementation, I normalized the weights to have a maximum value of 1. This is equivalent to multiplying the objective function terms by a constant and so does not affect the minimization. Figure 6.2 shows the relationship between the weighting value and the normalized cross correlation coefficient. I also tested different choices of the weighting matrix such as a full identity matrix or an identity matrix with zero weights for the lateral displacements. The importance of the

choice of weighting matrix will be explained in more detail in the Results and Discussion sections.

6.2.6 Computer Simulations with Simulated Ultrasound Data - Modified Regularization

In a second set of simulations, I also tested a modified version of the objective function regularization. The simulated phantom properties used were identical to the first simulated phantom described in the previous section, with an inclusion that was less compressible than the background. Ultrasound RF frames were simulated with the same convolution model, this time assuming a 10 MHz center frequency. The applied force used to generate displacements was doubled, producing a strain of roughly 2%. Furthermore, the frames were distributed equally in the time range with one frame for every 30 seconds over a duration of 1500 seconds. The same displacement and strain estimation techniques were applied, this time using a 1 mm kernel. This reconstruction used a modified version of the regularization, such that the objective function minimized was

$$\Phi(x) = \|W(d - f(x))\|_2^2 + \frac{\beta}{1000} R(\lambda_{grid}) + \beta R(\mu_{grid}), \tag{6.48}$$

$$R(\lambda_{grid}) = \sum_{i=1}^{N} \psi_i \left([C\lambda_{grid}]_i \right), \tag{6.49}$$

$$\psi_\lambda(t) = (10\delta)^2 \left[\sqrt{1 + \left| \frac{t}{10\delta} \right|^2} - 1 \right], \tag{6.50}$$

$$\psi_\mu(t) = (\delta)^2 \left[\sqrt{1 + \left| \frac{t}{\delta} \right|^2} - 1 \right]. \tag{6.51}$$

The changed scales of the regularization parameters were meant to better capture the difference is scales of the reconstruction parameters λ and μ. Equation 6.48

was then minimized, using the following weighting matrix:

$$W_{ii} = \begin{cases} 0 & \text{lateral displacements} \\ 0 & \text{extrapolated data} \\ 1 & \text{otherwise} \end{cases} \tag{6.52}$$

The reconstructions were run first on a 15×15 pixel grid, as before, and then on a 36×36 grid for comparison at higher resolution. In the former case, the regularization parameters were set as $\beta = 0.01$ and $\delta = 1000$, while in the latter reconstruction, they were set as $\beta = 1$ and $\delta = 1000$.

6.3 Results

6.3.1 Computer Simulations with Ideal Data

Figures 6.3 and 6.4 show the reconstructed Lamé parameter and shear modulus, respectively, along the cutline $y = 2.5$ cm for the SNR = ∞, 50, 40, and 30 dB cases alongside the target, or true, parameter fields. As the SNR decreases, artifacts and errors become more apparent in the solution data. This is particularly true for the Lamé parameter, which was underestimated in the SNR = 30 dB case. In contrast, the shear modulus appears to be quite robust to errors in the reconstruction, and apart from some "salt-and-pepper" noise, remains accurate at all noise levels.

Figure 6.5 shows the mean values of the reconstruction parameters in the inclusion and background along with their standard deviations. The reconstructions match the true values very closely with very small standard deviations both inside the inclusion and within the background. In contrast, standard elastography and poroelastography methods (corresponding to my algorithm's initial parameter values) tend to overestimate the background values and underestimate the

inclusion values. These methods also exhibit larger standard deviations, on the order of 0.1-4 kPa. In all cases both the error and standard deviation tend to increase as the SNR increases.

Converting the reconstruction parameters λ and μ into the Young's modulus and Poisson's ratio also helps to compare my algorithm to existing elastography and poroelastography methods. The errors of the reconstruction and the traditional methods for both of these parameters are summarized in Table 6.2. Figure 6.6 shows the reconstructed Young's modulus elastograms alongside those obtained by standard elastography methods, namely computing the ratio of the uniform applied stress to the measured strain. In all cases, my algorithm produced sharper, more accurate images of the Young's modulus. The differences are even more striking when comparing Poisson's ratio elastograms (Figure 6.7). The present method greatly outperforms the standard axial-to-lateral strain ratio method at all noise levels, though this comes at a computational cost. Algorithm runtimes averaged 3-3.5 hours.

6.3.2 Computer Simulations with Simulated Ultrasound Data

6.3.2.1 Synthetic Ultrasound Images, Displacement, and Strain Estimates

Figures 6.8 and 6.9 show example brightness (B-mode) images and histograms of the RF envelope data for the simulated ultrasound frames. The envelope histograms were observed to follow a Rayleigh distribution, suggesting that the simulated frames contain fully developed speckle. Speckle tracking of the simulated RF yielded estimates of the axial and lateral displacement fields as a function of both space and time. Figure 6.10 compares the estimated displacements to the true values used to displace the scatterers during image simulation. The strain estimator was then applied to produce images of the lateral and axial strain as well as the

observed and corrected EPR (Figure 6.11).

6.3.2.2 Simulated Phantom I: Less Compressible Inclusion

Figure 6.12 shows a comparison of the estimated Young's modulus and Poisson's ratio for standard elastography and poroelastography techniques and the model-based poroelastic reconstruction in the first simulated phantom case. In both methods, the Young's modulus is underestimated, but the standard elastography estimate tends to produce fewer artifacts. The Poisson's ratio images show very different behaviors. The standard poroelastography estimate does contain a peak near in the true inclusion location, but this peak has a value of 0.63, a non-physical value for Poisson's ratio. Furthermore, the standard poroelastography image also contains a very large amount of noise. In contrast, the reconstructed Poisson's ratio image very clearly identifies the correct size and location of the inclusion, but it provides a very poor quantitative estimate. While it estimated the background value correctly, the reconstruction produced an inclusion Poisson's ratio that was lower than the background, as opposed to the true value which was higher. These effects are more easily seen in Figure 6.13 which shows the Young's modulus and Poisson's ratio estimates along the line $y = 2.5$ cm. The algorithm runtime was 4.5 hours.

6.3.2.3 Simulated Phantom II: More Compressible Inclusion

Figure 6.14 shows a comparison of the estimated Young's modulus and Poisson's ratio for standard elastography and poroelastography techniques and my model-based poroelastic reconstruction for the second simulated phantom case. As before, both methods underestimated the true Young's modulus, with the standard method producing an elastogram with fewer artifacts. In the Poisson's ratio images, the standard method produces a poroelastogram that does not clearly delin-

eate the inclusion. As before, the reconstructed Poisson's ratio image very clearly identifies the correct size and location of the inclusion. In this case, however, the result is quantitatively accurate to a reasonable degree, predicting a peak inclusion Poisson's ratio of 0.35. Figure 6.15 shows the Young's modulus and Poisson's ratio estimates along the line $y = 2.5$ cm. The algorithm runtime was 9 hours.

6.3.2.4 Simulated Phantom III: Modified Regularization

Figure 6.16 shows a comparison of the estimated Young's modulus and Poisson's ratio for standard elastography and poroelastography techniques and my model-based poroelastic reconstruction using the modified regularization function defined in section 6.2.6 for the 15×15 pixel grid. In this case, the reconstruction produced accurate quantitative maps of the Poisson's ratio with some artifacts along the edges and the center line. The Young's modulus in the inclusion was significantly underestimated. These observations are both made more clear in the $y = 2.5$ cm cut line plots (Figure 6.17). The algorithm runtime was 10 hours.

Figure 6.18 shows a comparison of the estimated Young's modulus and Poisson's ratio for standard elastography and poroelastography techniques and my model-based poroelastic reconstruction using the modified regularization function defined in section 6.2.6 for the higher resolution 36×36 pixel grid. This reconstruction produced similar accurate quantitative maps of the Poisson's ratio. Artifacts along the edges were less pronounced, while artifacts along the centerline remained prominent. A new artifact in this reconstruction is the apparent widening of the inclusion in the Poisson's ratio image. The Young's modulus in the inclusion was underestimated even more so than in the 15×15 pixel grid, likely owing to the larger value of β used in the higher resolution case. The $y = 2.5$ cm cut line plots (Figure 6.19) show a similar pattern to the 15×15 pixel grid results, with the widening of the inclusion clearly visible. The algorithm runtime was 49 hours.

6.4 Discussion

Poroelastography techniques currenly rely on very limiting assumptions of spatial uniformity and specific geometry and loading conditions. They also tend to be highly prone to noise both because of the noise-amplifying effect of strain estimators (differentiation) and the inclusion of lateral displacement estimates which tend to be far less accurate than axial estimates. I have proposed an inverse problem formulation for poroelastic imaging that seeks to circumvent these issues.

Given a set of ideal displacement measurements corrupted by Gaussian distributed errors, the model-based poroelastography method can indeed outperform traditional poroelastography methods. This is clear from computer simulations performed with ideal data (see Figures 6.5-6.7). The method demonstrated good performance for the range of SNR values tested (SNR $\geq$ 30 dB). Standard poroelastography methods yielded greater uncertainty in estimating the background and inclusion values of the Lamé parameter and shear modulus, especially as the noise level increase. In particular, Poisson's ratio elastograms generated by standard methods begin to show an unacceptable level of noise as the SNR approaches 30 dB.

The advantages of the model-based method begin to fade away as the quality of the measurement data becomes more realistic. In practice, errors may not follow a perfect Gaussian distribution and may even be spatially and temporally dependent. Computer simulations with simulated ultrasound data highlight the challenges this poses. In these experiments, the model-based method still maintained some good advantages. In both simulated phantoms, it was able to delineate the shape and size of the inclusion from the background. In the case of a less compressible inclusion, however, this carried with it a very poor quantitative estimate. The case of a more compressible inclusion seemed to perform much better and could even be said to outperform the corresponding standard measurement.

It is unclear though if the algorithm tends to favor solutions of this shape, making this case predisposed to better performance.

We can attempt to answer some of the questions surrounding the difficulty encountered by these first two simulation studies by analyzing the residuals that would be generated by the "true" solution. That is, we consider how different the displacement measurements are from the displacements predicted for the true parameter fields. Figures 6.20 and 6.21 show the distribution of weighted displacement errors $W(d - f(x_{true}))$ between the measured displacements d and the estimated displacement for the true parameters $f(x_{true})$ for different choices of the weighting matrix W. For every choice of weighting used, there exists a nonzero bias in the weighted displacement error. The CRLB-based weighting used in the experiments greatly reduces the bias, but does not remove it completely. In both simulated phantoms, the CRLB weighting reduces the bias from approximately -7 μm to -2 μm. The simulated RF data were sampled at 80 MHz, however, which makes both of these biases smaller than the sampling resolution (9.6 μm). The model-based approach then is extremely sensitive to biased errors in the displacement estimates, since the ideal data experiments show good performance in presence of unbiased Gaussian errors. This sensitivity presents a challenge to the practicality of this method since it requires such a high degree of accuracy from the speckle tracking algorithm. In theory though, a more accurate speckle tracking algorithm with no bias and roughly Gaussian noise should vastly improve the performance of this method.

In the modified regularization simulations, the reconstructions produced highly accurate quantitative estimates of Poisson's ratio. Because multiple parameters varied between these simulations and the previous ones, it is difficult to ascertain the changes that most likely contribute to the improvement. In this case, the distribution of the data points in time, the strain magnitude, the regularization, and the

weighting all differed. Because of the long run times required to reconstruct a single image, analyzing these variables independently is computationally intractable in the present implementation. Nevertheless, the results of these simulations are encouraging and point to the potential usefulness of these poroelastic reconstruction methods. The observation that the higher resolution reconstruction reduced edge artifacts is also encouraging.

Despite the difficulties encountered in this study, I have shown that a more general framework for poroelastography parameter estimation can be achieved. The current implementation faces many barriers to clinical application, including computational efficiency, but it provides important proof of concept for this new approach to poroelastography. Future work should focus first on increasing computational efficiency of the model-based poroelastography reconstruction code. Implementation in a compiled language could decrease the amount of time required to solve the forward problem thus decreasing runtimes. In particular, efforts should be focused on increasing the efficiency of the forward sensitivity solver since the computation of the Jacobian dominates the runtime of the reconstruction. Once the computational efficiency of the implementation has been increased, systematic studies should be conducted to analyze the effects of the temporal sampling, strain magnitude, regularization parameters, and weighting matrix choice. Furthermore, the inclusion of lateral displacement data has not been fully explored, and this may have implications for solution convergence or uniqueness.

6.5 Conclusion

I have developed and tested a new ultrasound poroelastography method based on Biot poroelasticity and an inverse problem formulation. Compared to previous

poroelastic imaging methods, this approach reduces the number of assumptions imposed and allows for quantitative estimation of spatially varying poroelastic properties. I tested this method in a simulation study using both ideal data corrupted by zero mean Gaussian noise and using displacement measurements from simulated ultrasound images. For the case of ideal measurements and Gaussian noise, my method greatly outperforms traditional poroelastography methods. In the simulated ultrasound experiments, biases in the data pose a major challenge for the poroelastic reconstruction algorithm, and the quality of the parameter estimates greatly decreases. This sensitivity to measurement errors and the computational expense are both major challenges to the proposed method. Despite this, the method still is of theoretical value for the field of poroelastography and the study of inverse problems. Future studies should seek to investigate the effects of temporal sampling, grid resolution, and strain magnitude, and to increase the robustness of this method to measurement errors, either through improved data weighting or the use of different objective functions or regularizers. Efforts to improve computational efficiency may also facilitate future studies.

Table 6.1: Summary of the poroelastic parameters used in solving the forward model.

Parameter	Value
Permeability, κ	1×10^{-12} m^2
Porosity, ϕ	0.333
Biot-Willis coefficient, α	1
Fluid compressibility, χ_f	4.4×10^{-10} Pa^{-1}
Fluid viscosity, μ_f	1.002×10^{-3} Pa $\cdot$ s

Table 6.2: Mean relative errors of poroelastograms produced with the model-based method (Recon) and traditional poroelastography methods (Trad) at varying noise levels.

SNR (dB)	Young's Modulus Error (%)		Poisson's Ratio Error (%)	
	Recon	Trad	Recon	Trad
∞	0.008	18.86	0.005	4.84
50	0.68	18.94	0.79	5.43
40	1.80	18.83	2.16	8.35
30	4.71	22.43	5.66	21.42

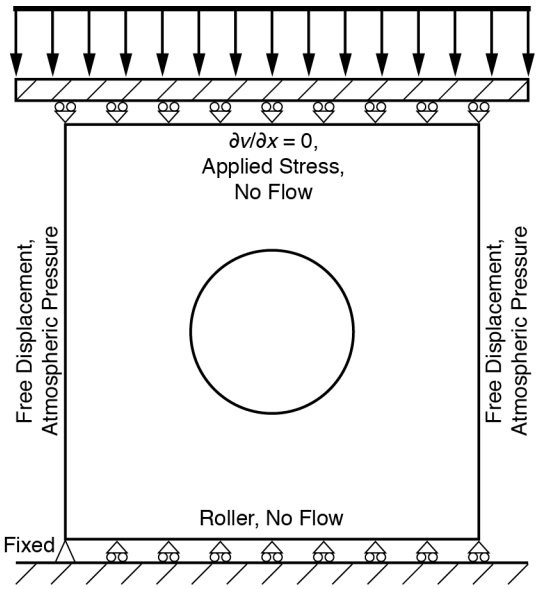

Figure 6.1: Schematic of the forward poroelasticity problem with boundary conditions and loading shown.

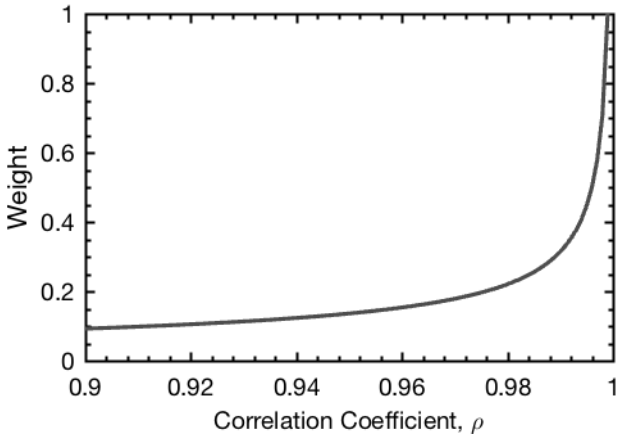

Figure 6.2: Relationship of the weighting values, as defined by the Cramér-Rao Lower Bound, to the normalized cross correlation coefficient.

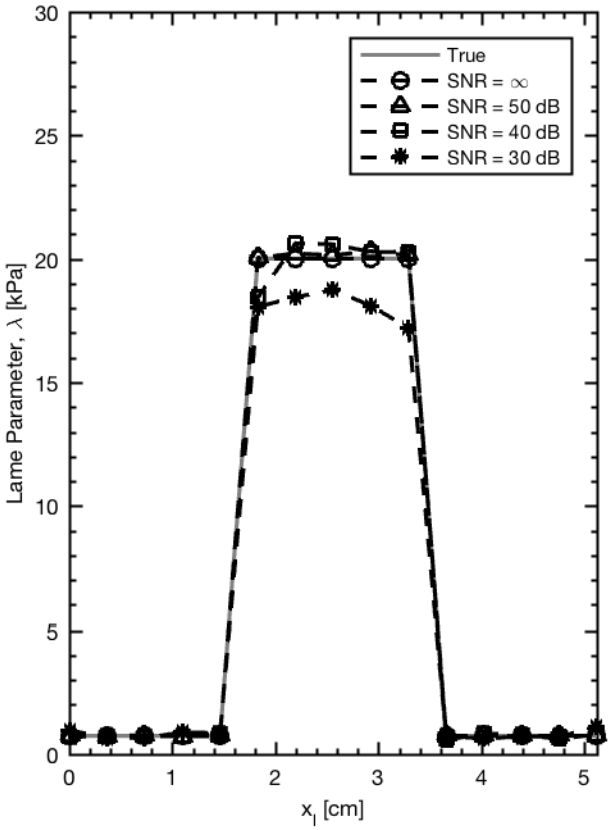

Figure 6.3: Reconstructed values of λ along the line $y = 2.5$ cm for various SNR levels.

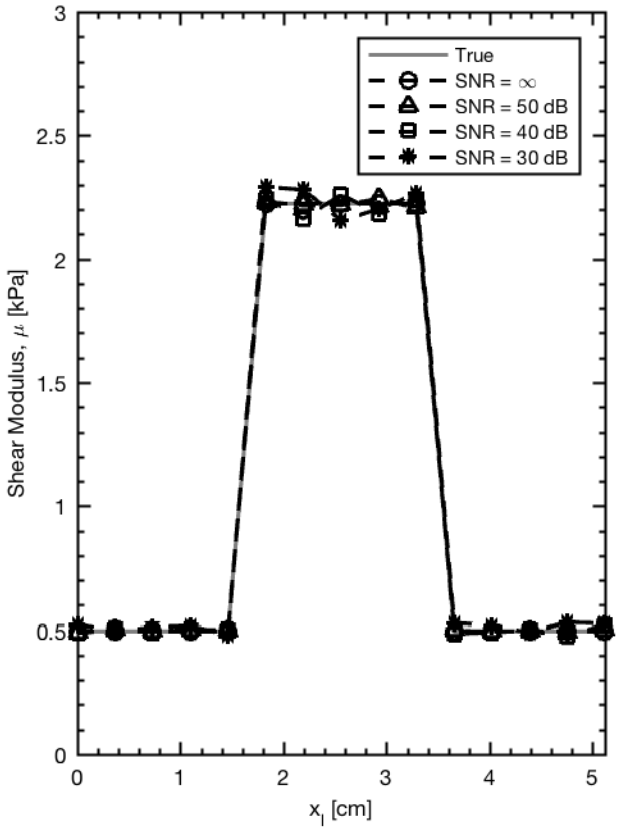

Figure 6.4: Reconstructed values of μ along the line $y = 2.5$ cm for various SNR levels.

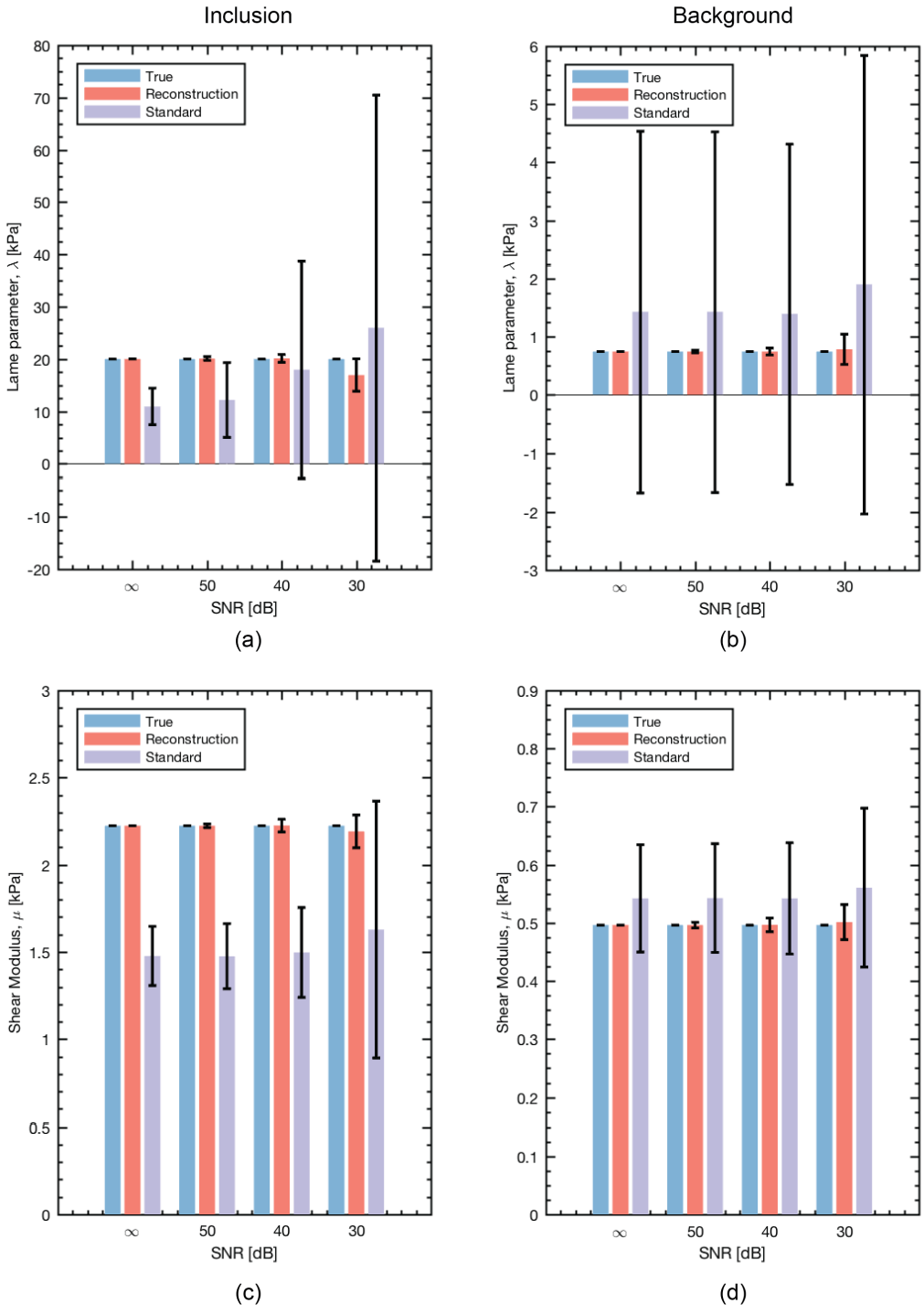

Figure 6.5: Mean values of the reconstruction parameters and standard deviations for (a) Lamé parameter in the inclusion, (b) Lamé parameter in the background, (c) shear modulus in the inclusion, (d) shear modulus in the background.

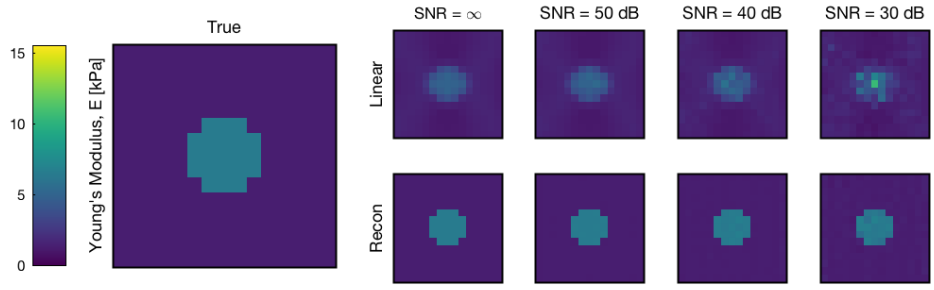

Figure 6.6: Comparison of the Young's modulus for the proposed reconstruction method (Recon) and the standard elastography estimate (Linear) for various SNR values.

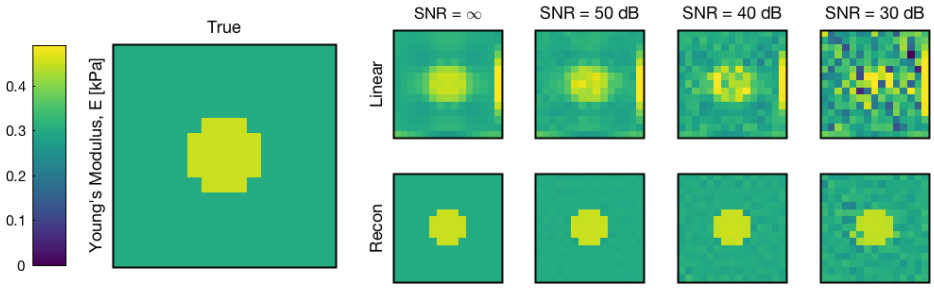

Figure 6.7: Comparison of the Poisson's ratio for the proposed reconstruction method (Recon) and the standard poroelastography estimate (Linear) for various SNR values.

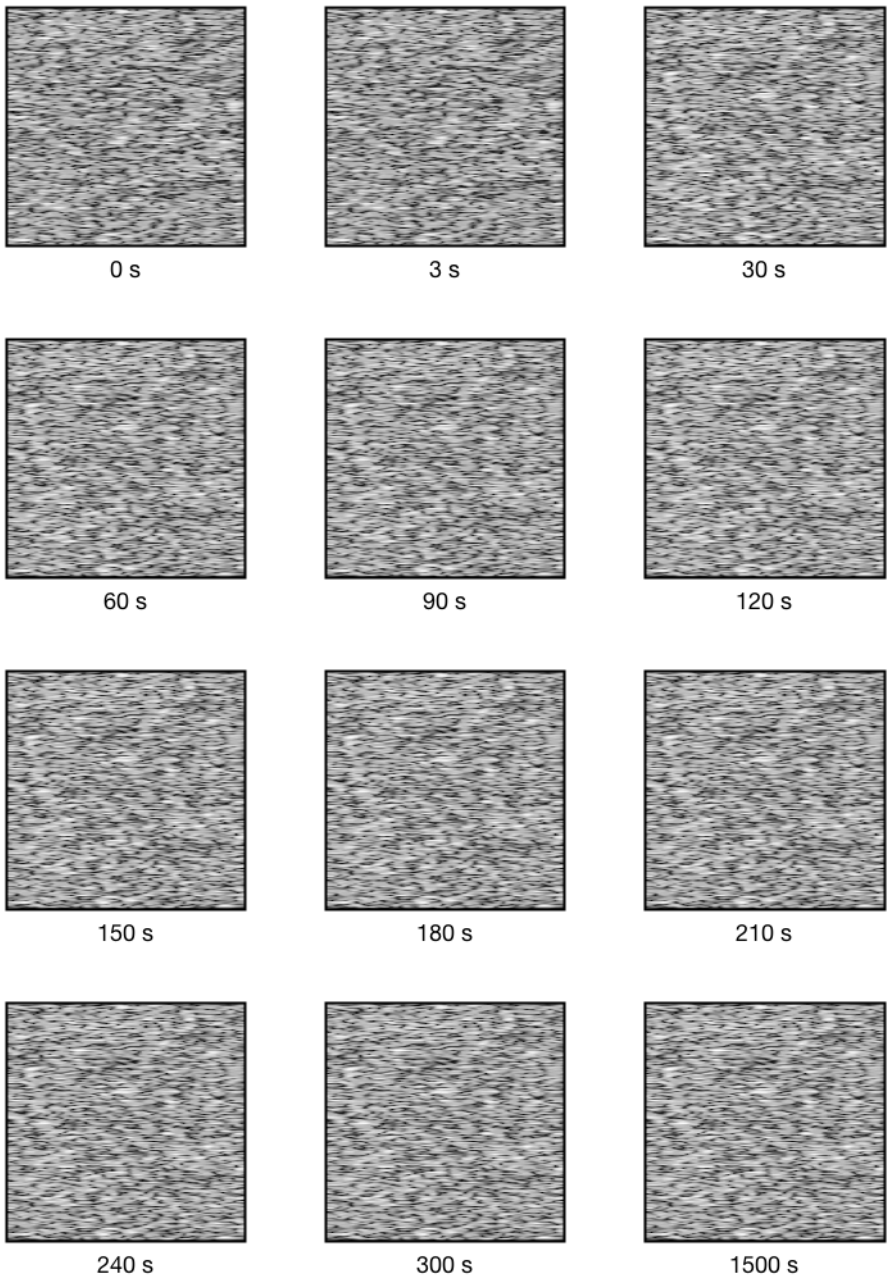

Figure 6.8: Example brightness mode images produced from the simulated RF data.

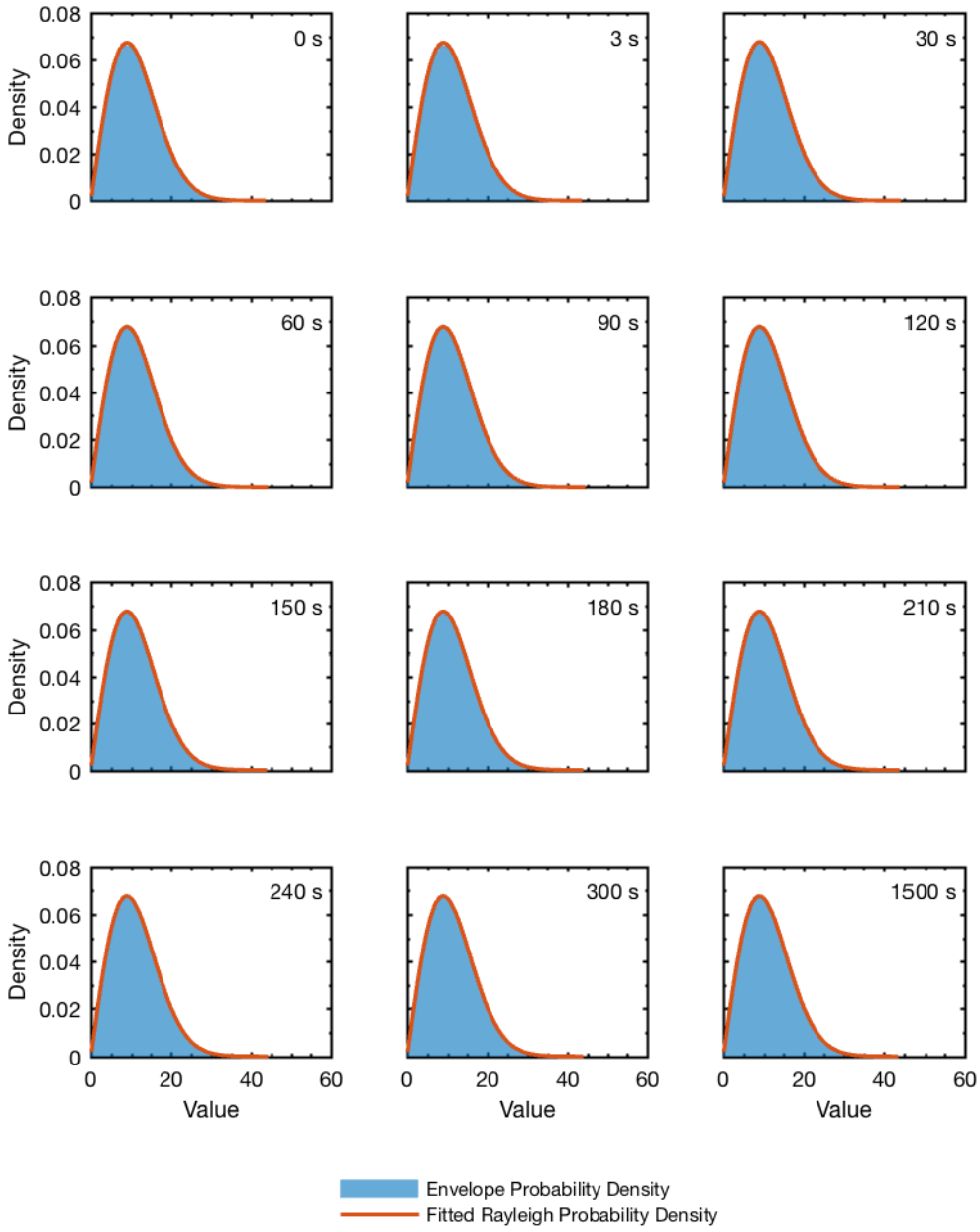

Figure 6.9: Example histograms of the signal envelope for the simulated RF frames. The envelope levels are Rayleigh distributed, suggesting that the simulated ultrasound frames contain fully developed speckle.

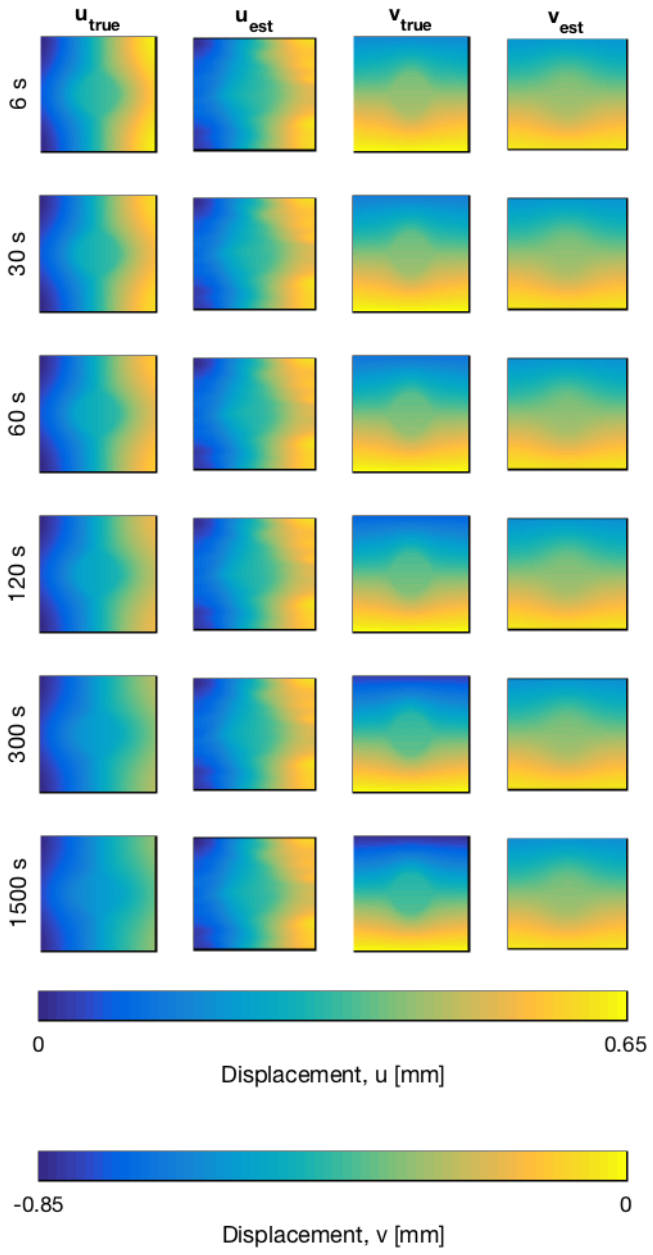

Figure 6.10: Example displacement estimates from speckle tracking applied to the synthesized RF frame sequence showing good agreement between the true and measured displacements.

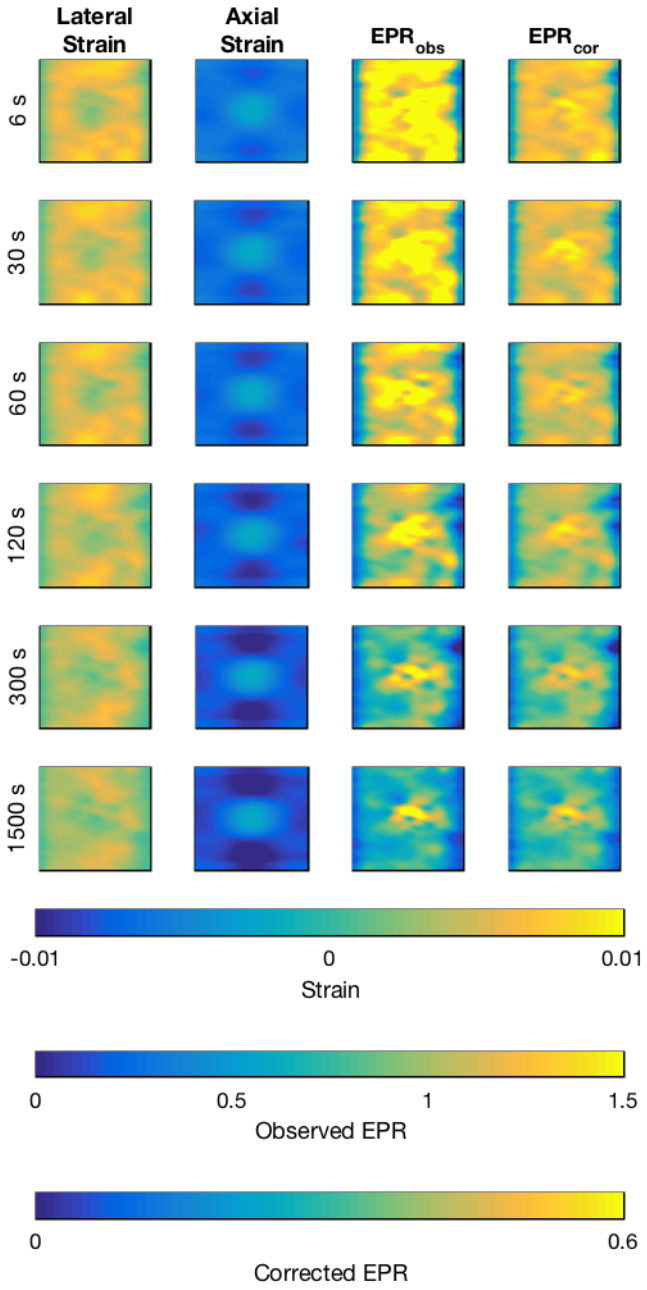

Figure 6.11: Example strain and EPR estimates from speckle tracking and strain estimators applied to the synthesized RF frame sequence.

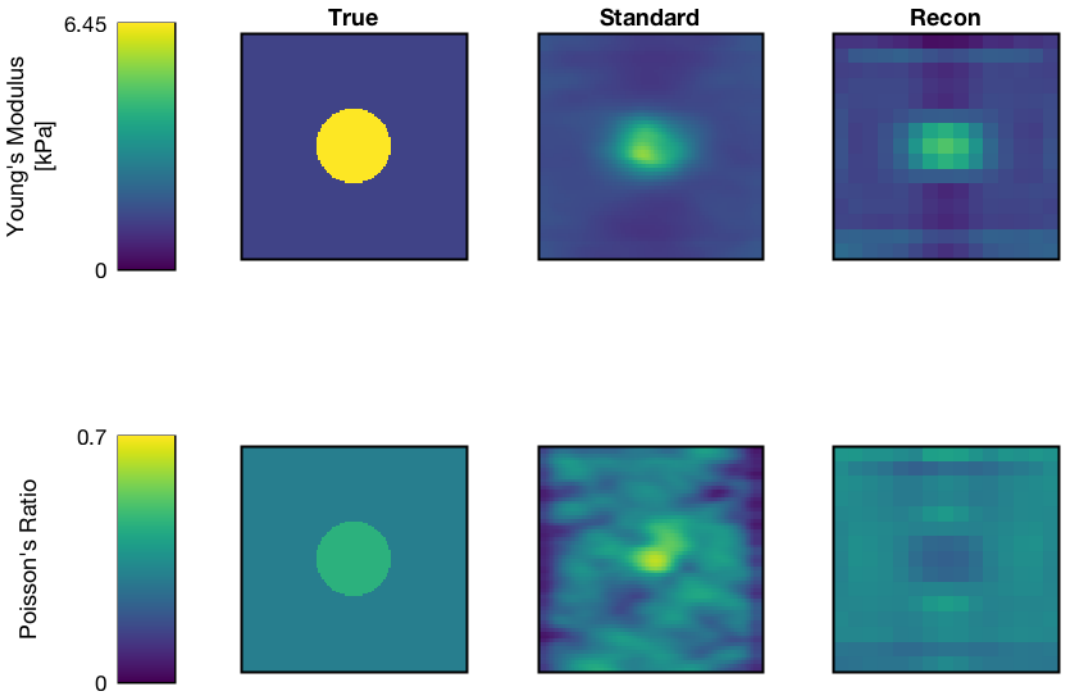

Figure 6.12: Comparison of Young's modulus and Poisson's ratio images estimated by the proposed reconstruction method (Recon) and by standard elastography and poroelastography techniques for a simulated phantom with an inclusion that is less compressible than the background (Background: $\nu = 0.3$, Inclusion: $\nu = 0.45$).

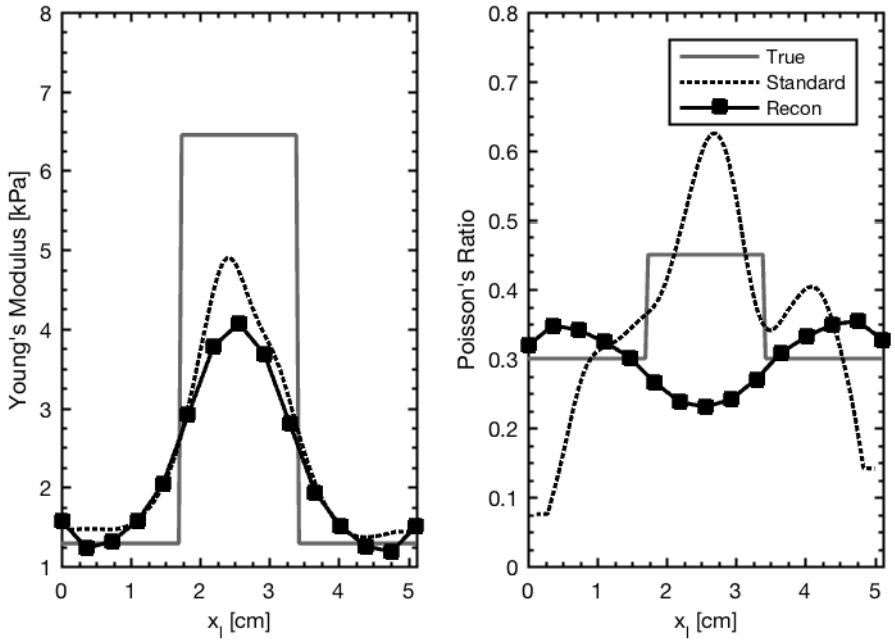

Figure 6.13: Comparison of Young's modulus and Poisson's ratio estimates along the line $y = 2.5$ cm for a simulated phantom with an inclusion that is less compressible than the background (Background: $\nu = 0.3$, Inclusion: $\nu = 0.45$).

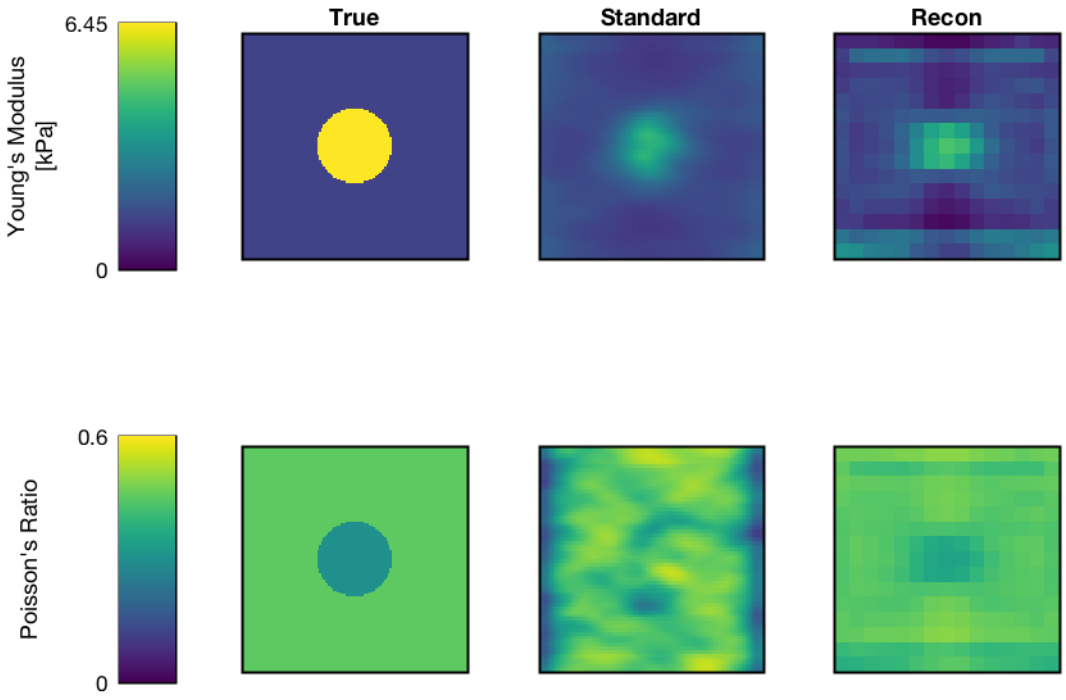

Figure 6.14: Comparison of Young's modulus and Poisson's ratio images estimated by the proposed reconstruction method (Recon) and by standard elastography and poroelastography techniques for a simulated phantom with an inclusion that is less compressible than the background (Background: $\nu = 0.3$, Inclusion: $\nu = 0.45$).

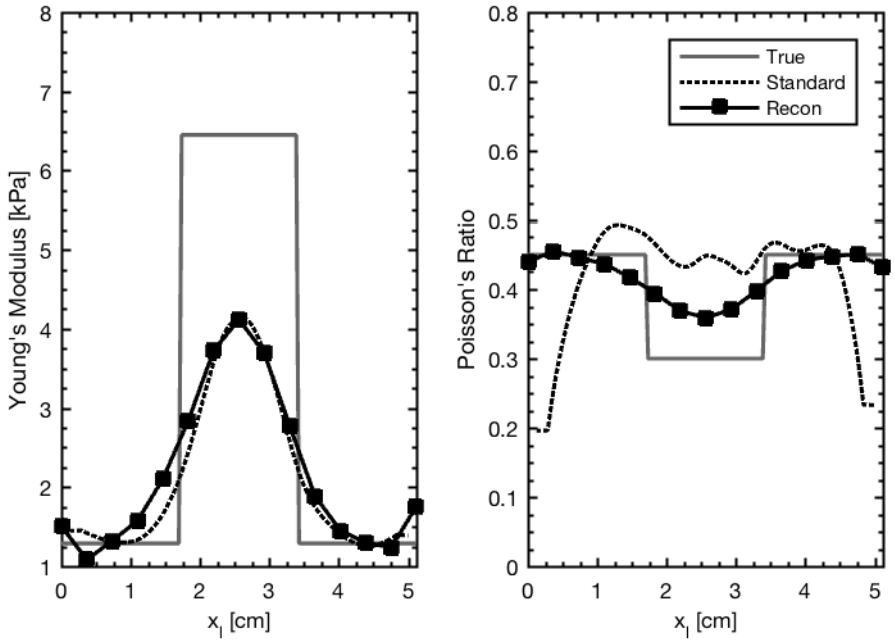

Figure 6.15: Comparison of Young's modulus and Poisson's ratio estimates along the line $y = 2.5$ cm for a simulated phantom with an inclusion that is less compressible than the background (Background: $\nu = 0.3$, Inclusion: $\nu = 0.45$).

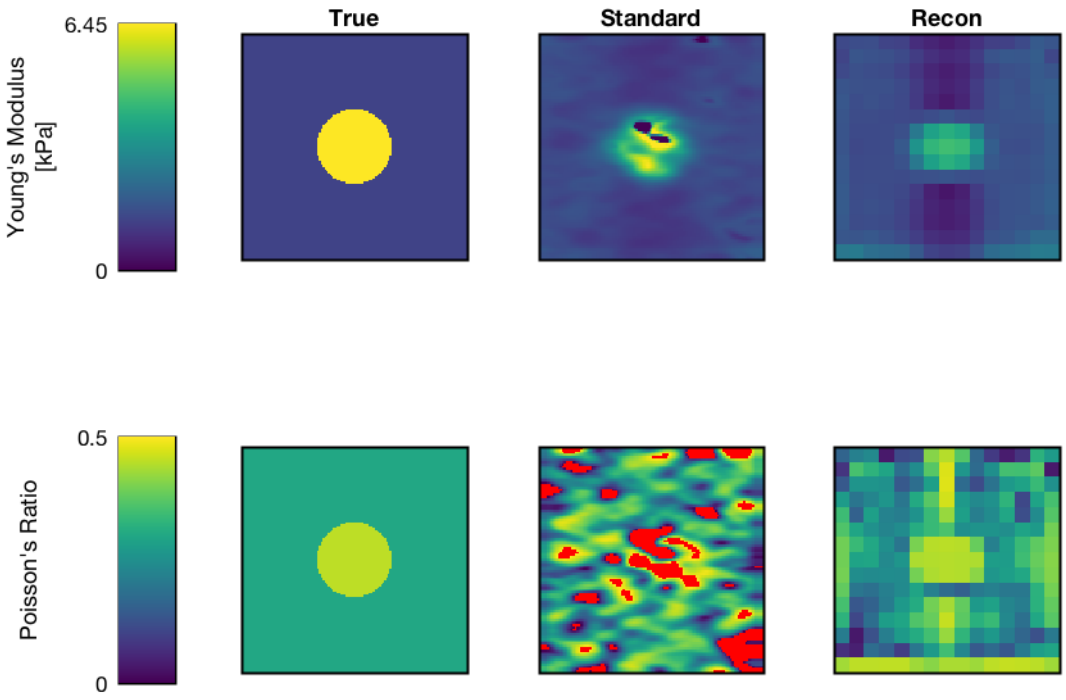

Figure 6.16: Comparison of Young's modulus and Poisson's ratio images estimated by the proposed reconstruction method (Recon) and by standard elastography and poroelastography techniques for a simulated phantom with an inclusion that is less compressible than the background (Background: $\nu = 0.3$, Inclusion: $\nu = 0.45$). This reconstruction used the modified regularization function described in section 6.2.6 with a 15×15 pixel grid.

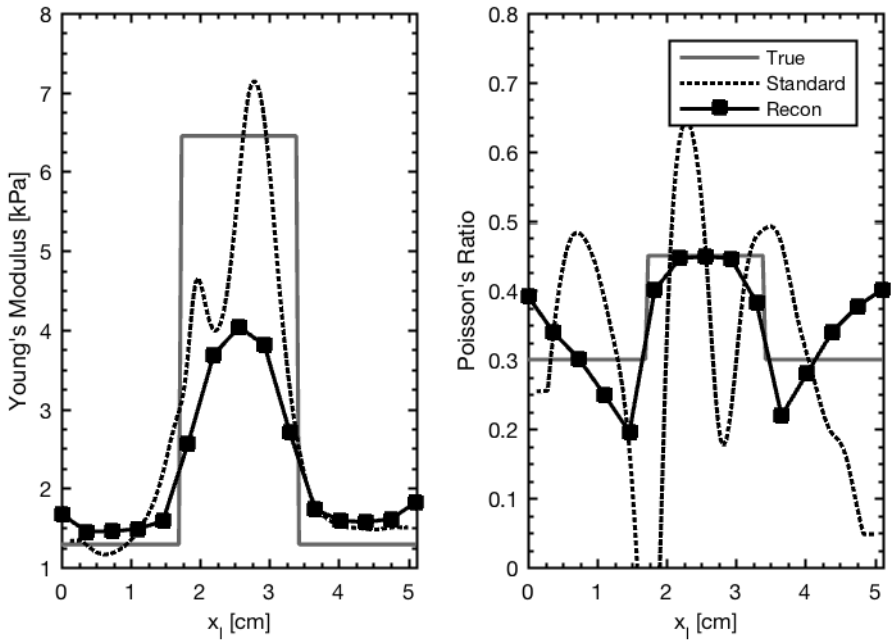

Figure 6.17: Comparison of Young's modulus and Poisson's ratio estimates along the line $y = 2.5$ cm for a simulated phantom with an inclusion that is less compressible than the background (Background: $\nu = 0.3$, Inclusion: $\nu = 0.45$). This reconstruction used the modified regularization function described in section 6.2.6 with a 15×15 pixel grid.

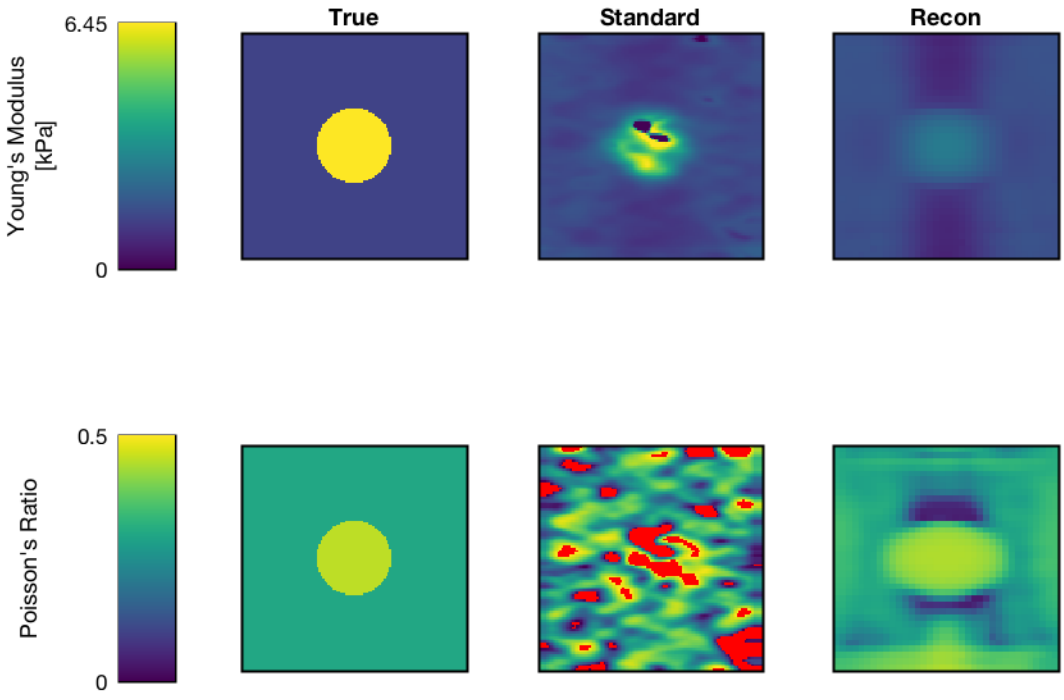

Figure 6.18: Comparison of Young's modulus and Poisson's ratio images estimated by the proposed reconstruction method (Recon) and by standard elastography and poroelastography techniques for a simulated phantom with an inclusion that is less compressible than the background (Background: $\nu = 0.3$, Inclusion: $\nu = 0.45$). This reconstruction used the modified regularization function described in section 6.2.6 with a 36×36 pixel grid.

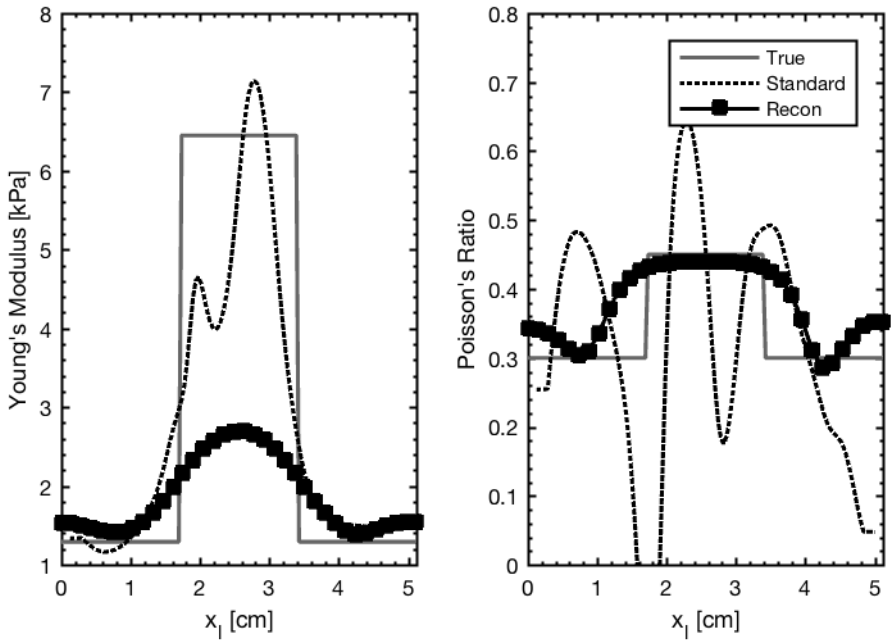

Figure 6.19: Comparison of Young's modulus and Poisson's ratio estimates along the line $y = 2.5$ cm for a simulated phantom with an inclusion that is less compressible than the background (Background: $\nu = 0.3$, Inclusion: $\nu = 0.45$). This reconstruction used the modified regularization function described in section 6.2.6 with a 36×36 pixel grid.

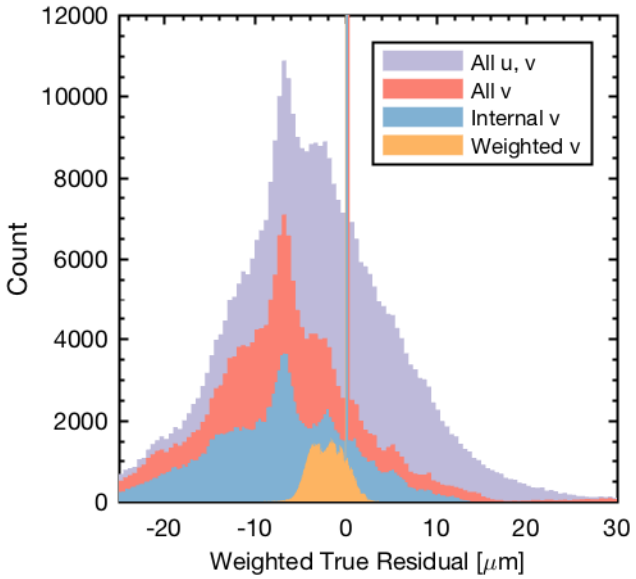

Figure 6.20: Histograms of the weighted displacement error $W(d - f(x_{true}))$ for the measurements obtained from a simulated phantom with an inclusion that is less compressible than the background (Background: $\nu = 0.3$, Inclusion: $\nu = 0.45$). Including all measurements components with indentical weights (All u, v) produces a broader and more biased histogram. As we remove the lateral displacement estimates (All v) as well as any points extrapolated from the measured data (Internal v) the total error decreases, but the bias remains. Weighting the measurements by the CRLB greatly reduces the error and bias, but does not negate it (Weighted v).

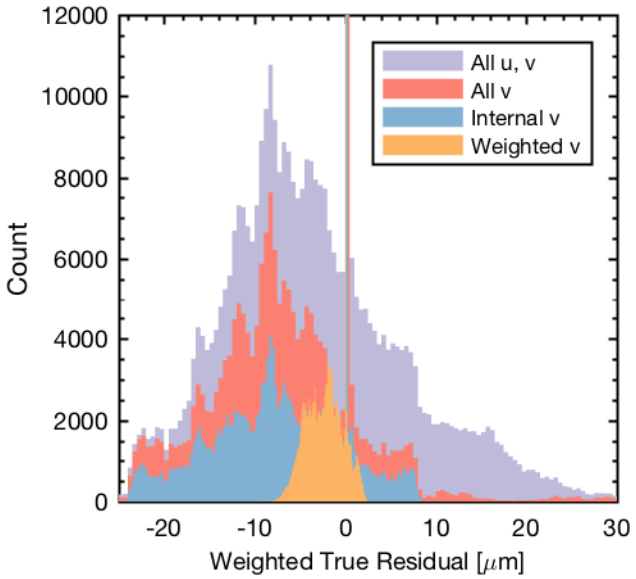

Figure 6.21: Histograms of the weighted displacement error $W(d - f(x_{true}))$ for the measurements obtained from a simulated phantom with an inclusion that is more compressible than the background (Background: $\nu = 0.45$, Inclusion: $\nu = 0.3$). Including all measurements components with indentical weights (All u, v) produces a broader and more biased histogram. As we remove the lateral displacement estimates (All v) as well as any points extrapolated from the measured data (Internal v) the total error decreases, but the bias remains. Weighting the measurements by the CRLB greatly reduces the error and bias, but does not negate it (Weighted v).

BIBLIOGRAPHY

Armstrong, C. G., Lai, W. M., and Mow, V. C. (1984). An analysis of the unconfined compression of articular cartilage. *J. Biomech. Eng.*, 106(2):165–73.

Arneson, T. J., Liu, J., Qiu, Y., Gilbertson, D. T., Foley, R. N., and Collins, A. J. (2010). Hospital treatment for fluid overload in the Medicare hemodialysis population. *Clin. J. Am. Soc. Nephrol.*, 5(6):1054–63.

Barbone, P. E. and Bamber, J. C. (2002). Quantitative elasticity imaging: what can and cannot be inferred from strain images. *Phys. Med. Biol.*, 47(12):2147–64.

Berry, G. P., Bamber, J. C., Armstrong, C. G., Miller, N. R., and Barbone, P. E. (2006a). Towards an acoustic model-based poroelastic imaging method: I. Theoretical foundation. *Ultrasound Med. Biol.*, 32(4):547–67.

Berry, G. P., Bamber, J. C., Miller, N. R., Barbone, P. E., Bush, N. L., and Armstrong, C. G. (2006b). Towards an acoustic model-based poroelastic imaging method: II. experimental investigation. *Ultrasound Med. Biol.*, 32(12):1869–85.

Berry, G. P., Bamber, J. C., Mortimer, P. S., Bush, N. L., Miller, N. R., and Barbone, P. E. (2008). The spatio-temporal strain response of oedematous and nonoedematous tissue to sustained compression in vivo. *Ultrasound Med. Biol.*, 34(4):617–29.

Biot, M. A. (1941). General theory of three-dimensional consolidation. *J. Appl. Phys.*, 12(2):155–164.

Cespedes, I., Insana, M. F., and Ophir, J. (1995). Theoretical bounds on strain estimation in elastography. *IEEE Trans. Ultrason. Ferroelectr. Freq. Control*, 42(5):969–971.

D'Errico, J. (2012). inpaint_nans. `https://www.mathworks.com/matlabcentral/fileexchange/4551-inpaint-nans`.

Detournay, E. and Cheng, A.-D. (1993). Fundamentals of poroelasticity. In Hudson, J. A., Brown, E. T., Fairhurst, C., and Hoek, E., editors, *Compr. Rock Eng. Princ. Pract. Proj.*, chapter 5, pages 113–171. Pergamon Press, Oxford, 1 edition.

Doyley, M. M., Meaney, P. M., and Bamber, J. C. (2000). Evaluation of an iterative reconstruction method for quantitative elastography. *Phys. Med. Biol.*,

45(6):1521–1540.

Doyley, M. M., Srinivasan, S., Pendergrass, S. a., Wu, Z., and Ophir, J. (2005). Comparative evaluation of strain-based and model-based modulus elastography. *Ultrasound Med. Biol.*, 31(6):787–802.

Fung, Y. (1993). *Biomechanics: Mechanical Properties of Living Tissues*. Springer New York, New York, NY, 2nd edition.

Garcia, D. (2010). Robust smoothing of gridded data in one and higher dimensions with missing values. *Comput. Stat. Data Anal.*, 54(4):1167–1178.

Garcia, D. (2011). A fast all-in-one method for automated post-processing of PIV data. *Exp. Fluids*, 50(5):1247–1259.

Garra, B. S., Cespedes, I., Ophir, J., Spratt, S. R., Zuurbier, R. A., Magnant, C. M., and Pennanen, M. F. (1997). Elastography of breast lesions: initial clinical results. *Radiology*, 202(1):79–86.

Goenezen, S., Barbone, P., and Oberai, A. A. (2011). Solution of the nonlinear elasticity imaging inverse problem: The incompressible case. *Comput. Methods Appl. Mech. Eng.*, 200(13-16):1406–1420.

Insana, M. F., Pellot-Barakat, C., Sridhar, M., and Lindfors, K. K. (2004). Viscoelastic imaging of breast tumor microenvironment with ultrasound. *J. Mammary Gland Biol. Neoplasia*, 9(4):393–404.

Kallel and Ophir (1997). A Least-Squares Strain Estimator for Elastography. *Ultrason. Imaging*, 19(3):195–208.

Kallel, F., Bertrand, M., and Ophir, J. (1996). Fundamental limitations on the contrast-transfer efficiency in elastography: an analytical study. *Ultrasound Med. Biol.*, 22(4):463–470.

Konofagou, E. and Ophir, J. (1998). A new elastographic method for estimation and imaging of lateral displacements, lateral strains, corrected axial strains, and Poisson's ratios in tissues. *Ultrasound Med. Biol.*, 24(8):1183–1199.

Konofagou, E. E., Harrigan, T. P., Ophir, J., and Krouskop, T. A. (2001). Poroelasticity: Imaging the poroelastic properties of tissues. *Ultrasound Med. Biol.*, 27(10):1387–1397.

Kouw, P. M., Kooman, J. P., Cheriex, E. C., Olthof, C. G., de Vries, P. M., and Leunissen, K. M. (1993). Assessment of postdialysis dry weight: a comparison of techniques. *J. Am. Soc. Nephrol.*, 4(1):98–104.

Kuei, S., Lai, W., and Mow, V. (1978). A biphasic rheological model of articular cartilage. In Eberhardt, R. and Burstein, A., editors, *Adv. Bioeng.*, page 17. American Society of Mechanical Engineers.

Lindberg, M., Prütz, K.-G., Lindberg, P., and Wikström, B. (2009). Interdialytic weight gain and ultrafiltration rate in hemodialysis: lessons about fluid adherence from a national registry of clinical practice. *Hemodial. Int.*, 13(2):181–8.

Mow, V. and Kuei, S. (1980). Biphasic creep and stress relaxation of articular cartilage in compression: theory and experiments. *J. . . .*, 102(February 1980):73–84.

Mow, V. and Lai, W. (1980). Recent developments in synovial joint biomechanics. *Siam Rev.*, 22(3).

Mridha, M. and Odman, S. (1986). Noninvasive method for the assessment of subcutaneous oedema. *Med. Biol. Eng. Comput.*, 24(4):393–8.

Nair, S. P. and Righetti, R. (2015). Resimulation of noise: a precision estimator for least square error curve-fitting tested for axial strain time constant imaging. *Phys. Med. Biol.*, 60(9):3515–3529.

Nair, S. P., Yang, X., Krouskop, T. a., and Righetti, R. (2011). Performance analysis of a new real-time elastographic time constant estimator. *IEEE Trans. Med. Imaging*, 30(2):497–511.

Oberai, A. A., Gokhale, N. H., Doyley, M. M., and Bamber, J. C. (2004). Evaluation of the adjoint equation based algorithm for elasticity imaging. *Phys. Med. Biol.*, 49(13):2955–2974.

Oberai, A. A., Gokhale, N. H., and Feijoo, G. R. (2003). Solution of inverse problems in elasticity imaging using the adjoint method. *Inverse Probl.*, 19(2):297–313.

Oe, B., de Fijter, C. W., Geers, T. B., Vos, P. F., Donker, A. J., and de Vries, P. M. (2000). Diameter of inferior caval vein and impedance analysis for assessment of hydration status in peritoneal dialysis. *Artif. Organs*, 24(7):575–7.

Ophir, J., Cespedes, I., Ponnekanti, H., Yazdi, Y., and Li, X. (1991). Elastography: A quantitative method for imaging the elasticity of biological tissues. *Ultrason. Imaging*, 134:111–134.

Perriñez, P. R., Kennedy, F. E., Van Houten, E. E. W., Weaver, J. B., and Paulsen, K. D. (2009). Modeling of soft poroelastic tissue in time-harmonic MR elastography. *IEEE Trans. Biomed. Eng.*, 56(3):598–608.

Perriñez, P. R., Kennedy, F. E., Van Houten, E. E. W., Weaver, J. B., and Paulsen, K. D. (2010a). Magnetic resonance poroelastography: an algorithm for estimating the mechanical properties of fluid-saturated soft tissues. *IEEE Trans. Med. Imaging*, 29(3):746–55.

Perriñez, P. R., Pattison, A. J., Kennedy, F. E., Weaver, J. B., and Paulsen, K. D. (2010b). Contrast detection in fluid-saturated media with magnetic resonance poroelastography. *Med. Phys.*, 37(7):3518–3526.

Pitre, Jr, J. J., Koziol, L., Kruger, G. H., Vollmer, A., Ophir, J., Ammann, J., Weitzel, W. F., and Bull, J. L. (2016). Design and testing of a single-element ultrasound viscoelastography system for point-of-care edema quantification. *Ultrasound Med. Biol.*, 42(9):2209–2219.

Qiu, Y., Sridhar, M., Tsou, J. K., Lindfors, K. K., and Insana, M. F. (2008). Ultrasonic viscoelasticity imaging of nonpalpable breast tumors: preliminary results. *Acad. Radiol.*, 15(12):1526–33.

Righetti, R., Garra, B. S., Mobbs, L. M., Kraemer-Chant, C. M., Ophir, J., and Krouskop, T. A. (2007a). The feasibility of using poroelastographic techniques for distinguishing between normal and lymphedematous tissues in vivo. *Phys. Med. Biol.*, 52(21):6525–41.

Righetti, R., Ophir, J., and Krouskop, T. A. (2005). A method for generating permeability elastograms and Poisson's ratio time-constant elastograms. *Ultrasound Med. Biol.*, 31(6):803–16.

Righetti, R., Ophir, J., Srinivasan, S., and Krouskop, T. A. (2004). The feasibility of using elastography for imaging the Poisson's ratio in porous media. *Ultrasound Med. Biol.*, 30(2):215–28.

Righetti, R., Righetti, M., Ophir, J., and Krouskop, T. A. (2007b). The feasibility of estimating and imaging the mechanical behavior of poroelastic materials using axial strain elastography. *Phys. Med. Biol.*, 52(11):3241–59.

Samani, A. and Plewes, D. (2004). A method to measure the hyperelastic parameters of ex vivo breast tissue samples. *Phys. Med. Biol.*, 49(18):4395–4405.

Simon, B. R. (1992). Multiphase poroelastic finite element models for soft tissue structures. *Appl. Mech. Rev.*, 45(6):191–218.

Skovoroda, A. R., Emelianov, S. Y., Lubinski, M. A., Sarvazyan, A., and O'Donnell, M. (1994). Theoretical analysis and verification of ultrasound displacement and strain imaging. *IEEE Trans. Ultrason. Ferroelectr. Freq. Control*, 41(3):302–313.

Skovoroda, A. R., Emelianov, S. Y., and O'Donnell, M. (1995). Tissue elasticity reconstruction based on ultrasonic displacement and strain images. *IEEE Trans. Ultrason. Ferroelectr. Freq. Control*, 42(4):747–765.

Sridhar, M., Liu, J., and Insana, M. F. (2007). Viscoelasticity imaging using ultrasound: parameters and error analysis. *Phys. Med. Biol.*, 52(9):2425–43.

Walker, H. K. (1990). The Origins of the History and Physical Examination. In Walker, H. K., Hall, W. D., and Hurst, J. W., editors, *Clin. Methods Hist. Phys. Lab. Exam.*, chapter 1, pages 5–21. Butterworths, Boston, 3rd edition.

Walker, W. F. and Trahey, G. E. (1994). A fundamental limit on the accuracy of

speckle signal alignment. *IEEE Ultrason. Symp.*, pages 1787–1792.

Westerweel, J. and Scarano, F. (2005). Universal outlier detection for PIV data. *Exp. Fluids*, 39:1096–1100.

Yashiro, M., Kamata, T., Yamadori, N., Tomita, M., and Muso, E. (2007). Evaluation of markers to estimate volume status in hemodialysis patients: atrial natriuretic peptide, inferior vena cava diameter, blood volume changes and filtration coefficients of microvasculature. *Ther. Apher. Dial.*, 11(2):131–7.

Zhang, Y., Oberai, A. A., Barbone, P. E., and Harari, I. (2012). Solution of the time-harmonic viscoelastic inverse problem with interior data in two dimensions. *Int. J. Numer. Methods Eng.*, 92(13):1100–1116.

Zienkiewicz, O. C. and Taylor, R. L. (2000). *The Finite Element Method*. Butterworth-Heinemann, Oxford, 5 edition.

CHAPTER 7

Conclusions and future directions

7.1 Conclusions

The work presented in chapters 4-6 contributed to the development of new methods of estimating viscoelastic and poroelastic tissue properties as well as the understanding of present methods. The literature on poroelastgraphy is sparse, and the field is young compared to the rest of ultrasound elastography. Furthermore, it has met only limited success in clinical studies, in part because the results can be difficult to interpret. This work has sought to expand the theoretical understanding of poroelastic imaging and highlight important considerations for interpreting poroelastogram measurements. The importance of geometry and loading assumptions has been demonstrated using both numerical and experimental methods. Finally, new methods of poroelastic parameter estimation have been proposed and evaluated, the goal being to provide more flexibility in the assumptions that must be accepted for any poroelastgraphy measurement.

In Chapter 4, I tested a simplified single-element ultrasound viscoelastography (UVE) system for point-of-care edema monitoring by measuring the viscoelastic properties of a tissue-mimicking material (tofu) in creep tests under large strains, as would be used clinically to diagnose edema. I demonstrated that the UVE system was capable of generating depth-dependent maps of viscoelastic material pa-

rameters including time constants and elastic moduli. My results suggest successful benchtop validation of this UVE system. This provides a good foundation for future studies to investigate the relationship between UVE measurements and current methods of assessing peripheral edema.

In Chapter 5, I detailed the development of two finite element models of poroelastic deformation – a cylinder and a rectangular block – and used these to demonstrate the importance of geometric and strain magnitude assumptions on poroelastic parameter estimation methods that utilize curve fitting. In particular, I showed that Armstrong's solution to the KLM equations may not be accurate in poroelastography measurements utilizing large strains. Furthermore, I showed that assumptions of cylindrical geometry behave very differently from an alternative loading that clinical use may find more suitable. These differences exist not only in the axial strain history, but also in the behavior of the effective Poisson's ratio, a key component of poroelastography imaging. The predictions of the computational models were verified using experimental measurements of tofu cylinders and blocks under large strain. The results demonstrate the importance of utilizing accurate assumptions in poroelastic parameter estimation and suggest that more general methods may be more useful for obtaining accurate measurements in the clinic.

In Chapter 6, I described the development and testing of a new ultrasound poroelastography method based on Biot poroelasticity and an inverse problem formulation. Compared to previous poroelastic imaging methods, this approach reduces the number of assumptions imposed and allows for quantitative estimation of spatially varying poroelastic properties. I tested this method in a simulation study using both ideal data corrupted by zero mean Gaussian noise and using displacement measurements from simulated ultrasound images. For the case of ideal measurements and Gaussian noise, my method greatly outperformed traditional

poroelastography methods. In the simulated ultrasound experiments, biases in the data posed a major challenge for the poroelastic reconstruction algorithm, and the quality of the parameter estimates greatly decreased. This sensitivity to measurement errors and the computational expense are both major challenges to my proposed method. Despite this, the method still is of theoretical value for the field of poroelastography and the study of inverse problems.

7.2 Summary of Scientific Contributions

The key contributions of this work to the development of ultrasound viscoelastography and ultrasound poroelastography are listed as follows:

1. Ultrasound viscoelastography can be used to generate depth dependent maps of viscoelastic material properties in a tissue mimicking material.

2. Poroelastography techniques that rely on curve fitting to estimate poroelastic parameters must carefully match the assumptions of the fitting model and the experimental measurements. Mismatches between these assumptions and conditions can lead to disagreement between the true poroelastic parameters and the measured estimates.

3. When creep loading is applied to a small central area embedded in a larger block of tissue, as might be done in a clinical poroelastography experiment, the effective Poisson's ratio exhibits depth dependence and does not decay uniformly to the Poisson's ratio of the drained matrix.

4. Fitting mismatches of poroelastic parameters are greater at larger strain, but appropriate choices of fitting model can decrease these errors.

5. Poroelastic imaging can be posed as an inverse problem, and spatial maps of poroelastic properties can be estimated without violating the assumption of

spatial uniformity required by most poroelastic parameter estimation methods.

7.3 Future Directions

This work has provided a number of avenues for estimating edematous tissue mechanical properties using ultrasound displacement and strain measurements. The results presented in this dissertation can be further expanded upon by benchtop and clinical measurements.

It was noted in Chapter 5 that the creep curves predicted for the "block" geometry tend to converge as the area ratio $\hat{A} = A/A_{load}$ increases. This geometry may offer advantages in providing robust parameter estimates and in ease of clinical implementation. Of theoretical interest, future studies should attempt to obtain an analytical solution to the "slab" geometry $\hat{A} \to \infty$. This would facilitate efficient and accurate parameter estimation in a geometry that is easily replicated in clinical measurements.

Most poroelastography studies rely on the assumption that, at steady state, the EPR decays to Poisson's ratio of the drained porous matrix. The finite element models in Chapter 5 predicted the depth dependent evolution of the effective Poisson's ratio (EPR). This has important implications for interpreting EPR elastograms, and benchtop validation of these numerical predictions is vital to understanding the images obtained in the clinic. Future studies should therefore be conducted to examine this effect in poroelastic phantoms.

Chief among the open questions that remain are questions of clinical applicability. More clinical studies of poroelastography are needed to determine how useful this method might be in quantifying the properties of edematous tissue. This work has highlighted the role of model assumptions and raised new questions about the

most accurate way to perform and interpret clinical measurements. To further explore this, clinical studies should employ a wide variety of loading conditions, geometric configurations, applied strain magnitudes, and deformation models. Of immediate interest is the use of the "slab" geometry in clinical measurements since this configuration can be easily realized clinically. Furthermore, since the "block" finite element models tend to converge as $\hat{A} \rightarrow \infty$, this configuration may provide robust measurements of poroelastic parameters that are not not as sensitive to geometric assumptions. Additionally, clinical studies should explore new geometries and loading configurations. The prospect of using radial compression of the lower limb is particularly attractive since it could easily be applied with a blood pressure cuff.

The inverse problem formulation of the poroelastic imaging problem described in Chapter 6 also provides a completely new avenue of investigation. In its present form, the method is computationally inefficient, but shows theoretical promise. Further work should be done to improve efficiency and optimize the performance of the algorithm. Future studies may use this increased efficiency to more extensively explore the effects of temporal sampling, grid resolution, and strain magnitude, and to increase the robustness of this method to measurement errors, either through improved data weighting or the use of different objective functions or regularizers.

Efforts to improve computational efficiency and understand parameter selection may also facilitate future clinical studies. In particular, the permeability of the tissue may be extremely useful clinically as it may indicate the degree to which fluid is *mobile* in edematous tissues. The inclusion of permeability into the inverse problem formulation is straightforward but computationally expensive. If adequate gains in efficiency can be achieved, however, this may provide an easily interpreted variable for quantitatively evaluating edema in clinical studies.